POLITECNICO DI MILANO

Scuola di Ingegneria Industriale e dell'Informazione

Corso di Laurea in Ingegneria Meccanica

Multi-dimensional CFD Simulation of a H-type Darrieus Vertical-Axis Wind Turbine with OpenFOAM®

Relatore: Prof. FEDERICO PISCAGLIA
Correlatore: Ing. ANDREA MONTORFANO

Tesi di laurea di:

GIULIA BALDASSARRA
Matricola 804806

Anno Accademico 2014 - 2015

Abstract

A H-type Darrieus VAWT has been investigated with OpenFOAM®. The CFD simulation has been the test-case for the application to an external-aerodynamics case of the lengthscale-based hybrid model DLRM (*Dynamic Length-scale Resolution Model*), which operates in URANS or ILES mode depending on the comparison of the modeled scales to what can potentially be resolved by the computational grid and time-step. For the simulation, the dynamic OpenFOAM®solver pimpleDyMFoam for incompressible flows has been chosen, and the mesh has been realized with Pointwise®.
The rotor is composed by three untwisted blades, with dihedral NACA 0021 profiles, connected to the vertical mast by means of two horizontal supports. The wind velocity has been set to 14.2 m/s and the turbine rotates at 41.44 rad/s, which corresponds to a tip-speed ratio of $\lambda = 1.5$. This choice stems from the experimental inference that the turbine is very likely to stall for $\lambda \leq 2$. Thus, it definitely represents a crucial condition for understanding the turbine behavior.
In order to reproduce a non-confined environment (i.e. to avoid any blockage effect from the boundaries), a very extended domain has been considered, which results in a ≈ 45 M-cell mesh. Moreover, the domain has been split into an internal cylinder, integral with the turbine motion and very refined, and an outer domain, still and coarser. The interpolations of the results at the cylinder lateral surface have been then handled with an *Arbitrary Mesh Interface*.
The final purpose of this work has been the comparison of the numerical results to already available experimental data from tests performed in the wind tunnel at Politecnico di Milano. Much attention has been paid to the analysis of the wake, in terms of fluid deceleration and deflection, in both the transversal and the longitudinal direction with respect to the flow stream. The main aerodynamic coefficients (lift, drag, power and torque) have been computed as well. As a result, a good agreement between the numerical solutions and the data from tests has been observed.

Keywords: vertical-axis wind turbine, OpenFOAM, computational fluid-dynamics, RANS/LES hybrid models, DLRM, moving mesh, Arbitrary Mesh Interface.

Sommario

Oggetto del lavoro di tesi è l'analisi CFD di una turbina eolica ad asse verticale Darrieus di tipo H mediante il codice di calcolo OpenFOAM®. La simulazione rappresenta il test-case per l'applicazione a casi di aerodinamica esterna del modello ibrido RANS/ILES DLRM (per esteso *Dynamic Length-scale Resolution Model*), che opera in modalità URANS o ILES sulla base di un confronto dinamico tra le scale modellate e quelle potenzialmente risolvibili. Per la simulazione è stato adottato il solutore dinamico incomprimibile pimpleDyMFoam, disponibile nella distribuzione ufficiale di OpenFOAM®, mentre la griglia di calcolo è stata realizzata mediante il generatore di griglie Pointwise®.
Il rotore è composto da tre pale diedre dal profilo simmetrico NACA0021, a sezione uniforme, fissate all'asse centrale per mezzo di due piatti orizzontali. Il vento ha una velocità di 14.2 m/s e la turbina ruota a 41.44 rad/s, così da ottenere un rapporto di velocità periferica $\lambda = 1.5$. Questa scelta deriva dalle evidenze sperimentali sull'alta probabilità che la turbina vada in stallo per $\lambda \leq 2$, condizione decisamente interessante per studiare il funzionamento della turbina.
Per riprodurre un flusso d'aria non confinato (ovvero evitare effetti di bloccaggio per via del contorno), si è preso in considerazione un dominio molto esteso, corrispondente a ≈ 45 M di celle. Il dominio è stato poi suddiviso in due regioni: un cilindro che racchiude la turbina, rotante solidalmente con essa e con mesh più raffinata, e un dominio esterno, fisso e a minor risoluzione. L'interfaccia è gestita mediante una *Arbitrary Mesh Interface*, che opera un'interpolazione dei flussi delle variabili conservate attraverso le superfici di regioni di mesh adiacenti.
Obiettivo del lavoro di tesi è stato il confronto dei risultati numerici con gli esiti già disponibili di test sperimentali condotti presso la galleria del vento del Politecnico di Milano. In particolare, è stato analizzato lo sviluppo della scia, trasversalmente e longitudinalmente rispetto al flusso indisturbato, sia in funzione del rallentamento che dell'angolo di imbardata assunto dopo l'impatto con la turbina. Sono state inoltre calcolate le forze agenti sulle pale del rotore, le coppie e le potenze prodotte e i coefficienti aerodinamici di drag e lift. Il risultato mostra una buona corrispondenza tra le misure sperimentali ed i risultati numerici.

Parole chiave: turbina eolica ad asse verticale, OpenFOAM, fluidodinamica computazionale, modelli ibridi RANS/LES, DLRM, mesh mobile, Arbitrary Mesh Interface.

Aknowledgements

I would like to express my very great appreciation to Professor Federico Piscaglia, for his overwhelming dedication to my work and constant encouragement throughout the whole project. I am also very grateful to Eng. Andrea Montorfano for his generous help to this thesis. Thank you for always finding time for me, for your meticulous scrutiny and your precious hints.

My deepest acknowledgment goes to Professor Angelo Onorati and to the whole ICE group, from the Energy Department at Politecnico di Milano. Thank you for having welcomed me so warmly in your team and for believing in me from the very first time. I also thank Dr. Shashikant Aithal, from the Computing Resource Center at Argonne National Laboratory (IL, USA), for supplying the computing resources with the high-performance cluster Blues and, therefore, for making this work possible.

I am very grateful to Professors Javier García García and Juan Luis Prieto Ortiz, from Escuela Superior de Ingenieros Industriales (Universidad Politécnica de Madrid), for their helpfulness and support during my 5-month stay in Spain. Moreover, I would like to thank Professor Mario Guagliano, for the time he devotes to students and the enthusiasm he puts in his work.

My greatest gratitude goes to my family, for always supporting me. Thanks to Lavinia and Mattia Filippo, my best friends and my best luck, to my mum Tiziana for teaching us to think great and look further into the future, and to my dad Vinicio, for counterbalancing her brazen enthusiasm for life with a bunch of priceless rationality. Thanks also to my grandparents, for always keeping me company with your prayers.

In random order, I would also thank all the people who supported me with their affection throughout these years at university:

Alberto, for constantly showing me the silver lining of life and for having been biding your time so long just to hug me again. Thanks for being my motivation. Mericonci, for always cheering me up with your smile. Maria Grazia, for your being so genuinely unconventional. My wonderful friends from my hometown, who never left me alone, no matter the distance. I owe you a lot. Keyvan, for your honesty and generosity. You really helped me a lot on this work. Edo, for being such a principled person and such a good friend. Giammi, for never hanging up on such a fleeing super-busy friend.

Andrea and Brinchi, my first "partners in crime" on this adventure. Giuditta, for always thinking so highly of me. Tulsi, for having shared one of the most exciting experiences of life with me. The Porta Romana 106 crew, for being my second Milanese home. Mirella and Mimmo, for growing fond of us so unconditionally. Filippo, Alessandro and all the Master's students close to graduation, for sharing thoughts, troubles and suggestions. You have been of great support during this experience.

Contents

List of Figures

Chapter 1

Introduction to Wind Technology

Nowadays renewable resources attract quite an undivided attention in the energetic scenario for many reasons. The strongest points in favor are surely the environmental ecological cause and the human healthcare, since these technologies often stand out for the lowest levels of harmful emissions. The shortage of fossil fuels also represents a remarkable point. However, this attitude towards the promotion of low pollutant technologies is then barely followed by a practical commitment. If we count the hydraulic power out, we can easily get a sense about the situation and realize that most of the effort has yet to be made.

The set of technical and non-technical concerns to promote these technologies significantly influences the feasibility of the new methods. For instance, the random variability in both time and space of sources like the sun or the wind represents a true obstacle, since it implies variability in energy production as well and inaccuracy in efficiency and costs estimation. Nevertheless, even when benefits do counterbalance the related issues, these technologies struggle to be promoted, since today's skepticism is often trivially due to our strong fuel-based tradition in energy production. Such a radical change does require efforts and uncomfortable compromises, but the first changes must occur in our mindset.

Specifically, this thesis deals with wind energy, which is the second most exploited renewable source worldwide today, after water energy. It represents a countertrend if compared to the other alternative sources of energy, since its usage keeps increasing exponentially. The growing interest from industries and enterprises is indeed the most important proof of its potential and commercial exploitability, and these reasons are also the ones that principally make it worth being further investigated.

Wind technology consists in the conversion of the kinetic energy from wind into electricity. Energy from wind has always been exploited since the earliest times and today's working principle is still not far from the one of ancient windmills. The wind turns the blades of a turbine, which spins a shaft, and this rotation can be used for diverse purposes. However, despite its simplicity, the idea of connecting the rotor to an alternator in order to produce electricity is quite recent. In 1981 there was no production from wind worldwide. Today, thanks to the increasing attention to environmental preservation issues and consequent financial backing from international governments, this technology keeps being enhanced. The world wind power installed capacity has been estimated at 369.6 GW for 2014, which is 60 times its value for 1996 [12]. On condition that this non-linear trend of growth will not change, it is a plausible prediction, according to [11], that wind power might supply 22 % of electricity in 2030 for the entire world. Indeed, even if wind technology exhibits several inborn flows (non-continuous operation, occupation of the site, changes to landscape, acoustic emissions, electromagnetic interferences, disorders in avifauna, high initial investment in fixed capital), its peculiarity of environmental sustainability and its satisfactory energetic outcome manage to counterweight all these weaknesses and determine its competitiveness in a fuel-based world energetic scenario.

The first wind turbine design traces the old windmills style, since revolution occurs around a horizontal rotor shaft, positioned on top of a tower together with the generator. This is still the most common design and has been optimized through times, leading to an upstream three-blade rotor as the most suitable solution for power generation. Eventually, the rash for new turbine designs led to a completely different set-up, that is, vertical axis wind turbines. Indeed, despite their inborn issues, they still stand out for two key advantages: the electrical generator can be placed at the bottom of the machine, leading to a much less costly solution, and its revolution around a vertical mast makes the overall machine less sensitive to wind incidence, i.e. there is no need to align its receptive area with the flow stream direction. This way, wind turbines become suitable for residential energy production as well, since in urban environments the wind direction is usually non predictable or even occasional. There are two main designs for VAWTs. The first one is a S-shaped turbine called Savonius, simple in structure and subjected to a very unstable flow field, which implies a very low efficiency. The second one, namely Darrieus, is characterized by a number of vertically oriented airfoil blades revolving around a shaft. Both are actually subjected to a very complex aerodynamics, with rapid fluctuations and strong tip vortices, but since the Darrieus turbine uses an airfoil design, its optimization gives more chances to reach a higher efficiency, which theoretically might border on the values of HAWTs' efficiency.

Specifically, this thesis focuses on a three-blade H-type Darrieus model and aims at describing the aerodynamic field that originates from it, by simulating the flux investing the turbine through the open-source CFD software OpenFOAM. The wake formation and extension as well as the yaw angle that originates from the flow impacting the blades are two of the main quantities that will be investigated. Torque and power generation will also be taken into account, and lift and drag coefficients will be derived. Final goal of this work is the comparison of the simulation outputs to the experimental results found in literature. In this way, an adequate validated numerical model will be provided for future studies on the machine optimization.

1.1 Implications of a Wind-Based Technology

Wind turbines are devices that convert the kinetic energy from wind into electricity. Nowadays, there are unnumbered designs for this technology, each fulfilling some important requirements, but at the same time unavoidably presenting some limitations. Most of their weaknesses are actually in-born flaws related to the wind, which hardly can be addressed. Thus, it is of utmost importance to investigate first the general implications of a wind-based technology.

Wind is a convective flux originated by air density variations due to non-uniform heating from the sun. Its evolution is unpredictable in space and time: small local events induce big fluctuations that spread randomly. This is the first issue, since the input data to design wind turbines will always be uncertain. Indeed, pure mathematical modeling lead to very complex and non-linear formulations, as a true reflection of reality, and a statistical approach becomes mandatory prior to design turbines. Clearly, this implies that the more wind actual behavior deviate from the averaged one assumed, the more the results of the analysis lose reliability. To this purpose, the choice of a proper location is extremely important, not only because it influences the machine performances straightforwardly, but also because it simplifies and legitimates the analysis itself, accounting for the difficult modeling work to be done and allowing optimization. Favorable sites are characterized by strong wind intensity with large duration, such as mountaintops, costal regions or offshore sites, while, on contrary, in urban environments the wind usually does not reach a sufficiently high speed and changes its direction too often.

Indeed, there is an admissible range of velocities for a correct functioning of wind turbines, that is typically 5 to 30 m/s for common applications. This thesis study case perfectly fits the restriction, since the wind speed is

assumed to be 14.2 m/s far upstream of the machine. Precisely, if the wind speed is below this range, the turbine is not efficient or does not work at all; if it exceeds the higher limit, the turbine may be damaged. A few solutions are actually possible to avoid it, such as varying the blades' inclination to reduce the resistant section (flag position) or using mechanical brakes to slow the machine down, but they are just solutions to stem the problem, which should be preferably avoided on the whole.

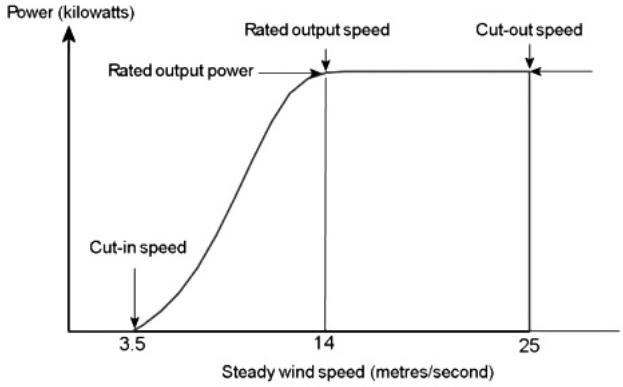

Figure 1.1: Typical HAWT Power Curve

Fig. 1.1 provides the typical HAWT power curve, showing how the power output varies with wind speed. The cut-in limit marks the beginning of energy production, which initially grows with a steep trend and eventually halts at the so-called rated power value. This energy output is then kept constant until the cut-out limit, which represents the last admissible functioning condition before breakage. Operation is theoretically possible in the whole band in-between the cut-in and the cut-out limits. However, efficiency results optimized (thus costs minimized) only if the wind speed exceeds the rated value.

Nevertheless, excessive speed is generally a rare condition if compared to insufficient speed. This is why, for instance, one of the first concerns when building a wind turbine is to mount it on top of a tower in order to expose it to sufficiently high wind intensity. Indeed, ground-level wind has generally no power due to the fact that its non-null velocity field ends up as just a chaotic motion, and at the same time the wind speed increases very slowly with altitude (the estimate is a power of 1/7) [6].

The very last point to consider is the small density of air. If velocity is somehow prescribed and density is very small, the only option to get a satisfactory mass flow rate is to increase the machine front area. A high mass

flow rate, indeed, is desirable because of its correlation to power. It stands to reason that the costs hugely increase, not only because the dimensions of the rotor increase, but also because the rotor needs to be supported by a higher and more resistant tower. Maintenance becomes an issue as well.

1.2 Classification of Wind Turbines

Wind turbines always stand apart from other turbomachinery for their singular features. However, it might be interesting to arbitrarily frame them up into the conventional classification of turbines in Pelton, Francis and Kaplan. The two main parameters that can be used for classification are the motor head and the volumetric flow rate, whose correlation is provided by Fig. 1.2. Experimental results collected in this graph show that if a turbine works with large fluid flows, it usually cannot deal with a high head as well. Pelton turbine results in being the most suitable for high head, while Kaplan is the most adequate to work with high volumetric flow rate.

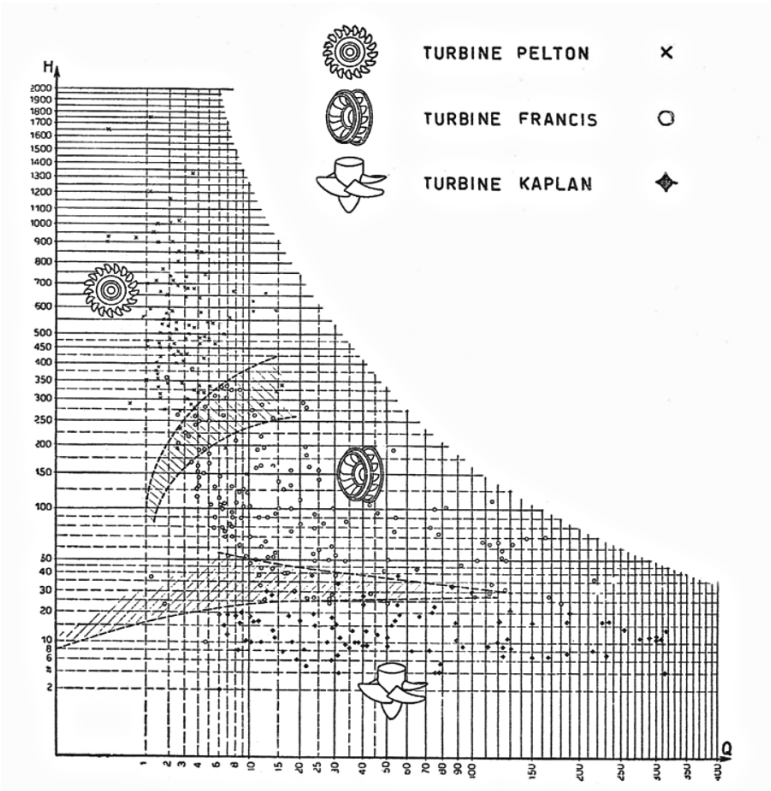

Figure 1.2: Turbine Classification on Their Motor Head and Flow Rate

Classification can be simplified by relating information to a single pa-

rameter. One option is to define the specific speed as follows:

$$N_s = \frac{n\sqrt{P}}{H^{\frac{5}{4}}} \tag{1.1}$$

where n is the rotational speed (rpm), P is the power (kW) and H the water head (m). According to what stated before, the Pelton turbine is characterized by the lowest N_s, the Kaplan one by the highest. Thus, wind turbines can technically be considered as an extreme extension of Kaplan turbines, where the specific speed reaches the highest value. A high specific speed implies that the turbine can deal only with small heads (denominator in N_s definition). This makes sense, because it can be inferred from experimental data that small heads imply high volumetric flow rates, which is trivially true for an *open* device as a wind turbine.

1.3 Horizontal Axis Wind Turbines

HAWTs represent more than 90% of wind turbines today. Broadly, the rotor hub is connected to a nacelle containing the generator, both of them positioned on top of a tower. Either synchronous or asynchronous machines can be used for connection to the electricity grid: the first solution allows avoiding the gearbox and is globally less noisy, but it is never preferred being much more expensive.

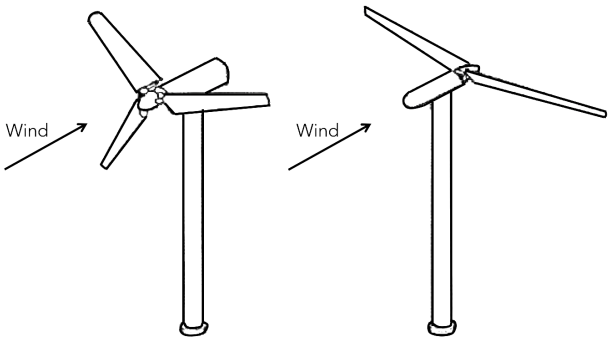

Figure 1.3: Upwind vs. downwind horizontal-axis wind turbine.

HAWTs are lift-based machines, i.e. revolution is mostly due to lift. For an easy understanding of this point, a comparison to airplane wings operation is useful. The result of a flow stream investing an airfoil is a difference in pressure, which in turn generates an overall aerodynamic force. This can be decomposed with reference to the direction of the relative speed between the fluid and the airfoil (in case also the airfoil is moving) into

a drag and a lift component, respectively aligned and perpendicular to it. Specifically, the lift force is the one that literally lifts the airplane up. Back to wind turbines, the working principle is exactly the same, but since the airfoil blades are secured to the hub, lifting is prevented. The consequence is that the acting force is converted into a rotational momentum (the only allowed degree of freedom), which spins the rotor. A drag force is actually generated as well, and balances the overall equilibrium during rotation. However, it always occurs if an object redirects the airflow coming at it, since motion implies an opposing force, but it does not contribute to the machine energetic output. This behavior also accounts for its appellation as induced drag force, meaning that it exists just because a lift force also exists.

The wider classification of HAWTs is based on their orientation being into the wind (upwind) or in its same direction (downwind), as shown by Fig. 1.3. In upwind machines, the rotor comes before the nacelle and is kept oriented against the wind with some yaw mechanism. Air passes through the blades first, with no previous deflection or interferences with other components, thus power losses are mostly inhibited. Also, since the blades swirl and decelerate the flow before it impacts the nacelle and the tower, the stress on these components is much relieved. However, due to this configuration, the blades might risk bending towards the tower, thus a more extended nacelle is required to keep rotor and tower well separated, as well as a very stiff connection between blades and hub. In downwind designs, instead, the rotor is located at the back. No yaw mechanism is needed, since the nacelle self-aligns stream-wise, and the blades do not risk striking the tower, so stiff connections can be replaced by much less costly solutions. On the other side, fatigue concentrates on the blades, and their flexibility is responsible for high turbulence. This implies lower efficiency that is the reason why upwind turbines are often preferred.

Today most successful HAWT is the upwind three-blade rotor, which reaches the highest efficiency thanks to a good blade design, aiming at reducing turbulence, and a careful choice of the materials. Indeed low inertial materials are used, which allow a prompt acceleration if the wind speeds up, such as laminated wood, composite materials or aluminum.

1.4 Vertical Axis Wind Turbines

These machines are just 10% of the overall wind turbines, but their architectures and design options are definitively much more disparate if compared to HAWTs. They also represent a much more recent innovation, but keeps growing thanks to the numerous benefits and chances of optimization they allow.

1.4.1 Benefits of Vertical Axis Design

First of all, the rotating shaft and the tower (often required to elevate the turbine to higher altitudes, where the wind is stronger) are aligned in the same direction, and not perpendicular to each other. This arrangement does not require any yaw mechanism to connect the two components nor particular support for the electrical generator and the gearbox, which can be simply placed at ground level. Costs are significantly reduced, since both the machine installation and the maintenance on these components are facilitated. In particular, the initial cost reduction is a crucial advantage, since the main factor preventing renewables from being incentivized is the huge initial investment on fixed capital. Indeed, this marks the difference between clean energy and fuel-based technologies, which instead involve relatively low initial expenses but high operational costs, extended throughout the whole estimated life of the plant. The key point is that, economically speaking, it is less ventured and more trusting to distribute the financial outlay on a long-term period and benefit from an averagely higher economical availability down-the-line in the working life of the machine, rather than relying on an initial-time full investment whose payback is expected in a long way off in time. This is the reason why investors are discouraged in investing on renewables. If relieving the initial investment on wind turbines has a much more trenchant effect on the overall expense than just caring about the operational costs, it is then evident why this point is of utmost importance.

Secondly, VAWTs are less sensitive to wind incidence, i.e. the turbine is able to intake the incoming airflow from all the directions. The selection of suitable sites is then wider, and even urban environments might be an option, thus paving the way for residential energy production.

In the end, VAWT blades move at relatively low speed if compared to HAWTs, which implies less noise and a minor influence on the ecosystem (these big installations affect birds' routes, which possibly should be kept unaltered).

Clearly, VAWTs exhibit numerous limitations as well, which will be deepened later, since a basic understanding of their structural features needs to be gained first. For instance, their aerodynamics is crucial, as it is characterized by instability and highly distorted and time-dependent wakes. Nevertheless, none of the downsides can be a reason for scaling this technology back. The counterparts to any successful innovation unavoidably come into play, but a solution is possible only with time. VAWTs showed off in a very

recent time and still need to be optimized, thus, at the state of the art, their merits are definitively worthier of attention than their handicaps. Similarly, this is the reason why also a comparison between HAWTs and VAWTs (or within any sub-category) is still not possible in a thorough way. Trivially, all the items fabricated to this moment rarely broke down and still work. Since the convenience of any technology is not only related to what it does, but also to its payback time, i.e. for how long it does it, it is still premature to infer a realistic estimate of their return on investment and of their overall benefit. Moreover, as stated in the introduction, the only estimation of their cost-effectiveness is often pointless, since their success today is mostly related to causes far off the economical one, such as ecology.

1.4.2 Classification of Vertical Axis Wind Turbines

The Savonius and the Darrieus shapes are the main designs for VAWTs. To describe the first one, it is useful to think of cutting a hollow cylinder lengthwise in two specular C-shaped parts and then offsetting the two halves to arrange them in a S configuration. The Darrieus rotor, instead, uses two or more vertically oriented airfoil-shaped blades, revolving around the mast. One option is that blades are curved to have their ends directly connected to the hub, and this solution is known as the egg beater design, for understandable reasons. Alternatively, blades can stand out as separate objects from the hub and are connected to it by means of struts, located at intermediate span heights. If the blades are straight (i.e. untwisted and with uniform section), the arrangement is known as giromill or H-bar design. If they are bent into a helix shape swirling around the mast, this configuration is simply denoted as helical-blade design.

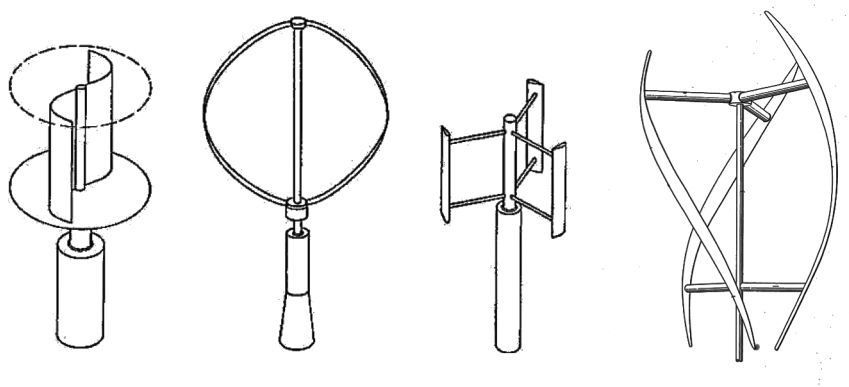

Figure 1.4: From left: Savonius, Egg-Beater, H-Darrieus (Giromill) and Helical-blade designs.

Savonius and Darrieus rotors have a completely different aerodynamic behavior. The Savonius rotor is operational due to drag forces, meaning that it rotates because the wind pushes the blades. On contrary, the Darrieus rotor is a lift-based machine, thus the same observations on HAWTs' aerodynamics hold for this case. The different working principle is the reason for the discrepancy in their performances, which will be discussed in the next chapter.

1.4.3 Issues of Vertical Axis Design

It is a matter of fact that VAWTs struggle to reach a high efficiency, even if in some typologies it actually halts just slightly below the values for HAWTs. In Savonius rotors, this limitation is the foregone counterpart to a too simplistic design that is responsible for high turbulence. Darrieus models, instead, benefit from a more favorable design based on airfoil blades, but they still do not reach HAWTs efficiency values. The point is that, while HAWTs' blades always face the wind with the optimal blade tilt angle (no matter the rotor angular position), in Darrieus turbines the wind incident angle on blades changes during revolution, implying that at each moment only part of the turbine is working and another part is dissipating. From another point of view, if HAWTs' circular swept area always faces the wind, on contrary VAWTs' swept area is represented by a rectangular area (rotor diameter times the blade span) whose *active* portion that faces the wind changes during revolution, implying that the swept area is never involved in its whole into the energy conversion process. Typical values for efficiency are then 10-15% for Savonius rotors vs. 25-30% for Darrieus, still below the value of 35% that can be achieved by HAWTs.

VAWTs design also involves another counterpart, regarding the machine overall structural resistance. In HAWTs, the blades are secured to the hub at one end and free at the other. Thus, the centrifugal force generated by rotation weights on the blades proportionally to the distance from the free end, i.e. the blades are mainly stressed at the juncture with the hub. By progressively increasing the blades' thickness consistently, the force can be easily distributed in a more uniform way. On contrary, VAWTs blades are always secured to the hub at two or more intermediate points of their span (no matter if at both their ends or by means of struts). The centrifugal force, indeed, mainly concentrates at the blade mid-span, but no solution for strengthening this part is possible without spoiling the aerodynamics of the whole machine and consequently its efficiency. This problem is more evident in Darrieus than in Savonius turbines, since lift-based machines normally spin at higher rotational speeds and consequently are more sensitive to centrifugal stress. Nevertheless, it is also true that high rotational speed generally couples with low torque, which prevents more from wear and tear.

For this reason, despite the sensitiveness to the centrifugal force, in the end Darrieus turbines appear to be globally more resistant than Savonius ones.

The only disadvantage involved by low torque is the inability to self-start. Savonius rotors are able to power up by themselves, when the wind exceeds a certain speed. Darrieus turbines, instead, require more sophisticated solutions, such as variable-pitch blades whose orientation about their axis can be regulated depending on wind conditions (subcategory of giromill rotors known as cyclo-turbines). An interesting solution that combines the qualities of both the two groupings is the invention of hybrid models. A Savonius rotor is mounted into the Darrieus one, and both spin around the same mast. Thus, the first provides the run-up to the cruising speed, and the second comes to play eventually. The overall machine is able to self-start and at the same time achieves a satisfactory efficiency level.

It is interesting to notice that the evolution of VAWTs traces all the issues just discussed. The first model has been the curved-blade eggbeater. The transition to H rotors occurred because straight blades manage to distribute the wind aerodynamic force more equally span-wise. Nevertheless, this model introduced the issue of the sensitivity to centrifugal stresses. So, helical-blades have been designed, which are still independent from the hub as in H-rotors, but not straight anymore. By swirling around the mast, they distribute the torque more evenly and prevent from destructive pulsations during revolution.

Chapter 2

Theoretical Aspects of Wind Turbines

The aim of this chapter is to provide an analytical description about the energetic behavior of wind turbines. To this purpose, the actuator disk theory has set the benchmark in wind-technology analytical modeling, since still today it represents the trust-worthiest theoretical approach among the available ones, and possibly the best framed in a context in which still now theory building seems to be unapproachable. It cannot be considered as an exhaustive analysis though, but it does represent a simplistic validated description of energetic interaction between turbines and fluid flow. However, it is important to point out from the outset that this method has been developed for HAWTs and no extension to VATWs has been acknowledged yet. Nevertheless, very recently, the idea that this theory might actually be extended as is to VAWTs as well is fighting its way. Thus, the first goal of this chapter is to explain the theory on hand, but a brief critique about its applicability will also provided.

2.1 The Actuator Disk Theory and the Betz efficiency limit

Let us consider a HAWT, crossed by a fluid flow that is assumed as uniform, incompressible and steady [6]. It is already evident that all these assumptions are definitively a stretch if dealing with air, but at the state of the art a more detailed investigation of such a complex phenomenon is still not possible analytically.

If wind turbines are investigated, two issues must always be considered: there is no stator upstream and the rotor is not ducted, thus the mass flow rate is not an assigned design choice. The first goal is then the identification of the fluid stream that crosses the machine. The mass flow rate is only

known at the rotor section, since its swept area can be used as a reference for its computation. This value, denoted as $\dot{m}_D$, will then quantify the fluid throughout the whole machine. In practice, by selecting all the upstream and downstream cross sections whose mass flow rate equals $\dot{m}_D$, a stream tube can be identified, so that the machine can be treated in the same way as ducted turbines (Fig. 2.2). The duct section enlarges downstream since, by impacting the rotor, the fluid decelerates without changing its density. If the mass flow is constant, then the section must increase.

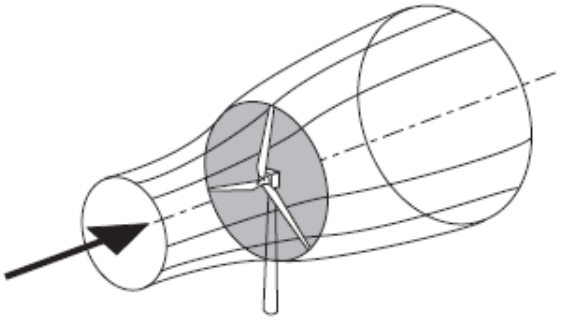

Figure 2.1: 3D view of the Wind Stream Tube across a HAWT

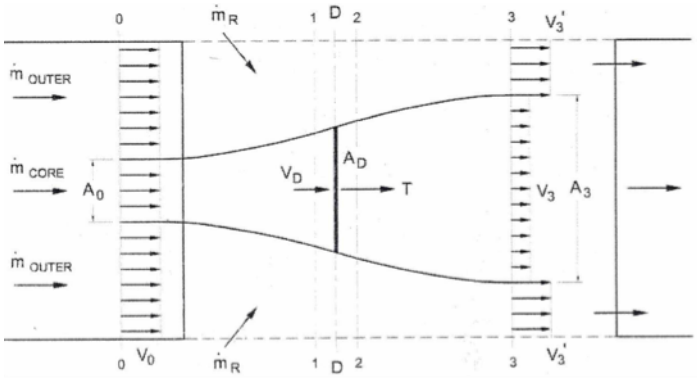

Figure 2.2: Wind Stream Tube [2]

This method allowing the selection of a fictitious duct for the machine by applying the mass conservation law to the whole path, is a reverse procedure with respect to standard analyses. In fact, this principle normally applies to fluids confined in space, but cannot be used to select that space. This way, theory is being inferred by studying an already existent machine, while the machine behavior should be better estimated *in order to* design the machine itself. This limitation is exactly the reason why still today wind

turbine design is mostly achieved through experimental tests and optimization is difficult.

An important hypothesis related to the stream tube is that properties are assumed not to change within the same cross section. In other words, given a section of the duct, the properties of the point centered on the machine axis extend to all the points belonging to that section, and a discrete change occurs at its boundaries. This is definitively an unrealistic hypothesis (for instance, two points at infinitesimal distance cannot have different pressure), but it allows downgrading the overall problem to one dimension.

Thus, let us select sections 0 and 3 to be considered as the machine inlet and outlet. They are just required to be far enough from the rotor upstream and downstream, i.e. where the velocity gradient in the axial direction is negligible. If the pressure has the same value in both the two sections (Eqs. 2.1, 2.2), it can then be inferred that the work done by the machine equals the kinetic energy subtracted from the fluid. This work is quantified by the the *motor head*, as defined in Eq. (2.3):

$$P_3 = P_0 = P_{atm} \tag{2.1}$$

$$P_3 - P_0 = 0 \tag{2.2}$$

$$H_m = \frac{v_3^2 - v_0^2}{2} \tag{2.3}$$

By focusing instead on the inner region of the machine, the fluid is expected to stagnate when impacting the rotor, and its velocity reduction should correspond to an increase in pressure. However, by rotating slowly, the blades are not able to halt the fluid, so that the velocity does not experience any leap at the rotor section, but gradually decreases all along the downstream path. At the same time, the pressure increases only slightly before the rotor, since no stagnation occurs, but what mostly matters is that it experiences a sharp drop right after it. In the end, the kinetic energy lost by the fluid cannot be retrieved, since it has been converted to mechanical work for the turbine, while the pressure rises back to its initial value, to adjust itself to the atmospheric value. The pressure rise is also responsible for a sort of diffusive effect, which further contributes to the velocity reduction (Fig. 2.3).

By observing this behavior, it is possible to infer that dissipation is the only reasonable explanation for it. Indeed, let us consider sections 1 and 2, being the closest to the rotor, upstream and downstream. The Bernoulli theorem states that, in case no dissipation occurs, the fluid overall energy T

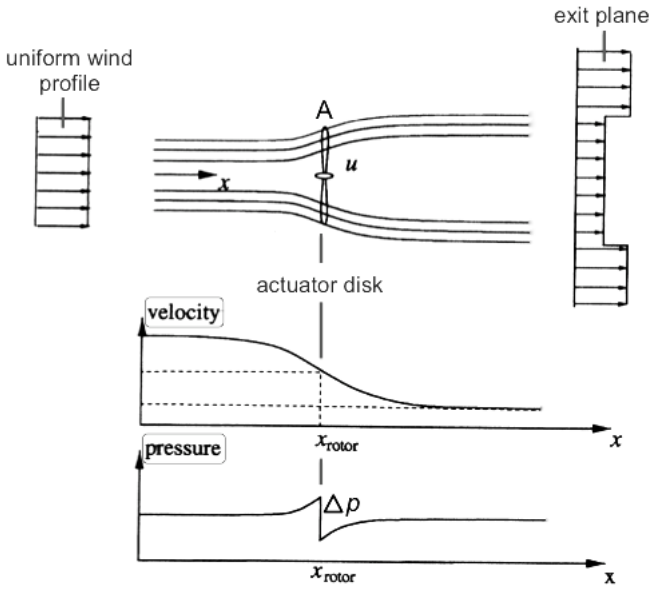

Figure 2.3: Velocity and Pressure Trends Across the Actuator Disk [15]

must be conserved stream-wise. If losses, instead, are purposely introduced at the rotor section, T has to decrease (Eq. 2.4). No potential energy is included in T, but only kinetic and pressure energies are taken into account (Eq. 2.5).

$$T_2 < T_1 \tag{2.4}$$

$$\frac{P_2}{\rho} + \frac{v_2^2}{2} < \frac{P_1}{\rho} + \frac{v_1^2}{2} \tag{2.5}$$

Since section 1 and 2 are at infinitesimal distance from each other, they have the same area. Also, for the same reason, the fluid does not experience noteworthy changes in density. From the mass continuity equation (Eqs. 2.6, 2.7), it is then inferred that velocity cannot be subjected to any sharp variation in the vicinity of the rotor (Eq. 2.8), which confirms what has been observed physically.

$$\dot{m}_1 = \dot{m}_1 \tag{2.6}$$

$$\rho_1 v_1 S_1 = \rho_2 v_2 S_2 \tag{2.7}$$

$$v_1 = v_2 \tag{2.8}$$

By putting the results together, Eqs. (2.5) and (2.8) account for the pressure drop experienced by the fluid, thus implying that dissipation is a

realistic explanation.

$$P_2 < P_1 \tag{2.9}$$

It now stands to reason that, differently from other turbines, a wind turbine behaves more similarly to an actuator disk purposely causing an energy loss to the flow. For this reason, standard modeling that applies to other machines does not hold for this case, and the turbine is better modeled as a porous disk. It is now possible to write the momentum balance for the control volume in-between section 1 and 2:

$$\left[\int_{s_1} \rho\overrightarrow{\mathbf{v}}(\overrightarrow{\mathbf{v}}\cdot\overrightarrow{\mathbf{n}})dS + \int_{s_2} \rho\overrightarrow{\mathbf{v}}(\overrightarrow{\mathbf{v}}\cdot\overrightarrow{\mathbf{n}})dS = \overrightarrow{T} + \int_{s_1} -P\overrightarrow{\mathbf{n}}dS + \int_{s_2} -P\overrightarrow{\mathbf{n}}dS\right]\cdot\dot{m}_D\cdot\overrightarrow{i} \tag{2.10}$$

T is the aerodynamic force applied from the machine to the fluid. By switching to a lumped parameter approach, Eq. (2.10) becomes:

$$\rho v_1(-v_{1n})S_1 + \rho v_2(-v_{2n})S_2 = T + P_1S_1 + P_2S_2 \tag{2.11}$$

$$\dot{m}(v_2 - v_1) = T + (P_2 - P_1)S_{disk} \tag{2.12}$$

$$T = (P_2 - P_1)S_{disk} \tag{2.13}$$

A similar procedure applied to sections 0 and 3 leads instead to Eq. (2.14):

$$T = \dot{m}(v_3 - v_0) \tag{2.14}$$

In the following algebraic passages, Eqs. (2.13) and (2.14) will be related to each other. To this purpose the Bernoulli equation is also taken into account. Indeed, it does not apply to the path 1-2, but it still holds for 0-1 and 2-3, since losses are only concentrated at the rotor section.

$$\frac{P_0}{\rho} + \frac{v_0^2}{2} = \frac{P_1}{\rho} + \frac{v_1^2}{2} \tag{2.15}$$

$$\frac{P_2}{\rho} + \frac{v_2^2}{2} = \frac{P_3}{\rho} + \frac{v_3^2}{2} \tag{2.16}$$

Eq. (2.13) is then modified, by using the results from Eqs. (2.15) and (2.16):

$$\begin{aligned} T &= (P_2 - P_1) = S_{disk} = && (2.17)\\ &= \rho\left(\frac{P_3}{\rho} + \frac{v_3^2}{2} - \frac{v_2^2}{2} - \frac{P_0}{\rho} - \frac{v_0^2}{2} + \frac{v_1^2}{2}\right)S_{disk} = && (2.18)\\ &= \rho\left(\frac{v_3^2}{2} - \frac{v_0^2}{2}\right)S_{disk} && (2.19)\\ & && (2.20) \end{aligned}$$

By equating the formulations of T expressed by Eqs. (2.14) and (2.17):

$$T = \dot{m}(v_3 - v_0) = \rho(\frac{v_3^2}{2} - \frac{v_0^2}{2})S_{disk} \tag{2.21}$$

$$\rho S_{disk} v_{disk}(v_3 - v_0) = \frac{1}{2}\rho S_{disk}(v_3 + v_0)(v_3 - v_0) \tag{2.22}$$

$$v_{disk} = \frac{1}{2}(v_3 + v_0) \tag{2.23}$$

The result is that velocity at the rotor section can be computed as an average between its values far upstream and downstream. This value is known as Froude velocity. An estimate of the power, instead, is provided here:

$$\begin{aligned} W &= T \cdot v_D = \\ &= \dot{m}(v_3 - v_0) \cdot \frac{1}{2} \cdot (v_3 + v_0) = \\ &= \rho S_D v_D \cdot (v_3 - v_0) \cdot v_D = \\ &= \rho S_D v_D \cdot ((2 \cdot v_D - v_0) - v_0) \cdot v_D = \\ &= \rho S_D \cdot 2(v_D - v_0) \cdot v_D^2 < 0 \end{aligned} \tag{2.24}$$

It is now possible to define a parameter, known as *axial induction factor* and denoted with a, which represents the velocity reduction percentage caused the porous disk with respect to the undisturbed upstream flow velocity. It must be said that this parameter collects the effects many factors affecting the machine behavior and is extremely difficult to estimate in practice. To the purposes of this analysis, however, it is fundamental to simplify equations and highlight the key points.

$$a = \frac{v_0 - v_D}{v_D} \tag{2.25}$$

The power ideally generated by the turbine is then given by Eq. (2.26):

$$|\dot{W}| = \rho S_D v_0^3 \cdot 2a(1 - a)^2 \tag{2.26}$$

So, efficiency can now be computed as the ratio between the power just defined and the ideal power computed by assuming that the fluid does never change its undisturbed velocity, i.e. by using v_0 instead of v_{disk} to define the mass flow rate.

$$|\dot{W}_0| = \dot{m}_D \cdot \frac{v_0^2}{2} = \rho S_D v_0 \cdot \frac{v_0^2}{2} = \rho S_D \frac{v_0^3}{2} \tag{2.27}$$

$$\eta = \frac{|\dot{W}|}{|\dot{W}_0|} = \frac{\rho S_D v_0^3 \cdot 2a(1-a)^2}{\rho S_D \frac{v_0^3}{2}} = 4a(1-a)^2 \tag{2.28}$$

The value of a that maximizes efficiency, according to this expression, is 1/3. If a equals this value, the maximum efficiency is given by the so-called Betz limit, provided by Eq. (2.29):

$$\eta_{max} = \eta(a = \frac{1}{3}) = \frac{16}{27} \cong 0.59 \tag{2.29}$$

Thus the ultimate conclusion of the actuator disk theory is that the maximum efficiency a wind turbine can achieve in ideal conditions (no viscosity, reversible process, etc.) is 59%. Since very strong hypotheses have been made and in reality friction comes to play, it can be then understood why real applications halt far below this value. Thus, reality is even less rosy than the already bad situation depicted by this theory.

2.2 Does the Betz Limit Apply to Vertical Axis Wind Turbines?

The actuator disk model, from which the Betz limit is derived, has not been developed for VAWTs directly. However, on the one hand no similar theory exists nowadays which applies to them, and on the other hand the idea that an analogous approach should also be followed for VAWTs is strengthening up. Due to the growing number of different turbine designs, there is an actual need to develop a similar description of the flow behavior for VAWTs, and at the moment, the most accredited belief is that the actuator disk theory might be suitable as a starting point to this case as well.

Indeed, there are a lot of substantial differences to be considered, but most of the assumptions made by the theory can actually be easily extended on the whole. Of course, the simplicity and ideality of its hypotheses help the cause, that is, a lot of researches today agree that even if this method has been developed for a specific class of turbines, the problem has been simplified to such an extent that a generalization of the results is possible. To further specify, no turbine modeling is considered, but just the fluid behavior upstream and downstream is taking into account. If the machine is just a porous disk introducing losses, then its horizontal or vertical arrangement is no more crucial. After all, no matter its shape, in ideal conditions, any turbine would decelerate the flow and totally convert the kinetic energy subtracted from the fluid into mechanical power.

In other words, the real issue is in the unrealistic assumptions, such as the fact that the wind impacts the turbine in the axial direction and even

downstream no swirl is taken into account. Thus, before wandering about the suitability of this model for other kind of turbines, the question should be about its applicability within the class of turbines for which it has been developed. If all the strong hypotheses behind it are accepted, then its extension to other turbines such as VAWTs should be a smaller issue.

2.3 Aerodynamics Overview

In this section, a brief overview of the most important aerodynamic coefficients is provided. An insight into the H-type Darrieus rotor behavior will be also given.

2.3.1 Aerodynamic Coefficients

The power extracted from the turbine is given by Eq. (2.30). T represents the overall torque applied to the turbine and ω is its rotational speed.

$$P = T \cdot \omega \tag{2.30}$$

One of the most significant aerodynamic quantities is the coefficient of power C_P. In Eq. (2.31) ρ represents the fluid density, A is the machine swept area and v_0 is the far upstream fluid velocity (prior to undergo variations due to presence of the turbine).

$$C_P = \frac{P}{\frac{1}{2}\rho A v_0^3} \tag{2.31}$$

Being dimensionless, this parameter allows comparing performances of different turbines, no matter their dimensions or the wind conditions. The numerator represents the power extracted de facto, while the denominator is the overall power carried by the undisturbed upcoming fluid flow. Therefore, this coefficient represents the extracted power fraction compared to the extractable amount, this latter being the kinetic power of the far wind. As expected, its maximum value must coincide with the Betz limit. Similarly, it is possible to define a coefficient of torque, as shown in Eq. (2.32), where R is the machine radius.

$$C_T = \frac{M_t}{\frac{1}{2}\rho A R v_0^2} \tag{2.32}$$

It must be highlighted that, if a high coefficient of power does always represent an evidence of good functioning, the torque cannot be a univocal estimate of the machine performances. For instance, small torque is often desirable in order to relieve the structural stress on the turbine. However, in many situations the ability to self-start is also required and can only be

achieved if the torque is high enough. In the end, also lift and drag forces do have a dimensionless equivalent too, as shown in formulae (2.33) and (2.34):

$$C_D = \frac{D}{\frac{1}{2}\rho A w^2} \tag{2.33}$$

$$C_L = \frac{L}{\frac{1}{2}\rho A w^2} \tag{2.34}$$

In these expressions, w is the wind relative speed computed at the blade tip. In Eq. (2.35) v_0 represents far upstream wind velocity and u is the blade tip speed. The reason is the coherency with the numerators, as lift and drag conventionally represent a decomposition of the overall aerodynamic force F with regard to the direction of w and not v_0.

$$\overrightarrow{w} = \overrightarrow{v}_0 - \overrightarrow{u} \tag{2.35}$$

The coefficients of lift and drag might help compare different turbines if they are interpreted as an estimate of how the net force distributes into the two components. However, a more proper reading of these coefficients is on the behavior of a given machine at different operating conditions. For instance, given an airfoil, both the two coefficients hugely vary with the flow angle of attack, hence they truly represent an estimate of the *active* portion of the machine area that is involved in lift or drag generation.

2.3.2 Insight into the H-type Darrieus Rotor: Comparison to Other Machines

The coefficients of power and torque are typically evaluated as functions of the tip speed ratio, denoted by TSR or λ.

$$TSR = \frac{u}{v_0} = \frac{R \cdot \omega}{v_0} \tag{2.36}$$

Fig. (2.4) shows that each configuration is operational within a specific range of λ and that two machines working at the same λ might perform very differently. As discussed in Ch. 2.3.1, a high C_P is nothing but the goal a wind turbine aims at, so it is always trivially beneficial. On contrary, a small C_T is generally desirable, but a high one would allow self-starting. As expected, HAWTs possess the best performance parameters, while the Savonius models are the most slow-running machines and stand out for the lowest power output and the highest torque. In this framework, Darrieus rotors result as much more performing than other VAWTs, to the extent that, in terms of C_P and C_T, they should be better compared to HAWTs. Indeed, they are almost as efficient as horizontal-axis turbines.

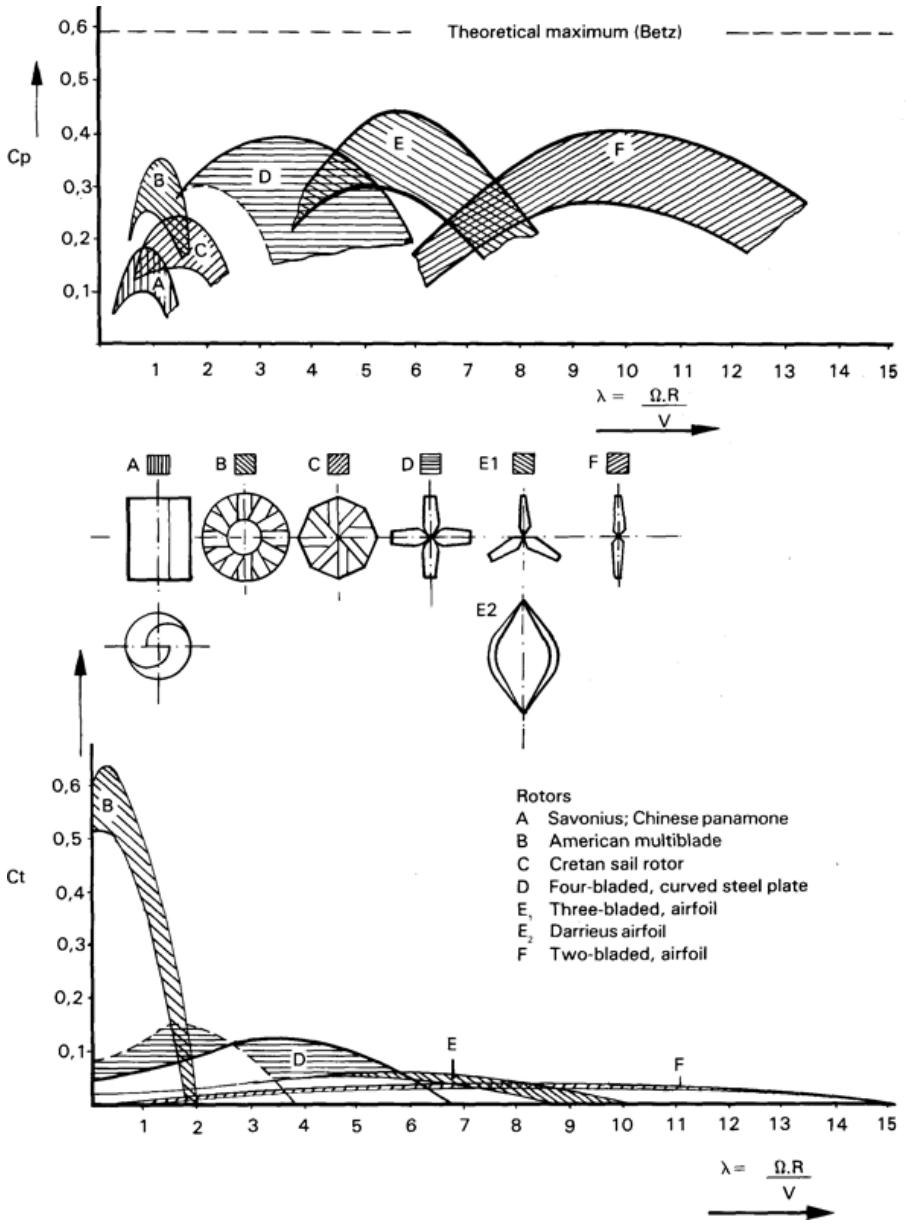

Figure 2.4: Coefficients of Power and Torque as a function of λ

Chapter 3

Governing Equations

CFD is a branch of fluid mechanics that aims at implementing numerical methods to solve problems where fluid flows are involved. This diverse set of techniques gained a foothold in recent times, since it often provides the only possible solution to problems that cannot be solved analytically. Numerous CFD software packages have been developed until today, and specifically the open-source code OpenFOAM®has been chosen for this thesis. Despite the peculiarities of each code, their physical and operational baselines are very similar to one another.

The goal of this chapter is to briefly illustrate the Navier-Stokes equations and how the physical problem is addressed in numerical codes, by introducing the finite volume method. Also, the main turbulence models will be broadly discussed. In the end, an insight into the model used for this thesis, namely *Dynamic Length Resolution Model*, is provided.

3.1 The Navier-Stokes Equations and the Finite Volume Method

The Navier-Stokes equations are a set of coupled differential equations that describe how velocity, pressure, temperature and density of a moving fluid are related. They also take unsteadiness and viscous effects into account. The short formulation is only made up by two equations, but the fluid three-dimensionality is inherently included. The first equation comes from the continuity principle, which states that the mass variation within a confined volume Ω always balances its net flux through its boundaries $d\Omega$. If the flow is incompressible, the result is shown by equation 3.1, where $\mathbf{U}$ is the fluid velocity vector [9].

$$\frac{\partial u_i}{\partial x_i} = 0 \tag{3.1}$$

The second equation is derived from the momentum equation, which

states that the total momentum is constant in closed systems. Equation 3.2 provides the simplified expression for incompressible flows, where p denotes the fluid pressure, ν is the dynamic viscosity and $\mathbf{b}$ the body forces.

$$\frac{\partial u_i}{\partial t} + \frac{\partial \left(u_i u_j\right)}{\partial x_j} = -\frac{1}{\rho}\frac{\partial p}{\partial x_i} + \frac{\partial}{\partial x_j}\left(\mu \frac{\partial u_i}{\partial x_j}\right) + b_i \tag{3.2}$$

The Navier-Stokes equations represent a comprehensive description of the fluid dynamics, but an analytical solution still does not exist for the general 3D case. In fact, analytical solutions have been derived just for specific simple cases, and it would be incorrect to extend them to cases with even slightly different ground hypotheses.

Thanks to the advancements in computer sciences, a new approach has been adopted. Today, the *finite volume method* allows evaluating partial differential equations in the form of algebraic ones, by discretizing them in both time and space. Indeed, solutions are computed at discrete points on a meshed geometry and result from a numerical procedure over time, which starts from specified initial and boundary conditions.

The time derivative term appearing in the Navier-Stokes equations is often discretized with a first-order backward Euler scheme, even if more sophisticated and higher-order schemes are also available. In Eq. (3.3) the apices denote the time-steps, and Δt is the time step duration:

$$\frac{\partial \phi}{\partial t} \approx \frac{\phi^n - \phi^{n-1}}{\Delta t} \tag{3.3}$$

Space discretization, instead, is achieved by partitioning the physical domain in a number of small volumes of arbitrary shape, named *cells*, and the sought physical quantities (pressure, velocity, density) are computed at the centroids of each cell, while the fluxes of the extensive quantities are evaluated at the cell faces.

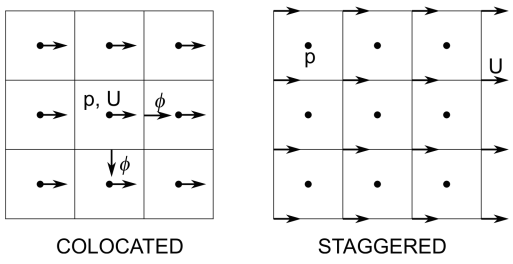

Figure 3.1: Colocated vs. Staggered Arrangement

This approach is called *collocated* and is the one implemented in OpenFOAM. It distinguishes from the *staggered* cell arrangement, since this latter associates velocity to the cell vertices (instead of centroids) to avoid some numerical issues (Fig. 3.1). Appropriate interpolation schemes are then implemented to discretize all the terms appearing in the equations (gradient, divergence and laplacian), but their analysis deviates from the objectives of this discussion.

The momentum equation cannot be reversed to a function of pressure, since it can only be solved for the pressure gradient. The pressure field is then obtained by exploiting its correlation with velocity, set by the momentum equation itself. In doing so, a key point to consider is that this correlation is also conditioned by the mass conservation. In fact, this latter represents a kinematic constraint on the velocity field, thus in turn the pressure field must be built accordingly. This problem is known as *pressure-velocity coupling* and allows combining continuity and momentum to derive an equation for pressure. With some pure algebraic manipulation, and assuming density and viscosity to be constant, the simplified Poisson equation is derived:

$$\nabla^2 p = -\rho \frac{\partial^2 \left(u_i u_j\right)}{\partial x_i x_j} \tag{3.4}$$

There exist diverse strategies to implement this coupling algorithm. In the specific case of *OpenFOAM*, segregated solvers like *SIMPLE* and *PISO* follow a pressure-correction model, as follows. The discretized momentum equation is given by 3.5:

$$A_P u_{i,P}^{n+1} + \sum_l A_l u_{i,l}^{n+1} = Q^{n+1} - \left(\frac{\partial p^{n+1}}{\partial x_i}\right)_P \tag{3.5}$$

where A is the coefficient matrix, with $P = 1...N_{cells}$ and $l = 1...N_{neighbors}$ of P. A *predicted velocity*, which does not satisfy continuity, is computed as shown in 3.6. By inserting it into the continuity equation, the Poisson equation for *corrected pressure* is derived, as shown in 3.7:

$$u*_{i,P} = \frac{Q^n - \sum_l A_l u_{i,l}^n}{A_P} - \frac{1}{A_P}(\frac{\partial p^n}{\partial x_i})_P \tag{3.6}$$

$$\frac{\partial}{\partial x_i}\left[\frac{\rho}{A_P}\frac{\partial p^{n+1}}{\partial x_i}\right] \tag{3.7}$$

In the end, *corrected velocity* is computed from *corrected pressure*:

$$u_i^{n+1} = \frac{Q^n - \sum_l A_l u_{i,l}^n}{A_P} - \frac{1}{A_P}\left(\frac{\partial p^{n+1}}{\partial x_i}\right)_P \tag{3.8}$$

3.2 Turbulence Modeling

Turbulence is an unsteady three-dimensional regime of motion, which occurs at high Reynolds numbers. Indeed, a 3D space allows sufficient flow stretching and turning for vortex generation and a low Re would imply viscous effects exceeding inertial effects, so that disturbances are prevented from spreading [22]. This phenomenon is chaotic, but not random [19]. The difference is slight, but fundamental for fluid dynamic modeling. A random phenomenon is governed by a probabilistic law and is not predictable either from a theoretical point of view. The most accurate prediction is that the system will be at condition X with probability Y. A chaotic phenomenon, instead, is deterministic, i.e. there exists a law prescribing its behavior as a function of its past history. The reason why *chaotic* is often confused with *random* is due to the strong dependency of the evolution law on the initial conditions: if small variations occur to the initial state, the final state will be so far from the expected one that the phenomenon appears to be random. Indeed, also in practice it is very difficult to distinguish, since measuring tools are often not accurate enough to appreciate differences in the initial state and, by repeating tests, the huge discrepancy in the results is justified by making the hypothesis of randomness.

From the point of view of CFD, the definition of turbulence as a *chaotic regime* implies that there must exist formulations to describe it deterministically: its behavior is irregular, but somehow universal [8]. Such a statement is also proved by the strong correlation to time/space as well as to initial/boundary conditions. However, at the state of the art, the causes for the *apparently random* behavior of turbulence have not been understood yet. For instance, it is still mostly unknown whether inaccuracy occurs to equations, to the way equations are solved, or to the way side conditions affect the solutions. For all these reasons, even if a deterministic approach would better fit the physics of the problem, a statistical approach is mandatory, i.e. in the end turbulence is treated as random. Specifically, statistics applies to the Navier-Stokes equations, as will be explained later on in this chapter. Fortunately, this compromise, due to the lack of knowledge about this complicated regime of motion, is supported by advanced computer and experimental tools, which definitively mark the difference with the past.

The first investigation of vortex structures was carried by Richardson in 1922. He introduced the idea that turbulence is made up by *eddies* of different sizes, which transfer energy to one another in a cascade manner [24]. First of all, no exact definition of *eddy* exists, but a proper characterization might be that of a local turbulent motion that is coherent to itself in a confined region, *i.e.* clearly included within an area with characteristic length l. Since the vortex is also associated to a velocity $u(l)$, a time scale

$t(l) = l/u(l)$ can be identified as well. Thus,vortices can be either classified depending on their length scale or their time scale. Thus, the *energy cascade* theory can now be introduced. The basic idea is that kinetic energy enters the largest scales of turbulence and is transferred by inviscid processes to the smallest ones. Only at this point, dissipation occurs.

By considering Richardson's work as a starting point, in the 40's, scientist Kolmogorov carried the first systematic analysis of turbulent flows, by especially focusing on the velocity field to investigate the evolution of the flow energetic spectrum. His work aimed at defining and categorizing vortices on the strength of their energetic content and their dissipative behavior. In other words, his goal was to set the threshold at which the dissipating mechanisms would replace conservative energy transfer processes [24] [28].

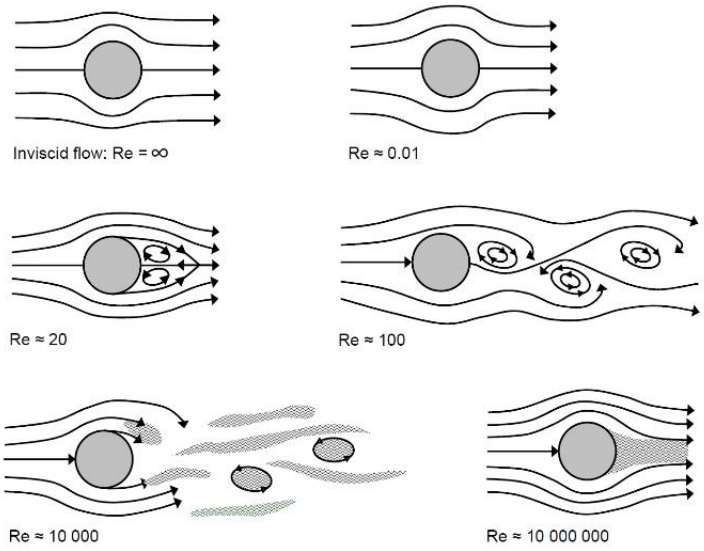

Figure 3.2: Turbulent flow past a bluff body as a function of the Reynolds number.

Three main class fields of eddies can then be identified. First of all, the so-called *integral* scale vortices correspond to the highest energy content and are the first to be generated. These low-frequency vortices are the same order of magnitude of the problem size (for instance, a fan initially produces vortices as big as its blades). Large vortices generate smaller vortices, at first with no dissipation. Since direct energy conversion occurs, the second class field is named *inertial*. Indeed, dissipation occurs only in the last step, when vortices result in being so little that they prevent kinetic energy from being further converted. Kinetic energy is then released from the flow in

form of heat, as a consequence of the higher viscosity as well as the higher frequency that characterize these scales. These eddies take the name from Kolmogorov himself, since he has been the first to identify and categorize them. Indeed, on the one hand, he agreed that an *eddy* preludes any definition [24], but on the other hand he managed to trace out some unmistakable common properties. For instance, in sufficiently small domains, isotropy is a good approximation for the behavior of vortices [17].

As it might be expected, the dimensions of the vortices (and consequently the way they distribute among the listed class fields) are highly affected by the Reynolds number, indeed representing the ratio of inertial forces to viscous forces. Specifically, the bigger its value is, the more extended the inertial scale interval will be, which means that there is a complete distinction between the two frontier characteristic scales and most of the vortices is characterized by intermediate dimensions. The most widely used turbulence models intrinsically make a distinction among scales and provide different in-built approaches depending on the vortex size. For instance, the same model might resolve some scales and model some others. For this reason, the high Reynolds condition results in being the most favorable to allow modeling and to verify the consistency between theory and experimental measurements on the energy spectrum. On contrary, the extension of these models to low-Reynolds flows is often inappropriate, since they are characterized by a non-clear distinction between dissipative and non-dissipative scales, and above all by an overall small dissipation [25].

In the following subsections, the two main turbulence families will be introduced, namely the *Reynolds Average Navier-Stokes* and the *Large Eddy Simulations*. Alongside with all the other techniques existing today, they have been implemented to be used as an alternative to the so-called *Direct Numerical Simulations*, which have the disadvantage of a very high computational cost. In fact, DNS aim at resolving all the possible eddy scales up to the Kolmogorov sublayer and, as an implication, they give optimum results in terms of both completeness and accuracy. However, in most cases their cost is not affordable in terms of high-level computer resources available or it might be considered not worthy for the investigation purposes. Thus, RANS and LES have been thought up to avoid such an expense, but of course they introduce some approximation, which translates to less data information and less accuracy. From a very broad point of view, the first method decomposes motion into an average value to be computed and fluctuations to be modeled, while the second method distinguishes large scales to be resolved from small ones to be modeled. A deeper insight is provided as follows.

3.2.1 RANS models

A time-averaged description of the flow is often satisfactory for investigation purposes. Thus, RANS models are based on a simplified formulation of the Navier-Stokes equations, obtained by decomposing each instantaneous variable into a mean value and a fluctuating term [5]. Formula 3.9 shows how this decomposition applies to the velocity field and to pressure.

$$u_i = U_i + u' \tag{3.9a}$$
$$p = P + p' \tag{3.9b}$$

The definition for the mean value given by Reynolds is shown by Eq. (3.10) in its *continuous* formulation and by Eq. (3.11) in the *discretized* form.

$$U(t) = \lim_{T\to\infty} \int_0^T u(t)dt \tag{3.10}$$

$$U(N) = \lim_{N\to\infty} \frac{1}{N} \sum_{i=1}^{N} u_i \tag{3.11}$$

Eqs. 3.10 and 3.11 are used for steady flows. If a transient flow is investigated, the *Unsteady Reynolds Average Navier-Stokes* (URANS) is used, and the new formulation for the mean value is provided by Eq. (3.12).

$$U(t) = \frac{1}{\Delta} \int_t^{t+\Delta t} u(\tau)d\tau \qquad \Delta t = fixed \tag{3.12}$$

The given definitions for the mean value satisfy the following properties, which are fundamental for the next passages: the mean value for u is U (3.13), the mean value for u' is null (3.14) and linear mapping holds (3.15).

$$< u >= U \tag{3.13}$$
$$< u' >= 0 \tag{3.14}$$

$$\langle u + v \rangle = U + V \tag{3.15a}$$
$$\langle cu \rangle = cU \tag{3.15b}$$

Therefore, the momentum Navier-Stokes equation becomes:

$$\frac{\partial U_i}{\partial t} + \frac{\partial \left(U_i U_j\right)}{\partial x_j} = -\frac{1}{\rho}\frac{\partial P}{\partial x_j} + \frac{\partial}{\partial x_j}\left(\mu \frac{\partial U_i}{\partial x_j}\right) + \frac{\partial \left(\langle u_i' u_j' \rangle\right)}{\partial x_j} \tag{3.16}$$

It can be noticed that the decomposition does not lead to just –let us say– a *duplicated* Navier-Stokes equation. Indeed, the new equation looks very similar to the original one, except for the fact that all the terms are now averaged in time and, moreover, a new term $\partial\langle u_i' u_j'\rangle/\partial x_j$ shows up. The reason for it is that, due to the properties listed above (3.13 to 3.15), the fluctuation terms combine and cancel with each other, all but the term pointed out. Specifically, this corresponds to the divergence of the Reynolds stress tensor, already divided by density. This tensor is usually denoted by τ_{ij} and its definition is given by Eq. (3.17).

$$\tau_{ij} = \rho\langle u_i' u_j'\rangle \tag{3.17}$$

To give a physical interpretation to it, how stresses distribute in a moving flow must be investigated. If the flow is still, the only possible stress is pressure, which applies to any surface along the normal direction. On contrary, for a moving flow, friction in-between adjacent layers moving at different velocities gives rise to slanting forces, thus torques and corresponding stresses (3.3). Differently from elastic solids, for which stresses strictly depend on the actual strain on particles, fluid flow stresses depend instead on the deformation rate.

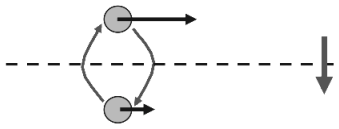

Figure 3.3: Differences in Velocities among Moving Particles produce a Net Momentum Transfer

To frame this interpretation into the Navier-Stokes equations, it can be stated that the Reynolds stresses quantify the kinetic energy transfer from the scales that almost resemble the average motion to the smallest turbulent scales that dissipate energy. Thus, the obtained momentum equation is a time-averaged equation with the addition of a single term that sums up the overall effects of dissipation introduced by turbulence onto the flow velocity field.

3.2.1.1. The Boussinesq Assumption

The averaged momentum equation obtained implies a completely different perspective with respect to its original formulation. Navier-Stokes does represent a *closed* differential problem, while the new model adds 6 unknowns represented by the Reynolds stress tensor components (downgraded from a total number of 9, thanks to the tensor symmetry), thus leading to the

so-called *turbulence closure problem*. This issue is generally addressed by modeling the turbulent components as functions of the mean motion. In fact, since all the other terms of the equation are averaged in time, the idea is to make the equation uniform. In some models, a specific expression is developed for any component of the Reynolds stress tensor. However, a more efficient way would be to look at the overall dissipation due to the viscous effects of turbulence and replace the tensor with just a function of a scalar parameter, which collects all the information given by the tensor itself. The physical problem is still not over, since the value of this parameter needs to be quantified each time, depending on the specific case. However, the mathematical issue is addressed since a scalar quantity within an equation is definitively much more manageable if compared to a full tensor.

Precisely, let us consider the Reynolds stress tensor, as defined by Eq. (3.17). One of the strongest theories is the Boussinesq approximation, for which the Reynolds tensor is assumed to be proportional to the mean deformation rate tensor S_{ij} (3.18, 3.68). The proportionality factor, indeed, is represented by a scalar quantity named *turbulence eddy viscosity* μ_T.

$$\tau_{ij} = 2\mu_T S_{ij} + -\frac{2}{3}\rho k \delta_{ij} \tag{3.18}$$

$$S_{ij} = \frac{1}{2}\left(\frac{\partial U_i}{\partial x_j} + \frac{\partial U_j}{\partial x_i}\right) \tag{3.19}$$

In this formula, ρ is the fluid density, δ_{ij} is the *Kronecher delta* and k is the *turbulence kinetic energy*. This latter is defined as the sum of all normal Reynolds stresses, as provided by equation 3.20:

$$k = \frac{\langle u_i' u_i' \rangle}{2} = \frac{1}{2}\left(\langle u'u' \rangle + \langle v'v' \rangle + \langle w'w' \rangle\right) \tag{3.20}$$

The quantity μ_T is exactly the scalar to which the vector problem is downgraded and holds the overall effects of turbulence. It might be seen as an index of how much the fluid opposes an imposed deformation of its own particles through friction. Specifically, it is a *dynamic* viscosity, which means that, from a cause-and-effect perspective, the fluid resistance to deformation is evaluated strictly in its dependency on the fluid atomic structure and not on its kinematic behavior. In other words, μ_T gives information about the fluid nature and not about the fluid motion, which instead is described by the *turbulence kinetic viscosity* ν_T.

$$\nu_T = \frac{\mu_T}{\rho} \tag{3.21}$$

The value of μ_T is not univocal, and actually its estimation has given rise to different theories, all based on the Boussinesq assumption as the starting

point. For instance, the so-called *two-equation turbulence models*, such as the $k-\epsilon$ and the $k-\omega$, all come from this initial hypothesis. In those models, the time-averaged momentum Navier-Stokes equation provided by Eq.(3.16) is manipulated to the formulation expressed by Eq. (3.22), where a function of μ_T replaces the Reynolds stress tensor, as already stated. What makes the difference among the diverse models is clearly the estimate of this parameter. These models will be discussed in the next chapter.

$$\frac{\partial \mathbf{U}}{\partial t} + \nabla \cdot \mathbf{U}\mathbf{U} = -\frac{1}{\rho}\nabla P + \frac{1}{\rho}(\mu + \mu_T)\nabla^2 \mathbf{U} \tag{3.22}$$

The simplification introduced by the Boussinesq assumption hugely helps reduce the amount of computational cost, but it is important to notice that it still remains an approximation with all the related issues. For instance, the proportionality between stresses and deformation rate has been experimentally confirmed for simple flows only (e.g. straight ducts), but it usually does not hold for complex cases (such as ducts with strong curvatures). Broadly, a simple formulation, obtained by downgrading the overall vector problem to a single scalar variable, can hardly represent the set of possible cases in its entirety.

Another weakness is that even for simple cases, if the goal is to reduce the amount of data involved in direct simulations, then the completeness of the results cannot be demanded either, i.e. it is impossible to get information about the whole regime of turbulence. Specifically, according to [17], small scales are isotropic and approximately independent from boundary conditions and flow steadiness. Thus, their modeling is normally doable and correct. On contrary, large scales usually exhibit a dynamic behavior that is intrinsically connected to the global behavior of the flow stream and largely varies depending on the situation. For instance, it depends on the geometry of the boundaries, on the type of fluid, or on the option of dealing with either an internal or an external aerodynamic field. Thus, their modeling requires a careful calibration on the specific study case, and this is the reason why capturing the entire spectrum of turbulence through simplified numerical simulations is almost impossible. These considerations might be extended to all the turbulence models aiming at simplifying DNS, but they are especially evident in RANS models.

3.2.1.2. Two-equation models, $k-\omega$ SST

RANS models include different subcategories, namely the *linear viscosity* models, the *non-linear viscosity* models and the *Reynolds stress* models (RSM). The so-called *algebraic* models belong to the first grouping, and in turn they include *one-* and *two-equation* models. This chapter will give a brief overview of these latter, with the final goal of introducing the $k-\omega$

model specifically in the SST version proposed by Menter [21]. Thus, the focus is now on this method, since it partially enters the turbulence model used for the simulations carried out for this thesis work. Indeed, the so-called DLRM will eventually be discussed (see Ch. 3.2.1.3.)

Broadly, two-equation models describe the turbulence properties of the flow by means of two conservation equations, each referred to a specific unknown, depending on the chosen method. The two transported quantities account for the past history of the fluid flow, in terms of convection and diffusion of the turbulence energy. In most cases, turbulence is firstly characterized by the amplitude of its fluctuations in the velocity field. This is why the first transported quantity is straightforwardly the turbulent kinetic energy k, already defined in Eq. (3.20).

However, k does not provide any specification about the size of the vortices, thus it is straightforward that the second transported quantity should be an estimate of the eddy scales. Since a small vortex distinguishes from a large one because of its higher dissipation rate, a suitable quantity can be either the so-called *turbulence dissipation rate* ϵ, which indeed leads to the $k-\epsilon$ model, or the *specific dissipation rate* ω, which instead leads to the $k-\omega$ model. Let us consider ϵ first, as provided by Eq. (3.23). It specifically represents the rate at which the velocity fluctuations dissipate.

$$\epsilon = \nu \langle \frac{\partial u_i'}{\partial x_j} \frac{\partial u_i'}{\partial x_j} \rangle \tag{3.23}$$

As previously introduced, the key point of these methods is to provide an estimate for μ_T to be used in Eq. (3.22). In this case, the $k-\epsilon$ model relates μ_T to the two transported quantities, up to a constant C_μ, as shown by Eq. (3.24).

$$\mu_T = \rho C_\mu \frac{k^2}{\epsilon} \tag{3.24}$$

By replacing the Reynolds stress tensor with this definition of μ_T, the *turbulence closure problem* is over. In fact, Eq. (3.22) is converted into a set of two equations in the two unknowns k and ϵ, as shown by (3.25) and (3.26).

$$\rho \frac{\partial k}{\partial t} + \rho U_j \frac{\partial k}{\partial x_j} = \tau_{ij} \frac{\partial U_i}{\partial x_j} - \rho\epsilon + \frac{\partial}{\partial x_j} \left[(\mu + \mu_T/\sigma_k) \frac{\partial k}{\partial x_j} \right] \tag{3.25}$$

$$\rho \frac{\partial \epsilon}{\partial t} + \rho U_j \frac{\partial \epsilon}{\partial x_j} = C_{\epsilon 1} \frac{\epsilon}{k} \tau_{ij} \frac{\partial U_i}{\partial x_j} - C_{\epsilon 2} \rho \frac{\epsilon^2}{k} + \frac{\partial}{\partial x_j} \left[(\mu + \mu_T/\sigma_\epsilon) \frac{\partial \epsilon}{\partial x_j} \right] \tag{3.26}$$

$$C_{\epsilon 1} = 1.44 \quad C_{\epsilon 2} = 1.92 \quad C_\mu = 0.09 \quad \sigma_k = 1.0 \quad \sigma_\epsilon = 1.3 \tag{3.27}$$

Both the two equations include transport, production and dissipation terms, modeled as just shown. Moreover, each modeled term is also optimized by means of closure coefficients (see Eq. (3.27)), which are derived empirically to help get the closest to the experimental results.

To sum up, the $k-\epsilon$ model is definitively a robust method, easy to implement and very cheap from a computational point of view. However, it also exhibits some significant weaknesses. Basically, this model has been developed for flows characterized by high Reynolds numbers and it performs very poorly if this hypothesis does not hold. The problem is that, even if a fully turbulent flow is investigated, the proximity of walls usually does represent an issue, since the flow is slowed down. As a consequence, the $k-\epsilon$ approach needs to be reformulated in the near-wall regions and to this purpose some ad-hoc damping functions are used [20]. These are simply known as *wall functions* and will be discussed in the next chapter, alongside with the stability issues they involve. In the end, because of its underlying assumptions, the $k-\epsilon$ model is often not adequate for complex cases such as high adverse pressure gradients, separation and strong streamline curvatures.

A valid alternative to the $k-\epsilon$ model is then represented by the $k-\omega$ model, which overcomes some of the issues just discussed. Quantity ω, namely the *specific turbulence dissipation rate*, is firstly defined in correlation with ϵ:

$$\omega = \frac{\epsilon}{C_\mu k} \tag{3.28}$$

Therefore, the new definition for the eddy viscosity μ_T is:

$$\mu_T = \frac{\rho k}{\omega} \tag{3.29}$$

Similarly to the $k-\epsilon$ model, the $k-\omega$ one is formulated through a set of two equations that are functions of the transported quantities. Moreover, also in this case closure coefficients improve the reliability of the results in comparison with data from experimental tests. Equations 3.30 to 3.32 show the standard Wilcox model.

$$\rho\frac{\partial k}{\partial t} + \rho U_j \frac{\partial k}{\partial x_j} = \tau_{ij}\frac{\partial U_i}{\partial x_j} - \beta^* \rho k\omega + \frac{\partial}{\partial x_j}\left[(\mu + \sigma^* \mu_T)\frac{\partial k}{\partial x_j}\right] \tag{3.30}$$

$$\rho\frac{\partial\omega}{\partial t}+\rho U_j\frac{\partial\omega}{\partial x_j}=\alpha\frac{\omega}{k}\tau_{ij}\frac{\partial U_i}{\partial x_j}-\beta\rho\omega^2+\frac{\partial}{\partial x_j}\left[(\mu+\sigma\mu_T)\frac{\partial\omega}{\partial x_j}\right] \tag{3.31}$$

$$\alpha=\frac{5}{9}\quad\beta=\frac{3}{40}\quad\beta^*=\frac{9}{100}\quad\sigma=\frac{1}{2}\quad\sigma^*=\frac{1}{2} \tag{3.32}$$

To elaborate further on the meaning of ω, its first definition was given in 1942 by Kolmogorov, who defined it as "the rate of dissipation of energy in unit volume and time". He also referred to it as "some *mean* frequency" expressed by Eq. (3.33), where c is a constant and l the turbulent length scale. Indeed, the reciprocal of ω is the time scale on which dissipation of turbulence occurs [31].

$$\omega=c\frac{k^{1/2}}{l} \tag{3.33}$$

This method results in being more performing than the $k-\epsilon$ model, especially for wall-bounded and low-Reynolds flows. It is also superior if high adverse pressure gradients or separation are addressed, which makes it more suitable for external-aerodynamics problems. In the end, it benefits from an overall higher stability. One counterpart is that much attention needs to be paid in the mesh generation step, especially for what concerns mesh refinement near the walls, in order to allow the best performance of this method. However, the real shortcoming is its sensitivity to the inlet free-stream turbulence properties, which instead moderately affects the performances of the $k-\epsilon$ model.

In the end, the so-called *Shear Stress Transport* $k-\omega$ model (shortly $k-\omega$ SST) is worth being mentioned, since it is achieving resounding success in CFD simulations nowadays. This model does not simply represent a variant of the standard $k-\omega$ model, but it combines the pros of both this latter and the $k-\epsilon$ model. Indeed, it switches from a more performing $k-\omega$ model applied near-wall to a standard $k-\epsilon$ far away, by using a blending function to smooth the transition. In this way, it benefits from the high accuracy given by the standard $k-\omega$, but at the same time it does not bump into its common weaknesses in the free-stream. For instance, this method is especially well-appreciated when dealing with high adverse pressure gradients and separating flows. Improvements are still needed though, since the model is not appropriate for investigating flows with sudden changes in strain rate (stagnation regions and regions where the flow strongly accelerates) or rotating flows [20] [21].

3.2.1.3. Wall Functions

The *boundary layer* can be defined as an arbitrary region of the fluid domain where viscous effects, due to the proximity to a wall, are more pronounced with respect to external regions. According to Prandtl's definition, if the undisturbed flow velocity is identified, the boundary layer extends to all the fluid streamlines whose deceleration exceeds 1% compared to that velocity. Within the boundary layer the fluid behavior is affected by friction, outside of it the flow is inviscid.

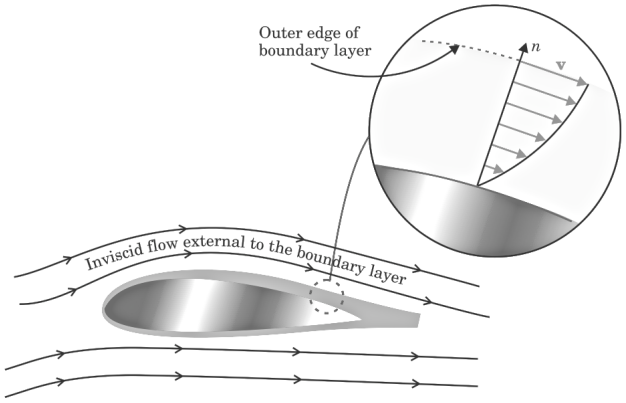

Figure 3.4: Boundary Layer on an Airfoil

Let us consider a fully turbulent flow. In this condition, viscous effects appear to be well-confined into a limited region adjoining the wall. Moreover, let us assume that the regime of motion is statistically stationary. In the end, let us investigate the velocity field in a local $x - y$ system on the wall boundary. By decomposing velocity into its mean value and its fluctuation, the Navier-Stokes equation holds as shown by equation 3.35:

$$u_i = U_i + u_i' \tag{3.34}$$

$$\rho\left(u_x\frac{\partial u_x}{\partial x} + u_y\frac{\partial u_x}{\partial y}\right) = -\frac{\partial p}{\partial x} + \frac{\partial}{\partial x}\left(\mu\frac{\partial u_x}{\partial x} - \rho u_x' u_x'\right) + \frac{\partial}{\partial y}\left(\mu\frac{\partial u_x}{\partial y} - \rho u_x' u_y'\right) \tag{3.35}$$

The following assumptions are taken into account:

$$u_x >> u_y \qquad \frac{\partial u_x}{\partial y} >> \frac{\partial u_x}{\partial x} \qquad \frac{\partial p}{\partial x} = 0 \tag{3.36}$$

Equation 3.35 becomes:

$$0 = \frac{\partial}{\partial y}\left(\mu\frac{\partial u_x}{\partial y} - \rho u_x' u_y'\right) \tag{3.37}$$

The first term in equation 3.37 is the *shear stress*, as defined by the Newton's law, while the second represents the *turbulent stress*. The overall stress, given by their sum, is constant throughout the boundary layer, as it can be inferred from the equation itself. It is important to notice that 3.37 is confirmed by experiments in the near-wall region only, and it does not apply far away, since out of the boundary layer stresses asymptotically tend to zero.

The goal now is to investigate how the two stress components combine with each other and in which regions one component appears to be prevalent to the extent that it might be considered as a good approximation of the whole stress. Indeed, if this occurs, it is possible to model that component only instead of the whole stress: this is exactly the approximation introduced by the so-called *wall-functions*. To these purposes, three regions with different stress behaviors, all within the boundary layer, can be identified:

- the *viscous sublayer*, representing the closest region to the wall;
- the *buffer layer*, which is the intermediate zone;
- the *log-law region*, corresponding to the most external layer.

Each region is treated differently. Indeed, the first one is characterized by negligible turbulent stress, so that the shear stress is only related to the fluid viscosity. It is basically an estimate of the fluid opposition to the deformation rate of its particles in accordance with the Newton's law (3.38).

$$\tau = \mu\frac{\partial u_x}{\partial y} \tag{3.38}$$

If both the two terms of the equation are divided by the fluid density, the right-hand side gains the dimensions of a square velocity. For the sake of convenience, in literature this fictitious velocity is referred to as *friction velocity* and denoted as u_τ, but this name only stems from its dimensions and not for the physics behind (3.40). The left-hand side, instead, keeps unaltered, except for the dynamic viscosity μ that is replaced by the kinematic ν.

$$u_\tau^2 = \nu\frac{\partial u_x}{\partial y} \tag{3.39}$$

$$u_\tau = \sqrt{\frac{\tau}{\rho}} \tag{3.40}$$

The following algebraic passages aim at defining two crucial quantities, namely $y+$ and $u+$, whose diverse correlations will characterize the stress behavior not only in this region, but also in the other ones listed above (3.43). In other words, by defining these two variables, the problem is standardized and the different cases are treated on a common ground. For the specific case on hand, this standardization process simply leads to a different but akin formulation of equation 3.39, which is exactly the law governing the viscous sublayer (equation 3.44).

$$\frac{u_\tau}{\nu} = \frac{\partial}{\partial y}\left(\frac{u}{u_\tau}\right) \tag{3.41}$$

$$d\left(\frac{u}{u_\tau}\right) = d\left(\frac{u_\tau y}{\nu}\right) \tag{3.42}$$

$$u^+ = \frac{u}{u_\tau} \qquad y^+ = \frac{u_\tau y}{\nu} \tag{3.43}$$

$$u^+ = y^+ \tag{3.44}$$

If y^+ equals the range $5 - 30$, turbulent stresses are no more negligible, but they become comparable to viscous stresses. The velocity distribution becomes very difficult to compute, since this layer is characterized by unsteady vortices. The so-called *buffer layer* is then treated through both theoretical and empirical approaches, which basically interpolate the formulations achieved for the inner and outer regions and adjust the results by means of experimental coefficients. To give an example, one of the most used formulations is the implicit one by Spalding [27]. B is a fixed value, k is the so-called *Von Karman constant*.

$$y^+ = u^+ + e^{-kB}\left[e^{ku^+} - 1 - ku^+ - \frac{(ku^+)^2}{2} - \frac{(ku^+)^3}{6}\right] \tag{3.45}$$

$$B = 5.5 \qquad k = 0.4 \tag{3.46}$$

In the end, the most *external* region of the boundary layer is characterized by opposite features with respect to the *inner* one, i.e. turbulent effects prevail. The values for y^+ are typically 35 to 50, from which it can be inferred that the turbulent region is the most extended. As it might be expected, the second term in equation 3.37 should be considered as the starting point for modeling.

$$\tau = -\rho u'_x u'_y = \tag{3.47}$$

$$= -u'_x u'_y \tag{3.48}$$

The Boussinesq assumption is adopted (3.18, 3.68), alongside with relations 3.36. In particular, being $u_x \gg u_y$, it identifies with the overall velocity u.

$$\frac{\tau}{\rho} = -\varepsilon\left(\frac{\partial u_x}{\partial y} + \frac{\partial u_y}{\partial x}\right) = \tag{3.49}$$

$$= -\varepsilon\left(\frac{\partial u_x}{\partial y}\right) = \tag{3.50}$$

$$= -\varepsilon\left(\frac{\partial u}{\partial y}\right) \tag{3.51}$$

At this point, the equation can be integrated only if an opportune closure model is adopted. For instance, formulation 3.52 was provided by Prandlt:

$$\varepsilon = l^2\left(\frac{\partial u}{\partial y}\right) \tag{3.52}$$

$$l^2 = (ky)^2 \qquad k = 0.40 \div 0.41 \tag{3.53}$$

The equation becomes:

$$u_\tau^2 = (ky)^2\left(\frac{\partial u}{\partial y}\right)^2 \tag{3.54}$$

$$u_\tau = (ky)\left(\frac{\partial u}{\partial y}\right) \tag{3.55}$$

$$d\left(\frac{u}{u_\tau}\right) = \frac{1}{k}\frac{d\frac{u_\tau y}{\nu}}{\frac{u_\tau y}{\nu}} \tag{3.56}$$

$$u^+ = \frac{1}{k}\ln(y^+) + B \tag{3.57}$$

This correlation accounts for the name given to this sublayer, which indeed is *log-law region*. The value of constant B needs to be computed as a function of the flow velocities at both the extreme boundaries of this sublayer, i.e. velocity is required to be known at both the interfaces with the buffer sublayer and the outside of the overall boundary layer. Since this information is often not available in common applications, velocities are just estimated through interpolation functions applied to different spots of the fluid domains, and B is computed consequently. Nikuradse provided an estimate of 5.5 for it, while eventually Coles and Hirst corrected this value to 5 [3] [4].

Figure 3.5 gives an overview on how stresses within the boundary layer are modeled through analytical functions. The actual trend, provided by

experimental tests, is given by the green line. It can be noticed that the two $u^+ - y^+$ correlations only apply to the limited y^+ range for which they have been developed. The Spalding formulation (or similar) for the intermediate region is not represented, but it simply guarantees continuity between the two end regions.

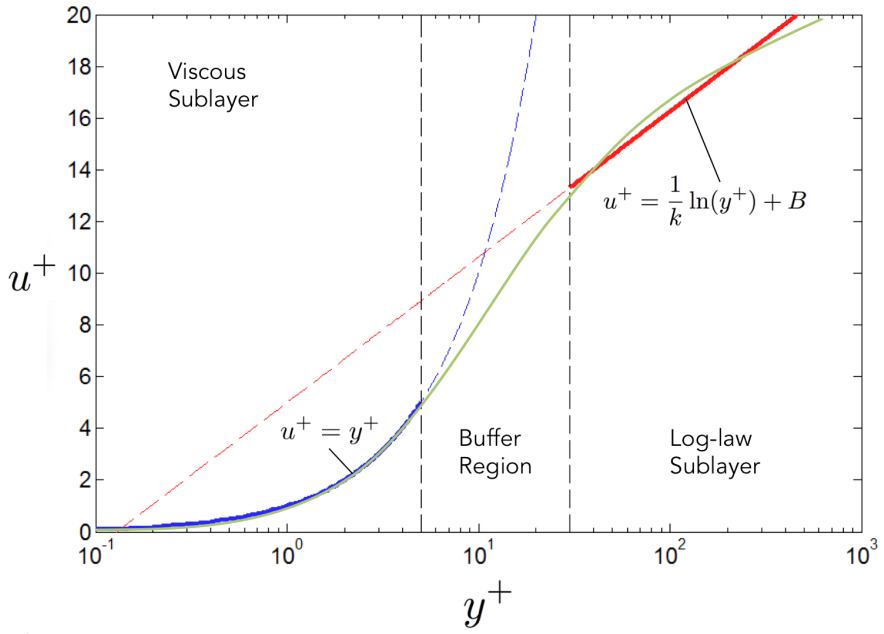

Figure 3.5: Wall Functions

Back to the purpose of this discussion, it will be now briefly addressed how practice comes from theory in two-equation models. The key point is that the boundary layer differs from the outer region due to its higher gradients in velocity and other quantities. On the one hand, this implies that correct meshing is mandatory to achieve satisfactory results. For instance, a good cell refinement is often required to capture the marked variation in aerodynamic quantities. On the other hand, since the fluid behaves in the near-wall layer very differently from elsewhere, the equations describing this behavior require different boundary conditions. Nevertheless, their definition is not physically univocal, thus a variety of near-wall treatments have actually been implemented.

The broader distinction is between *low-Reynolds* and *high-Reynolds* near-wall treatments (respectively LRN and HRN), as shown by figure 3.6. The first approach implies integrating the equations up to inner sublayer. Indeed, a strong refinement is required in the near-wall zone, which means that the

y^+ corresponding to the wall-adjoining cells should be at least smaller than 1. On contrary, the second approach models the overall boundary layer as if it was described by the log-law everywhere. Thus, wall-adjoining cells are larger, since their centroids are assumed to be in the log-law region. Accuracy is somehow less regarded, but convergency and stability do improve.

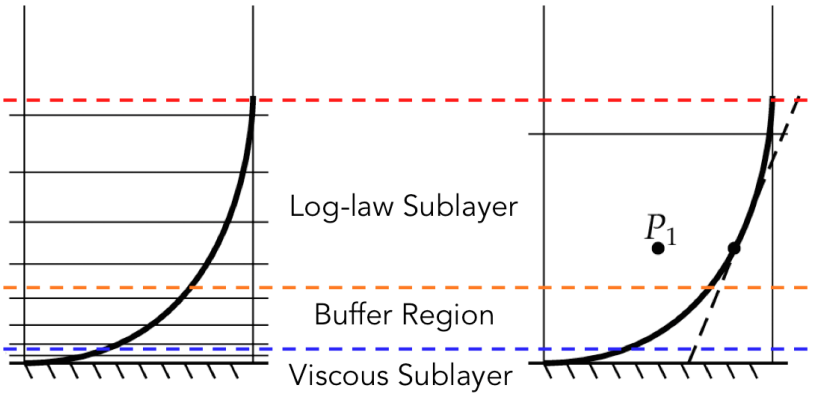

Figure 3.6: Low Reynolds vs. High Reynolds Near-wall treatments

It is important to notice that the centroids of the near-wall cells must fall on either the viscous sublayer or the log-law region. The buffer region, instead, is never taken into account, since no modeling for the boundary conditions is available for that region. Indeed, neither the stresses have been rigorously determined yet. At the most, a discrete switch from one approach to the other can be an option.

In finite volume methods' applications, wall functions can be implemented in two ways. The first solution consists in correcting the equations. Specifically, this is achieved by adding a *source term* to the momentum equation, which accounts for the difference in shear stresses between the boundary layer and the outer domain. The second solution, instead, consists in modifying the values of turbulent viscosity referred to the near-wall cells only. The main difference is that this latter does not aim at reproducing the velocity gradient into the equations, but simply gives the correct value of the shear stress as an overall final result. This is typically the preferred option in two-equation models. For instance, in $k-\omega$ models, if the new value for turbulent viscosity is defined, the shear stress τ can be computed and so can the friction velocity u_τ. The last step is the computation of near-wall k and ω, here denoted as k_w and ω_w. Specifically, k_w results from the zero-gradient condition on velocity (3.58) and ω_w is eventually computed as a function of k_w itself (3.59).

$$\frac{\partial k}{\partial u} = 0 \quad \rightarrow \quad k_w \tag{3.58}$$

$$\omega_w = \frac{\sqrt{k_w}}{C_\mu^{1/4} k y_w} \tag{3.59}$$

3.2.2 LES/ILES Models

A comparison among the diverse models definitively helps introduce Large Eddies Simulation models, since they place in-between RANS and DNS models, from both the points of view of accuracy and computational cost. Indeed, as discussed in the previous chapters, on the one hand Direct Numerical Simulations aim at indiscriminately solve all the scales of turbulence, but for this reason they often result in being unreasonably expensive and unworkable for common applications. On the other hand, Reynolds Averaged Navier-Stokes models focus on the mean motion only, which basically means that no scales are actually solved, but the overall motion is solved as a function of a fictitious mean scale. It stands to reason that, for specific cases, they might exhibit opposite weaknesses to DNS, such as scarce accuracy.

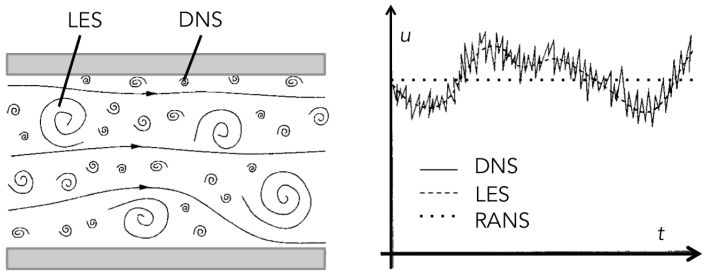

Figure 3.7: Comparison between DNS, LES and RANS models

Thus, LES models distinguish from both, as they somehow *select* the eddy scales to be solved and model the remaining ones. Therefore, they perform better than RANS in terms of the number of data provided about the flow, but of course they turn out to be more expensive. This is the reason why it is advisable to use LES only in case RANS were not performant enough for investigation purposes. Indeed, the real goal in every simulation is to collect the necessary information with the minimum computational waste: any extra datum does represent an extra cost [9]. Examples of cases that would require LES typically involve complex geometries and/or complex flow regimes: for instance, cases with significant changes in the design or very high Reynolds numbers.

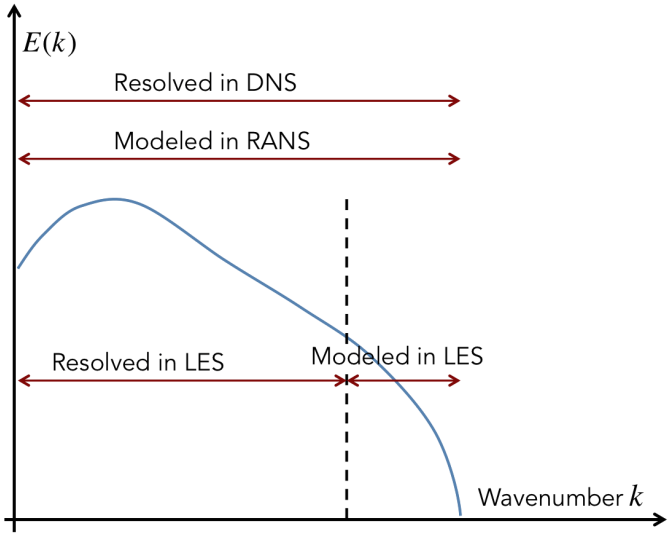

Figure 3.8: Kinetic Energy Spectrum of a Turbulent Flow as a Function of the wavelength k (logarithmic-scale plot).

There are substantial differences between small and large scales of vortices. Broadly, large scales are more dependent on the geometry and the aerodynamics of the overall case analyzed, while small scales are somehow more *universal* [17]. For instance, these latters are characterized by a more *stable* turbulence, resulting in isotropy and other common features. Moreover, large vortices correspond to a higher energy content and are responsible for transporting the conserved quantities, while small scales dissipate, without contributing to transport. For all these reasons, it makes sense to solve large scales and model small eddies.

In order to select the resolvable scales of turbulence, it is important to opportunely filter the overall velocity field. Expression 3.60 provides the new decomposition for velocity:

$$u_i = \bar{u}_i + u_i' \tag{3.60}$$

u_i is the overall velocity field, $\bar{u}_i$ includes the resolvable scales, and u_i' represents the smaller length-scales that cannot be adequately resolved on a computational mesh. The mathematical filtering tool can be a simple local average of the velocity field, as provided by formula 3.61. The result is intuitively shown by figure 3.7.

$$\bar{u}_i(\vec{\boldsymbol{x}}) = \int G(\vec{\boldsymbol{x}} - \vec{\boldsymbol{\xi}}) u_i(\vec{\boldsymbol{\xi}}) d\vec{\boldsymbol{\xi}} \tag{3.61}$$

$G(\overrightarrow{\boldsymbol{x}} - \overrightarrow{\boldsymbol{\xi}})$ represents the *filter kernel* and can be any expression providing a selection for large enough scales. For instance, it can be a *box* filter, a Gaussian or a cut-off filter based on Fourier transform. The same passages just explained for velocity also hold for pressure. It will now be shown how this filtering procedure applies to the Navier-Stokes equations. Actually, only the momentum equation (3.62) will be taken into account. Indeed, since the continuity equation is linear, filtering does not affect it (3.63).

$$\frac{\partial \rho u_i}{\partial t} + \frac{\partial \rho u_i u_j}{\partial x_j} = -\frac{\partial p}{\partial x_i} + \frac{\partial}{\partial x_i}\left(\mu \frac{\partial u_i}{\partial x_j}\right) \tag{3.62}$$

$$\frac{\partial \rho u_i}{\partial x_i} = 0 \tag{3.63}$$

The result of filtering equation 3.62 is given by equation 3.64:

$$\frac{\partial \rho \bar{u}_i}{\partial t} + \frac{\partial \rho \overline{u_i u_j}}{\partial x_j} = -\frac{\partial \bar{p}}{\partial x_i} + \frac{\partial}{\partial x_i}\left(\mu \frac{\partial \bar{u}_i}{\partial x_j}\right) \tag{3.64}$$

Since term $\overline{u_i u_j}$ is difficult to compute, equation 3.64 is re-written as in 3.65, where this term is replaced by $\bar{u}_i \bar{u}_j$. Actually, $\overline{u_i u_j} \neq \bar{u}_i \bar{u}_j$, thus a new term also shows up on the right-hand side of the equation, which accounts for this difference. Its definition is provided by equation 3.66. The reason for such a manipulation is that this term is eventually modeled in such a way that the computation of $\overline{u_i u_j}$ can be avoided.

$$\frac{\partial \rho \bar{u}_i}{\partial t} + \frac{\partial \rho \bar{u}_i \bar{u}_j}{\partial x_j} = -\frac{\partial \bar{p}}{\partial x_i} + \frac{\partial}{\partial x_i}\left(\mu \frac{\partial \bar{u}_i}{\partial x_j}\right) + \frac{\partial \tau_{ij}^S}{\partial x_j} \tag{3.65}$$

$$\tau_{ij}^S = -\rho\left(\overline{u_i u_j} - \bar{u}_i \bar{u}_j\right) \tag{3.66}$$

τ_{ij}^S is called *subgrid-scale Reynolds stress*. However, on the one hand, the name *stress* only stems from its role into the equation, but cannot be considered as an actual physical stress to be measured. On the other hand, also the name *subgrid* needs to be specified, as τ_{ij}^S represents the large-scale momentum flux that arises from the small-scale motion.

As a consequence, the models used to approximate τ_{ij}^S are called *subgrid-scale models* (SGS) or *subfilter-scale models*. An example is given by the Smagorinsky model (1963), in which the Boussinesq hypothesis is used. It basically assumes that the principal effects of τ_{ij}^S are increased transport and dissipation, which in turn depend on viscosity. With some manipulation from the equality between power and dissipation of the subgrid-scale turbulent kinetic energy, the model takes the formulation provided by Eq. (3.67). Actually, this is only one of the possible ways to deduce it, but other procedures are also possible (heuristic methods, turbulence theories and so on).

$$\tau_{ij}^S - \frac{1}{3}\tau_{kk}^S \delta_{ij} = \mu_T \left(\frac{\partial \bar{u}_i}{\partial x_j} + \frac{\partial \bar{u}_j}{\partial x_i} \right) = 2\mu_T \bar{S}_{ij} \tag{3.67}$$

$$\bar{S}_{ij} = \frac{1}{2} \left(\frac{\partial \bar{u}_i}{\partial x_j} + \frac{\partial \bar{u}_j}{\partial x_i} \right) \tag{3.68}$$

The filtered Navier-Stokes equation using this model τ_{ij}^S is given by Eq. (3.69):

$$\frac{\partial \rho \bar{u}_i}{\partial t} + \frac{\partial \rho \bar{u}_i \bar{u}_j}{\partial x_j} = -\frac{\partial \bar{p}}{\partial x_i} + \frac{\partial}{\partial x_i} \left((\mu + \mu_T) \frac{\partial \bar{u}_i}{\partial x_j} \right) \tag{3.69}$$

The subgrid-scale eddy viscosity μ_T is derived by dimensional arguments. Its formulation is shown by Eq. (3.70):

$$\mu_T = C_s^2 \rho \bar{\Delta} |\bar{S}| \tag{3.70}$$

$$|\bar{S}| = |\bar{S}_{ij} \bar{S}_{ij}|^{1/2} \tag{3.71}$$

C_s is a model parameter to be defined. It often equals 0.2 for isotropic turbulence, but depends on a number of factors, such as Re. $\bar{\Delta}$, instead, is the filter length scale (i.e. the minimum resolvable scale) and is computed as the cube root of the cell volume V to which it applies.

$$\bar{\Delta} = V^{1/3} \tag{3.72}$$

Filter width and mesh size need to be consistent. Precisely, the chosen $\bar{\Delta}$ must satisfy the inequality $\bar{\Delta} > h$, where h is the grid size.

Back to the main discussion, it can then be stated that large-eddy simulations do represent a successful method to be used especially when more accessible alternative approaches (such as RANS) fail. However, a physical modeling such as the one just discussed in this chapter might be very difficult to deal with, especially for two reasons. The first one is that the dynamic mechanisms of the physical phenomenon might be unknown or too complex to be modeled explicitly and exactly. For instance, this occurs when there is a strong interaction between complex thermodynamic and hydrodynamic mechanisms (combustion or shock/turbulence interaction). The second reason is that explicit modeling often does not allow realizing some constraints on the quantities under investigation (e.g. on the temperature or the molar concentration of pollutants).

In those situations, the solution is represented by the so-called *implicit* large-eddy simulations (ILES). They all base on the hypothesis that the

action of the sub grid scales on the resolved scales is equivalent to a strictly dissipative action. As a consequence, no subgrid-scale model is added to the discretized Navier-Stokes equations and a dissipation term is introduced either in the framework of upwind schemes for the convection (the most used approach) or explicit artificial dissipation term, or by the use of implicit or explicit frequency low-pass filters. The degree and order of the diffusive term introduced both depend on the chosen scheme. Typically, a second and/or fourth order is used, which makes the dissipation induced very close to that implied by physical subgrid models. The difference, however, is that an implicit viscosity replaces an explicit model inferred from inadequate physical considerations (for the complex cases listed above) with no worse impact on the quality of the results and, above all, the implicit version of LES allows using more robust numerical methods. This is the key point and also the reason why high-resolution simulations of flows today are more and more considered [26] [1].

3.2.3 DLRM

The model used for this thesis work is a scale-adaptive hybrid RANS-LES model, namely *Dynamic Length Scale Resolution Model* [23], which will be soon introduced.

Let us consider figure 3.8 first, from the previous chapter. In LES models, the threshold between modeled and resolved scales theoretically stems from the condition of equality between power production P and dissipation ϵ, i.e. dissipative scales are the only ones to be modeled and not resolved. As previously discussed, by resolving the largest scales instead of modeling the whole energy spectrum, accuracy in results definitely improves. Specifically, the model is also able to capture isolated and random flow unsteadiness. This is, indeed, one of the achievements over RANS models, to which flow isolated events are invisible. In fact, on contrary, in RANS models, turbulent length and time scales are inferred from simple dimensional analysis and are often overestimated, to the extent that flow unsteady local behaviors appear to be flattened. Moreover, RANS models are very dependent on initial and boundary conditions, so that results are perfectly repeatable if these conditions do not change. This aspect is another reason for their limitations in the fluid description.

Nevertheless, LES models' accuracy is counterbalanced by their expensiveness, which is sometimes comparable to DNS, especially for what concerns near-wall regions. Approximations such as the already discussed near-wall treatments can be adopted to reduce the computational cost, but for complex flows with high Reynolds numbers good accuracy can only be achieved through a good near-wall mesh refinement.

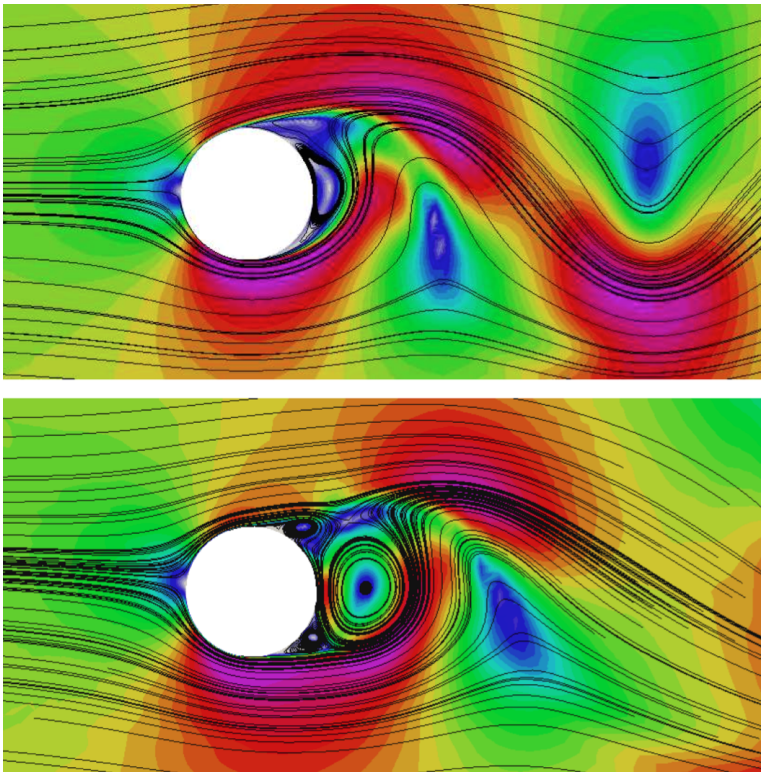

Figure 3.9: Comparison RANS vs. LES

These issues have led to the implementation of hybrid models, which aim at matching the best of the two worlds, i.e. at combining the efficiency and cheapness of RANS models with the accuracy from LES. The basic idea is to locally switch from one to the other according to some criteria. There is no unique optimum compromise, and the model performance mostly depends on the choice of the discriminating factor regulating the switch-mode of the hybrid model itself. Indeed, for instance, some models are based on the distance of the domain cells from the wall, but diverse solutions do exist as well.

The peculiarity of DLRM is that the change is based on the local turbulence length scale. Precisely, each turbulence length scale to be analyzed is firstly compared to the minimum resolvable scale according to LES. If this lenght-scale falls on the resolvable range of the energy spectrum allowed by the LES model, this latter is chosen. Otherwise the length-scale is modeled according to a standard $k-\omega$ SST model [21].

An insight into the logic behind this model is now provided, with reference to [23]. The locally minimum resolvable scale ℓ_t, which regulates the

switch between RANS and LES, is the result of a comparison between the local integral length scale L_t according to RANS and the local resolvable length scale Δ_f allowed by LES:

$$\ell_t = \min\left(L_t, \Delta_f\right) \tag{3.73}$$

L_t can be estimated directly from the values of turbulent kinetic energy k and dissipation ω for the standard Menter's $k-\omega$ SST model:

$$L_t \sim \frac{k^{1/2}}{\omega} \tag{3.74}$$

The estimate of Δ_f, instead, is given by:

$$\Delta_f = \max\left(\alpha|U|\delta t, \Delta_{eq}\right) \tag{3.75}$$

Both the two terms into brackets can be interpreted as estimates of the available LES filter width, and clearly the largest one is chosen for the model purposes. However, they differ from each other since their definitions stem from the evaluation of the constraints respectively imposed by time and space discretization, as will be soon explained. Indeed, Eq. (3.75) re-establishes their correlation, accounting for the fact that the temporal scales of the vortices and the spatial resolution of the grid are not independent from each other. This feature of the filter operation is of utmost importance, since less likely sudden changes in cell sizes or flow condition will go uncaught.

Let us focus on term $\alpha|U|\delta t$ first. The starting point is the assumption that the LES filter width $\Delta_{f,i}$ of cell i is proportional to the maximum distance covered by the corresponding fluid particle in a time step:

$$\Delta_{f,i} \propto U_i \delta t \tag{3.76}$$

It is opportune to set the condition given by Eq. (3.77) to take into account the need for a limited number of cells to actually resolve a turbulent structure (see also [14]).

$$\Delta_{f,i} \geq U_i \delta t \tag{3.77}$$

An equivalent formulation is then given by Eq. (3.78):

$$\Delta_{f,i} = \alpha U_i \delta t \qquad \alpha \geq 1 \tag{3.78}$$

where α is the proportionality constant. The goal now is to find a proper definition for this constant. To this purpose, let us introduce the Courant-Friedrichs-Lewy relation first. Given the discretized domain, it directly conditions the choice of the time-step, as shown by Eq. (3.79):

$$\delta t \leq \frac{CFL_{max}}{(U_i/\delta x_i)_{max}} \tag{3.79}$$

Indeed, in this formula, CFL_{max} is chosen on the basis of the numerical method adopted and the level of unsteadiness of the flow, while $(U/\delta x)_{max}$ represents the ratio of velocity to cell size belonging to the cell(s) for which this ratio is the largest of the whole mesh. Of course, once the δt is selected for the case study ($\delta t = \delta\bar{t}$), then the reverse formula gives the exact definition of CFL_{max} for the case analyzed.

$$CFL_{max} = \delta\bar{t}\left(\frac{U_i}{\delta x_i}\right)_{max} \tag{3.80}$$

Similarly to Eq. (3.80), a CFL_i for any cell i can be defined, as function of the chosen $\delta\bar{t}$:

$$CFL_i = \delta\bar{t}\left(\frac{U_i}{\delta x_i}\right) \tag{3.81}$$

and it clearly must hold:

$$CFL_i \leq CFL_{max} \tag{3.82}$$

In order to estimate α, it is also assumed that turbulence is normally generated at those cells with the highest CFL_i values. It must be said that this second assumption is true in most cases, but it is not general. Anyway, its limitations and implications will be discussed at a later time. For the moment, let us rewrite the definition of $\Delta_{f,i}$ given by Eq. (3.78) as a function of the defined CFL_i, which is possible thanks to Eq. (3.81):

$$\begin{aligned} \Delta_{f,i} &= \alpha U_i \delta t = && (3.83)\\ &= \alpha\frac{U_i\delta t}{\delta x_i}\cdot\delta x_i = && (3.84)\\ &= \alpha CFL_i \delta x_i = && (3.85) \end{aligned}$$

The cells representing the starting point for vortex generation (here, the ones with the highest CFL_i) are normally of superior interest for the analysis purposes. Thus, a LES model would be preferred since it gives more accurate results than RANS. For this reason, it would be very opportune to have the smallest $\Delta_{f,i}$ for these cells. In fact, since it represents the minimum length scale that is resolvable by LES, this choice would imply a more extended range of resolvable scales allowed, and as a consequence a higher possibility that the model switches from RANS to LES. Therefore, the value 1 is chosen for α, as it is the minimum permitted by Eq. (3.79). The result is that, for the cells corresponding to $CFL_i = CFL_{max}$, it holds:

$$\Delta_{f,max} = (\alpha)_{min} CFL_i \delta x_i = \tag{3.86}$$
$$= 1 \cdot CFL_{max} \delta x_i \tag{3.87}$$

To be coherent with this criterion, for which a smaller $\Delta_{f,i}$ should be preferred for a higher CFL_i, the value of $\Delta_{f,i}$ for all the remaining cells is also scaled consistently, i.e. as inversely proportional to their CFL_i numbers compared to CFL_{max}. The conclusion is the definition for α given by Eq. (3.88), which could be also inferred by comparing Eq. (3.87) to Eq. (3.83).

$$\alpha = \frac{CFL_{max}}{CFL_i} \tag{3.88}$$

Thus, for *any* cell, from Eq. (3.83) it holds:

$$\Delta_{f,i} = \alpha CFL_i \delta x_i = \tag{3.89}$$
$$= \frac{CFL_{max}}{CFL_i} \cdot CFL_i \delta x_i = \tag{3.90}$$
$$= CFL_{max} \delta x_i \tag{3.91}$$

Up to now, the procedure for defining α as in Eq. (3.88) has been discussed, but the method should be re-formulated in reverse. To sum up, parameter CFL_{max} is fixed first, since it depends on the numerical method and the level of turbulence of the case under investigation. Eventually, this parameter allows defining the time-step $\delta t = \delta \bar{t}$ each time. By defining $\Delta_{f,i}$ for cell i as proportional to $Ui\delta\bar{t}$ up to a constant $\alpha \geq 1$, the method would be over, if the value of α was just prescribed for the entire simulation, according to some criteria. Indeed, in literature diverse estimates for α are available, such as the value of 3 suggested by [13], which results from experimental tests.

However, the peculiarity of this method is that, thanks to the assumptions made, α is instead dynamically defined at each step and for each cell according Eq. (3.88). The dependence of α on both time and space is definitively a plus for the method, since it allows for a more correct estimation of the minimum integral length scale that can be locally captured by the model. This is basically one of the main improvements this method brings up if compared to previous formulations.

At this point, Eq.(3.91) should be further clarified. If at any step CFL_{max} is prescribed *a priori*, as already stated, then this expression basically relates $\Delta_{f,i}$ to the cell size δx_i only. In other words, the model will unlikely switch to LES if the mesh is too coarse. This definitively makes sense, since typically the mesh is refined at the zones of interest, and for

those regions the model guarantees that a more accurate method is used.

However, there might be some situation in which this does not hold. Let us consider a meshed flow domain (for instance a flow in a duct) and let us consider that there can exist two cells stream wise with same CFL equaling CFL_{max}, namely cell A (upstream) and B (downstream). Cell A is of intermediate size, but the velocity is high; at cell B the velocity reduces but the mesh refinement is higher. Therefore, since for this case the model only depends on the difference in δx_i, it might happen that a RANS model is used for cell A, while a LES model is applied to cell B. The problem is that, if hypothetically turbulence generates in A and propagates to B, the adoption of LES at B loses importance if only the mean turbulent motion has been considered in A. In other words, part of the useful information has been lost at A and using LES at B would only imply a computational waste.

This is the only inconsistency of DLRM and, specifically, it is an implication of the fact that the assumption that turbulence generates at high-CFL cells might not be verified. Indeed, CFL_{max} does not take the velocity only into account, but the ratio of the velocity to the cell dimension, while turbulence generation should only depend on the physics of the problem and not on the way the mesh is produced. It is the mesh, if anything, that should be realized accordingly with the physical problem, i.e. a smart solution would be to try to foresee where to expect turbulence generation and refine the mesh in those regions.

Nevertheless, it is also true that the troubling situation just described rarely happens. For instance, let us consider a fluid stream flowing into a duct with a sudden section enlargement. It is very likely that the mesh is more refined at the section change, where also the velocity is higher, and becomes coarser downstream, where the fluid decelerates.

Back to Eq. (3.75), let us now focus on the derivation of Δ_{eq}, which represents an equivalent LES filter size. Parameter LSR, extensively *lenght-scale resolution*, is first defined:

$$LSR = \frac{\Delta}{\ell_{di}} \tag{3.92}$$

The numerator is the length scale cut-off for the available LES model, thus it represents its actual filter width. The denominator, instead, is the value of the length scale corresponding to the lower limit of the vortex inertial subrange:

$$\ell_{di} \approx 60\eta \tag{3.93}$$

where η is the Kolmogorov scale:

$$\eta = \nu^{3/4}\epsilon^{-1/4} \tag{3.94}$$

If LSR equals 1 (the best case), the filter is able to resolve all the large scales, up to the dissipative subrange. However, in order to have a reasonable resolution in space and time at affordable cost, also a $LSR > 1$ can be accepted, within a limited specified range. Precisely, it has been observed that, for common engineering applications, the filter still works, even if less effectively, if $LSR \leq LSR_{max} = 5 \div 7$. If LSR, instead, exceeds this threshold, the ILES model loses its underlying hypotheses and, as a consequence, its validity. In fact, the assumptions that the modeled scales are isotrope and that power production equals dissipation are no more verified. When this occurs, the DLRM opts for a RANS model by default.

Following on from all these considerations, the equivalent LES filter size to be adopted in Eq. (3.75) is then:

$$\Delta_{eq} = LSR_{max} \cdot \ell_{di} \tag{3.95}$$

Back to Eq. (3.73), let us assume that the locally minimum resolvable scale ℓ_t has now been selected. This value enters the formulation of the filter function g:

$$g \equiv \left(\frac{\ell_t}{L_t}\right)^{2/3} \tag{3.96}$$

which, in turn, allows computing the –let us define it – *filtered* turbulent viscosity $\hat{\mu}_T$:

$$\hat{\mu_T} = g^2 \rho \frac{k}{\omega} \tag{3.97}$$

$\hat{\mu}_T$ is the key parameter of the DLRM model, since it exactly represent the discriminating factor that allows switching from one model to the other.

Specifically, if ℓ_t equals L_t, then $g^2 = 1$, thus μ_T is led back to its original (non-filtered) definition. In other words, in these regions the filter is not active and a RANS model is adopted.

$$\hat{\mu_T} = \rho \frac{k}{\omega} = \mu_{T,RANS} \qquad g^2 = 1 \tag{3.98}$$

On contrary, wherever l_t equals Δ_f, the original value of turbulent viscosity is reduced by a factor $g^2 < 1$. The result is a value of $\hat{\mu}_T$ as if it was given by the numerical dissipation, thus an ILES model is implemented.

$$\hat{\mu_T} = \mu_{T,ILES} < \mu_{T,RANS} \qquad g^2 < 1 \tag{3.99}$$

From a broader point of view, by comparing the local resolvable scales to the problem turbulence length scales, the model does nothing but evaluating if the grid resolution is high enough to allow the usage of a LES model. Any time the mesh is considered to be too coarse (compared to the turbulence problem investigated), a RANS model is adopted.

To understand the way the filter g^2 is derived and especially why it is a *squared* function, let us start from the consideration that the modeled length scale ℓ_T can also be defined in terms of the filtered (non-resolved) variables:

$$\ell_t \sim \frac{\hat{k}^{1/2}}{\hat{\omega}} \tag{3.100}$$

This change in perspective allows relating the filtered specific dissipation $\hat{\omega}$ to the filtered dissipation rate $\hat{\epsilon}$ similarly to Eq. (3.28):

$$\hat{\omega} = \frac{\hat{\epsilon}}{C_\mu \hat{k}} \tag{3.101}$$

The dissipation rate is resolved by DNS, since no cheaper alternative is available:

$$\hat{\epsilon} = \epsilon \tag{3.102}$$

Therefore, from Eqs. (3.28), (3.101) and (3.102):

$$\hat{\omega} = \frac{\omega k}{\hat{k}} \tag{3.103}$$

and from Eqs. (3.74), (3.100) and (3.101) an expression for the filtered turbulent kinetic energy can be found:

$$\hat{k} = g(\ell_t, L_t)k \tag{3.104}$$

where the equality holds in turn due to the equality of the proportionality constants from Eqs. (3.74) and (3.100). It is now explained how the filter function g is derived up to its formulation expressed by Eq. (3.96). In this, ℓ_t is computed according to Eq. (3.73) and L_t is calculated as:

$$L_t \simeq \frac{k^{1/2}}{C_\mu \omega} \tag{3.105}$$

In regions where turbulence cannot be resolved, i.e. where $L_t < \Delta_f$ in Eq. (3.74), the filter function g is set equal to 1 in order to have $\hat{k} = k$ in Eq. (3.104). However, there is no need to compute the filtered turbulent variables explicitly. A filtered turbulent viscosity $\hat{\mu}_T$ can be defined directly from the non-resolvable turbulent length and time scales:

$$\hat{\mu}_T \sim \frac{\ell_t^2}{t_t} \tag{3.106}$$

$$t_t \sim \frac{1}{\hat{\omega}} \tag{3.107}$$

Here the time scale has been computed directly in terms of the filtered (non-resolved) variables, in conformity with the derivation of the length scale ℓ_t in Eq. (3.100). By putting together Eqs. (3.100), (3.103), (3.104) and (3.107), it is straightforwardly proved why the model ends up with the formulation given by Eq. (3.97), which includes a squared g function.

To recap, no matter the two-equation turbulent model used, in any case the derivation of g will lead to formulation given by Eq. (3.96) [14]. The novelty, however, is that g has been applied to k and not directly to μ_T, as shown by Eq. (3.104), which accounts for the final result given by Eq. (3.97). The peculiarity is that this formulation includes g^2 instead of g. Thus, the goal now is to explain the implications of this choice to understand its reasons.

Let us consider both the two options of applying g or g^2 to μ_T in Eq. (3.97) and let us compare them. The filter function is first required to equal 1 as Δ_f equals the integral length of the modeled scales L_t, to reinstate the original RANS formulation given by Eq. (3.98). Both the two filter functions fit this requirement, thus the choice of the most suitable option does not depend on this point.

$$lim_{\Delta_f \to L_t} \;\; g = 1 \tag{3.108}$$

$$lim_{\Delta_f \to L_t} \;\; g^2 = 1 \tag{3.109}$$

The second requirement is that the filter function should tend to zero as the filter width Δ_f tends to zero. Again, both g and g^2 fulfill this condition, which represents an opposite situation to the one addressed before. Indeed, it states that if μ_T tended to zero, a DNS would be adopted. Actually, this situation never happens and is only taken into account theoretically.

$$lim_{\Delta_f \to 0} \;\; g = 0 \tag{3.110}$$

$$lim_{\Delta_f \to 0} \;\; g^2 = 0 \tag{3.111}$$

Therefore, up to now both the two filter functions would be suitable. However, as the last requisite, it turns out that also *how* the filter functions approaches the zero value is important. Thus, what makes the difference

is actually the limit of the first derivative of the filter function (and consequently the second) as Δ_f tends to zero.

$$lim_{\Delta_f \to 0} \left(\frac{\partial g}{\partial \Delta_f} \right) = \infty \tag{3.112}$$

$$lim_{\Delta_f \to 0} \left(\frac{\partial (g^2)}{\partial \Delta_f} \right) = 0 \tag{3.113}$$

The results show that the g function would approach the zero value with a vertical tangent line, while g^2 goes to zero with an horizontal tangent line. If the limit for g^2 is computed on its second derivative, a positive value is obtained as a result:

$$lim_{\Delta_f \to 0} \left(\frac{\partial^2 (g^2)}{\partial \Delta_f^2} \right) > 0 \tag{3.114}$$

This guarantees that for small variations of Δ_f about the zero value, the filter function g^2 will not undergo sudden rises. On contrary, the filter function g would not guarantee a smooth proportionality between Δ_f and the filter function itself. For this reason, g^2 is selected, which indeed implies that g is applied to k and not directly to μ_T. This setting is very important, since it allows for a higher possibility that, for any given length scale, the model prefers a LES resolution to RANS.

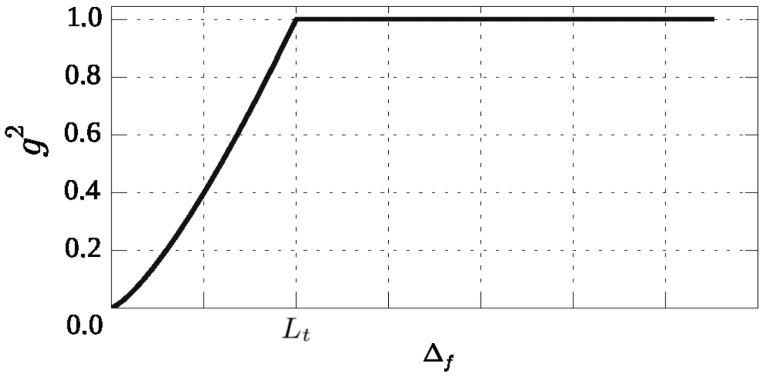

Figure 3.10: Filter Function $g^2(\Delta_f)$

The trend of g^2 as a function of Δ_f is shown by Fig. 3.10. This plot clearly shows how g^2 is clipped to 1 as Δ_f equals the integral length of the modeled scales L_t, as well as how it *smoothly* tends to zero as the grid size tends to the fine grid limit.

Chapter 4

Case Study

This chapter will give an overview about the case study investigated. The wind turbine on hand will be described in both its structural features and its aerodynamical properties. The final goal of this thesis is the comparison of the numerical results from simulations with the already available experimental results provided by V. Dossena *et al.* [7]. Thus, a brief overview of the reference paper will be provided as well. Specifically, the experiments have been performed on diverse machine and flow conditions, but one case has been selected to be tested numerically. The reasons for this choice will also be discussed, and the only information that aligns with the purposes of this thesis will be highlighted from the reference [7].

4.1 Machine Description

This thesis focuses on a H-type vertical-axis wind turbine as case study. The machine geometry is soon provided by Fig. (4.1). The rotor is composed by three untwisted blades, connected to the vertical mast by means of two horizontal supports. It has a swept area of approximately 1.5 m^2 (DxH, 1.028 m x 1.5 m) and it is equipped with dihedral blades with unstaggered NACA 0021 profiles ($c = 0.086\ m$). The blade detail is provided by Fig. (4.2).

Both the proportion in the machine dimensions and the design of the supports aim at minimizing the overlap between the wakes generated by the blade motion and the overall turbulence. Indeed, as previously discussed, the main obstacles to VAWTs' good performances are their unsteady aerodynamics and time-dependency, which make the interaction between the machine and the fluid very complex to investigate.

For what concerns materials, the blades are made up by a wooden core and a reinforcing cladding of CFRP. The two supports, instead, are made

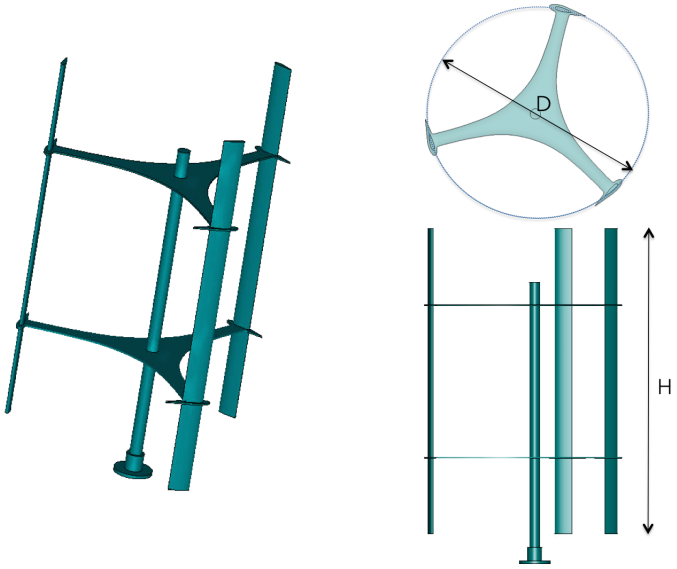

Figure 4.1: Case study geometry

of aluminum, while the vertical mast is made of steel. The rotor prototype has been designed by Tozzi Nord s.r.l., while the test stand and the acquisition system have been realized by the staff from Università di Trento.

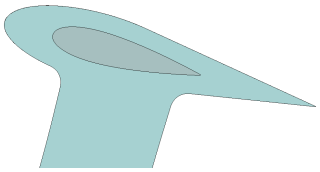

Figure 4.2: Blade Detail

4.2 Brief Overview of the Experimental Tests

Experimental tests were carried out in the wind tunnel facility at Politecnico di Milano. It consists in a two-floor building, each hosting a different section for testing. Precisely, the lower floor is a low-speed test section (14 m width x 3.84 m height) allowing a maximum air velocity of approximately 15 m/s, while the upper floor consists in a high-speed section (4 m x 3.84 m) allowing a maximum velocity of 55 m/s. Wind is generated by 14 fans, grouped into two parallel rows and driven by an inverter-controlled motor each. The overall installed electric capacity is 1.4 MW. Specifically, the

high-speed section has been chosen for tests, which is characterized by a turbulence level lower than 1%.

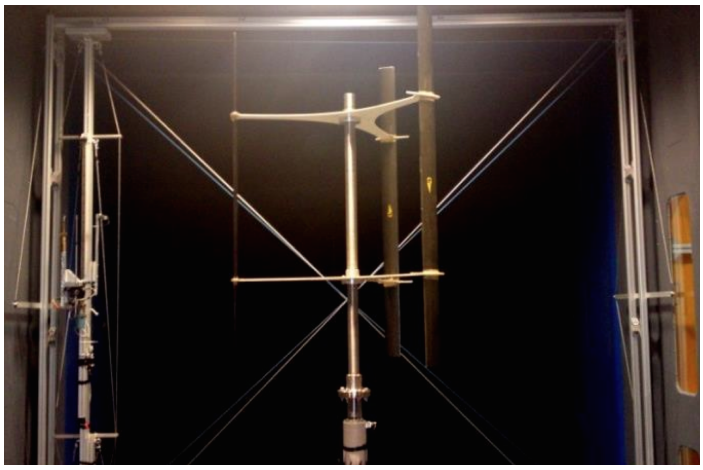

Figure 4.3: Test set-up in the large-scale section of the wind tunnel at Politecnico di Milano

A full-scale model has been tested, thus experiments have been performed in full-similarity conditions. Clearly, this has been possible since the wind turbine under investigation is designed for micro-generation of power.

To the purposes of [7], the machine was tested in both a confined and a non-confined environment. Indeed, one of the goals was to highlight the effect of the wind tunnel blockage on the aerodynamics and performances of the VAWT on hand. Broadly, the fluid flow is always conditioned by the presence of the wind tunnel walls and it is often impossible to reproduce an open-space condition for tests that exactly corresponds to reality. However, if the object is small enough in comparison with the dimensions of the wind tunnel itself, the edge effects might be properly confined far enough from the domain of interest that the results are considered to be accurate.

This requirement was fulfilled by the open-chamber configuration, but the machine was also tested in a close chamber (an opportunely-built removable test room) to compare the results. The final goal was, indeed, to infer a correlation model for the blockage effect from this comparison, to pave the way for other experiments that would not necessarily require a strict proportionality between the model dimensions and the size of wind tunnel section. In fact, the goal was to allow future testing of wind-turbine models with even too big dimensions if compared to the test section and adjust the results by applying some corrective factor.

It must be said that diverse blockage correlation models already existed in literature, but there was no available model for the tested machine design and this is why the experiments on the close chamber were performed.

In particular, its estimate is very difficult and strongly dependent on the specific machine type. The reason is that, when crossing the turbine, the airstream dynamically deforms as a function of both the machine design and the wind conditions. Also, they influence the deflection that the airstream undergoes downstream of the machine (we are dealing with a rotating object), which is especially evident for vertical-axis machines. Thus, every case is different from one another, and the correlations need to be derived each time. Moreover, despite the fully-stationary conditions of the flow that can be set upstream, the complex interaction between wind and turbine also affects the repeatability of the tests and makes the investigation of the blockage due to the wall very challenging.

Nevertheless, this is not the topic of this thesis, but the specification of this point is useful to give an overview about the reference paper and select the information that align with the purposes of this thesis. Precisely, the only results on the open-chamber configuration have been taken into account. After all, the blockage effect is a problem strictly correlated to experimental tests and the issue of edge effects onto the flow stream in numerical simulations is addressed from a completely different perspective, as will be soon explained in the next section.

4.3 General Set-up of the Study Case

The first goal is to reproduce a non-confined environment around the turbine, in order to set the same conditions of the open-chamber configuration from the reference paper. Indeed, this is crucial to allow a correct comparison of the results.

It is clear that, differently from experiments, there are no walls to be taken into account. However, also in numerical set-ups the domain edges do affect the flow stream and, as a consequence, the results of simulations. For instance, one condition might set the velocity of the fluid at the domain boundaries to its far undisturbed value. This definitively makes sense, but it still represents a constraint on the velocity field with its implications. For instance, it evidently prevents the fluid from crossing the boundaries, which can physically happen but is extremely difficult to consider.

There actually exists a solution to these obstacles, which consists in extending the numerical domain far enough from the turbine, in such a way

that its edge effects cannot interfere with the flow behavior in the proximity of the machine and consequently with the turbine behavior. A top view for the numerical domain chosen for the case on hand is shown by Fig. (4.4). As it can be noticed, its extension is significant with respect to the machine size.

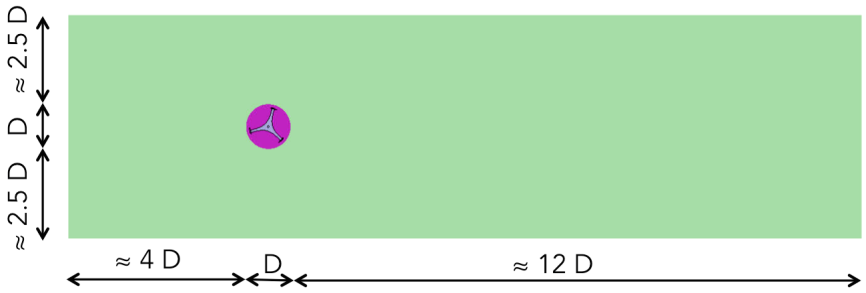

Figure 4.4: Top view of the numerical domain extension

Fig. (4.5), instead, shows the results of the velocity field from a preliminary 2D simulation that has been performed on the turbine under investigation, by using an unsteady RANS model (URANS) and with the same turbine and fluid settings used for the 3D case that is the topic of this thesis.

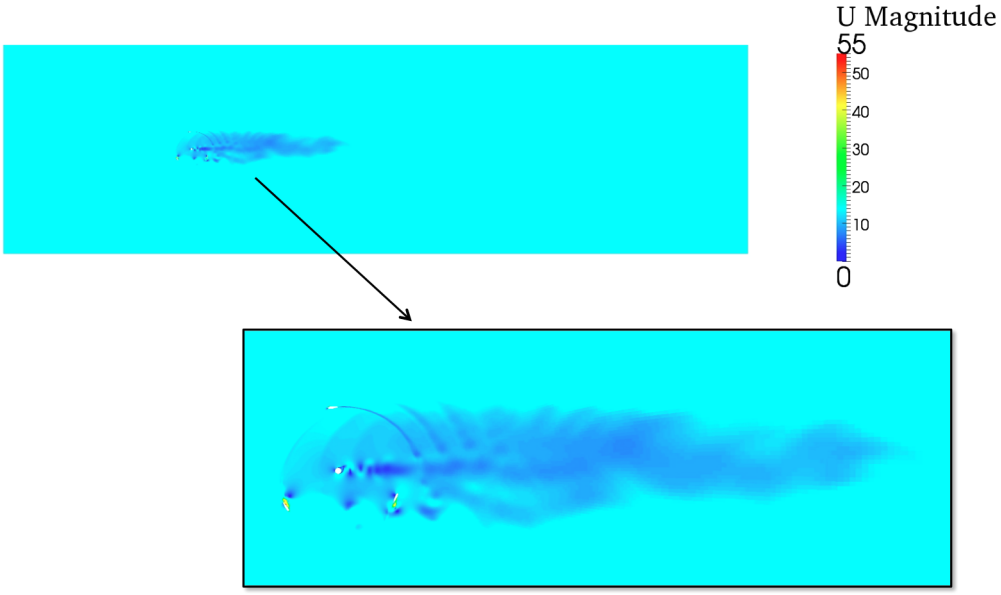

Figure 4.5: Velocity field at $t = 0.5$ s

The simulation was carried out only for a few time-steps ($t = 0.5$ s is the time-step shown in the figure), since the goal was to just get a general overview of the fluid behavior to easily set up the 3D simulation in a proper way from the very beginning. Indeed, it is not truly trustworthy from the aerodynamics point of view, since – as stated in Ch. (3.2) – turbulence is strictly a three-dimensional regime of motion. Especially if the geometry is complex, only a 3D simulation can provide a reliable description of the fluid flow. However, it has been useful to get some important hints for the 3D case.

First of all, it shows that there exists an undisturbed region outside the domain portion affected by the interaction with the turbine, i.e. far from the turbine, the velocity equals the magnitude value set upstream. The presence of this region proves that the edge effects have been properly isolated and, consequently, that the chosen domain extension is correct.

Secondly, it shows the extension of the turbine turbulent region and the way the blade wakes interact and overlap (at least, qualitatively). Indeed, this information is particularly useful when realizing the mesh, since it indicates which regions should be refined more than the others and the way the cells should better be oriented. Thus, on the one hand, especially for a very extended domain, it is important to limit a high mesh resolution to a few selected regions and create a coarser mesh elsewhere, since this allows reducing the overall number of cells and consequently the computational cost. In fact, the resulting mesh is always a compromise between the accuracy of the results (given by a higher refinement) and the computational cost involved. On the other hand, if the cells are oriented accordingly to the flow stream (for this case, along a circumference), then the possible numerical issues are more likely to be held back.

So, from the blade detail in Fig. (4.5), it is evident that the wakes arrange according to an annulus around the turbine. Therefore, the mesh should be especially refined along this circumference and, in general, inside the cylinder shown by Fig. (4.6), which is a detail of Fig. (4.4).

The lateral surface of this cylinder is also chosen to be the interface between an *outer* meshed domain, which is still, and an *inner* one, which rotates together with the turbine. This solution for dealing with rotating objects, namely *Arbitrary Mesh Interface*, will be deepened in Ch. (4).

It must be clarified at this point that, in general, a more meticulous procedure would require a *grid independence test*. Especially if a very refined mesh is required for the zones of interest, the dimension of the cells is set to the value for which the accepted error (in simulation results) becomes stable

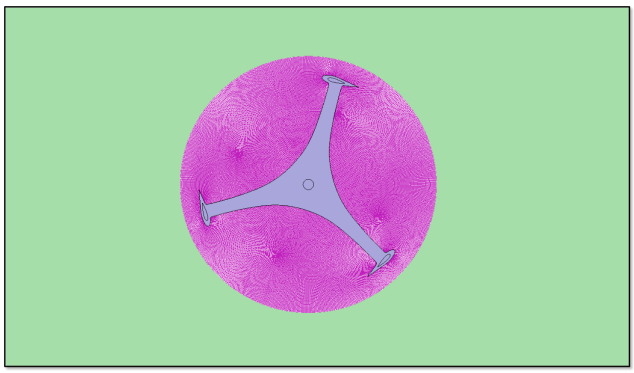

Figure 4.6: Mesh refinement in the near-turbine region

for even more refined meshes. In other words, the cell size is chosen in such a way that a higher refinement would involve a non-significant improvement in the results according to confidence bound set *a priori*.

To achieve this goal, the simulation is therefore repeated more times with the same settings, except for the level of mesh refinement, which is improved at each attempt (for instance, at each step the cell number is doubled). The trend of some aerodynamic quantity (e.g. the coefficient of power) is derived as a function of the mesh refinement and it is then possible to make a prediction of the mesh refinement level that allows the analyzed quantity to converge within the established confidence bound. Thus, this refinement level is selected for the simulation, if its adoption is compatible with the available computer tools.

For the case analyzed in this thesis, the grid independent test is unfortunately not feasible. In fact, as already discussed, this case requires a very extended domain and, of course, a good level of refinement. The result, that will be presented in the next chapter, is ≈ 45 M cells and definitively implies a huge computational cost. Therefore, the reason for which the grid test is not performed is that the repetition of the simulation would be unreasonably expensive.

Nevertheless, an evaluation for the mesh quality is already given by the comparison of the numerical results to the available experimental data. To some extent, this might be even regarded as a more reliable proof that the mesh has been realized properly. Indeed, for the case under investigation, a good agreement with the experimental results is found, thus we simply conclude that the chosen mesh is opportune for the investigation purposes. If a confidence bound had been established before, it could have been also possible to infer whether the mesh was optimized or not (i.e. whether the

flow properties had converged). However, here the followed procedure is the reverse one, thus from the comparison we can just agree that the resulting confidence bound is proper for the investigation purposes.

Actually, a decision was made to reduce the domain extension, and the number of cells mentioned above is just half of the cell number of the original mesh attempt. Indeed, on the one hand it is true that the boundaries could not be moved closer to the turbine. However, on the other hand, one advantageous feature of the turbine on hand is that it is symmetric with respect to a mid-span horizontal plane. This allowed meshing and simulating only half of the domain and extend the results to the remaining part. Precisely, the upper half domain was selected, as shown by Fig. (4.7).

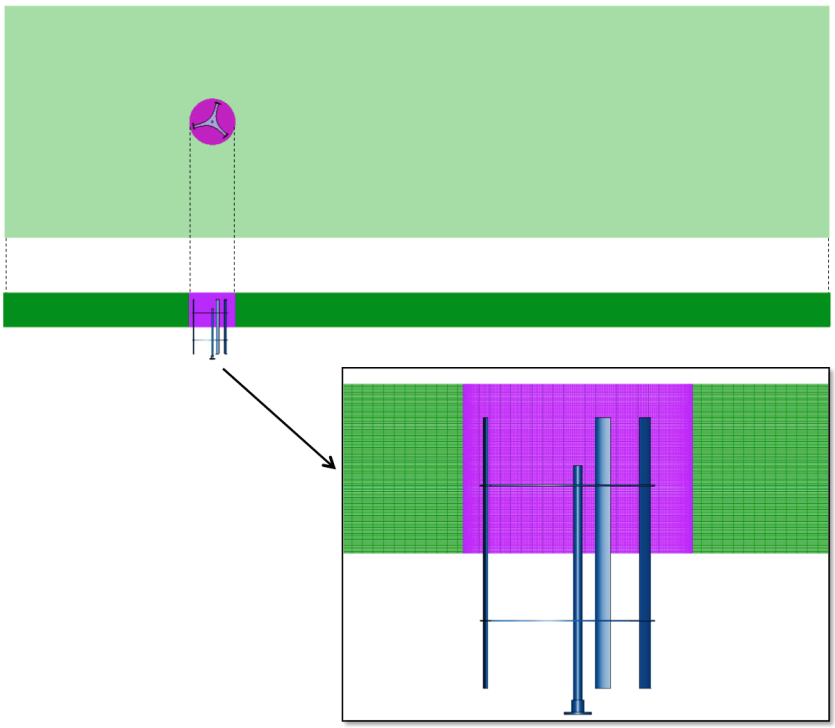

Figure 4.7: Upper symmetric domain; turbine detail.

4.4 Point of operation and flow condition

The measurements have been performed with diverse techniques (mechanical, structural and aerodynamical tools) and a comprehensive description

of the measurement set-up and test plan is provided by the reference paper [7]. Indeed, the numerical results have been derived along the same lines of the experimental test, i.e. the same quantities have been derived at the same measurement spots.

The fluid unsteady behavior has been described both upstream and downstream of the turbine, and the main aerodynamic quantities of the machine have been collected as functions of the rotor angular position. Specifically, much attention has been paid to the description of the wake in terms of both the deceleration and the deflection of the flow, due to the impact with the turbine as well as to the interaction among the wakes generated by each single blade.

To get a thorough description, the pressure and velocity fields have been evaluated on three different vertical planes, mounted transversally to the flow stream. With reference to Fig. (4.8), the three traverse planes are positioned at $x = -0.75D$ (denoted as *upstream*), $x = +0.75D$ (*near*) and $x = +1.5D$ (*far*), where D is the rotor diameter.

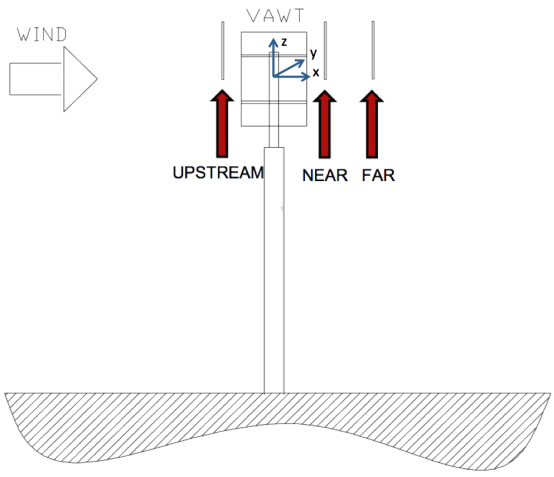

Figure 4.8: Traverse Measurement System

Also the experimental measurements have been performed for the upper symmetric part of the domain only. Thus, by selecting the numerical results from the CFD simulation on the same measurement planes, a direct comparison is possible. Indeed, both the experimental tests and the numerical simulation take advantage of the midspan symmetry, thus opting for a much cheaper procedure. In the end, for both the two cases, the traverse-plane extension exceeds the top of the blades of 25% their mid-span, to allow taking

into account the enlargement of the wake spanwise as well. The transversal dimension of the planes, instead, is the same as the one shown in Fig. (4.4), i.e. $\approx 6D$ in whole.

Actually, for the numerical simulation, the aerodynamic fields have been also evaluated on an extra plane, which is positioned horizontally and coincides with the symmetry plane. This plane will be particularly useful to derive information about the wake longitudinal extension.

Three different operating conditions have been investigated in [7]. Indeed, the wake description and the main aerodynamic quantities, such as the integral torque and power coefficients, have been derived for tip-speed ratios equaling 1.5, 2.5 and 3.5. The frontier cases respectively correspond to the lowest and the highest load conditions, while the intermediate case gives the maximum value for the coefficient of power. In [7], these different operating conditions have been obtained by setting the rotor angular velocity to a constant value of 400 rpm during tests and varying the air speed in the wind tunnel within a range of 6 to 16 m/s.

The experimental results for C_p as a function of λ (open chamber) are shown in Fig. (4.9). The corresponding trend for the torque coefficient, instead, is provided by Fig. (4.9).

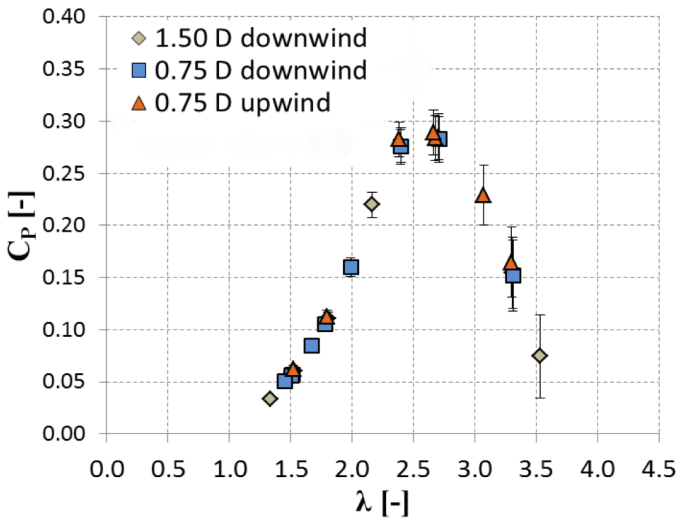

Figure 4.9: Coefficient of power from experimental tests.

The choice of the velocity range for the airstream depends on both the risk of damage for the turbine and the quality of measurements. In fact,

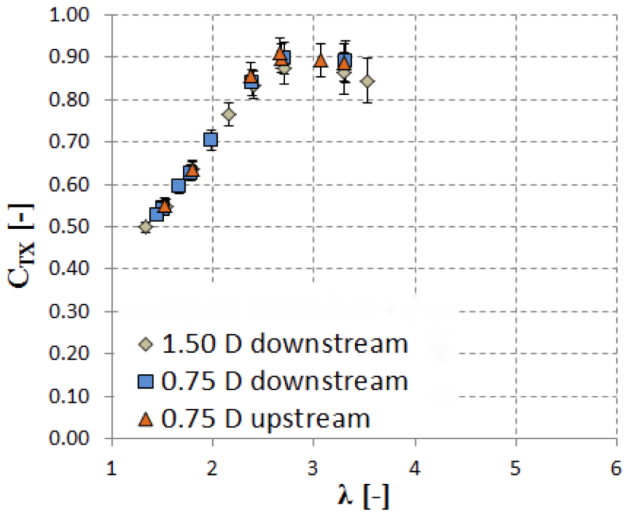

Figure 4.10: Coefficient of torque from experimental tests.

the highest threshold has been set to avoid structural problems in the test model, while the minimum threshold has to guarantee accuracy in the test results.

For what concerns the intermediate working conditions, they evidence the evolution of the unstable and time-dependent vortex generation process, especially at the tip-blades. A very interesting result is a non-symmetric dynamic stall occurring for $\lambda \leq 2$. The lift coefficient suddenly goes down as the blade orientation during rotation exceeds the critical angle of attack, and the flow detaches. This condition is crucial to understand the turbine behavior and, exactly for this reason, the case $\lambda = 1.5$ has been chosen for the numerical simulation presented in this work.

The undisturbed velocity of the flow is 14.2 m/s. In Ref. [7] this is the velocity measured at the turbine walls for the open-chamber configuration. This information implicitly takes into account any variation on the fluid velocity occurring in-between the generating fans and the turbine itself. In the numerical simulation, no variations for the wind velocity will occur in the upstream region, thus its value can be directly set to 14.2 m/s at the inlet section. For sure, this is also the velocity at the turbine walls.

By reversing Eq. (2.36), the rotational speed of the turbine is computed:

$$\omega = \frac{\lambda \cdot v_0}{R} = \frac{1.5 \cdot 14.2}{1.028/2} = 41.44 \text{ rad/s} \tag{4.1}$$

Chapter 5

Geometry Discretization

The spatial discretization of the domain is a crucial step in computational fluid dynamics and often takes the majority of the time spent on case set-up. The governing equations are discretized and solved at each subdomain, thus the computational grid directly affects the quality of the results. In this chapter, a broad overview on the parameters used to evaluate a good mesh is provided first. Eventually, the general meshing strategy will be presented and some past meshing attempts will be discussed with the aim of explaining the choices at the basis of the final result used in simulations. An insight into the *Sliding Interface* method and the usage of an *Arbitrary Mesh Interface* will be provided as well.

5.1 Requirements for a Quality Mesh (applied to the Case-Study)

It is extremely important to mesh the geometry in a proper way, since poor grids can increase the discretization errors and turn the adopted numerical schemes unstable. The key points to be taken into account are the problem geometry, the flow field and the requirements of the algorithm. The final computational grid is always a compromise between the accuracy of the solution and the computational cost involved. Indeed, these are opposed benefits and their balance largely depends on the level of refinement of the mesh.

The solution for achieving both accuracy and moderate cost is to select the most meaningful regions from the aerodynamics point of view and increase the mesh resolution in those subdomains only. Indeed, regions with high gradients are the ones to be refined, such as leading edges, boundary layers, shear layers, shock regions.

For the case-study under investigation, the most telling subdomains are

the layers adjoining the blades, where the impact with the flow occurs and turbulence is generated. However, as stated above, not only should the mesh refinement be based on the geometry, but also on the aerodynamic problem. In other words, not all the meshes realized at the boundaries of an airfoil profile are identical, but they also adapt to the physical problem (how the flow interacts with the blade itself).

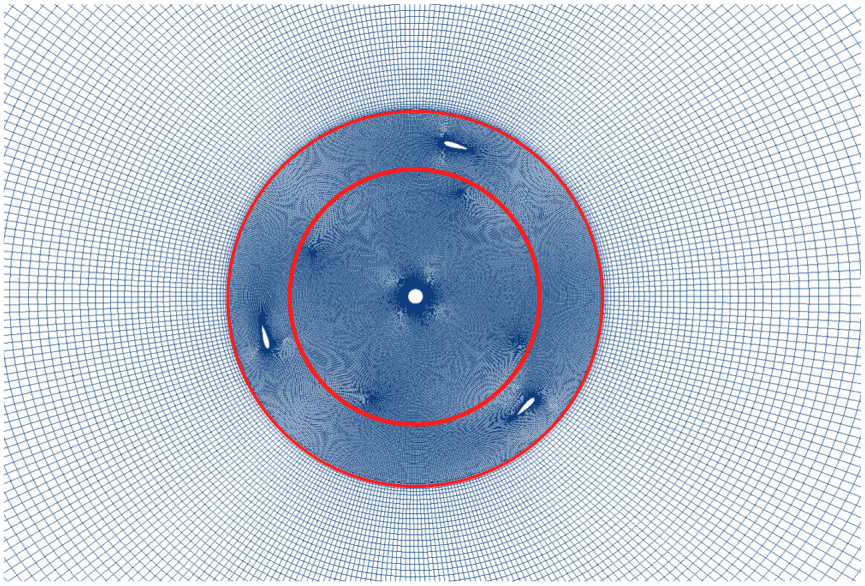

Figure 5.1: Mesh refinement about the turbine blades

This point is especially important for the case on hand, since the turbine rotates and, as a consequence, the flow impacts each blade at any angle of attack. More precisely, let us consider the very common case-study of an airfoil invested by wind, which arrives at an angle of attack $\alpha = 0° \div \approx 30°$ and let us suppose that the fluid regime is laminar. For this case, a good mesh is achieved by just refining the region closest to the leading edge.

For the specific case of this thesis, instead, this is not enough, since the two sides and the trailing edge also require a high level of refinement and actually this refinement needs also to be extended to the wake downstream of each blade, where turbulence is generated. After all, the study of the flow turbulent behavior after impacting the turbine is the goal of this thesis. Fig. (5.1) provides a *slice* of the 3D final mesh, which shows how the mesh refinement has been applied not only to the airfoil boundaries, but also to the whole annulus highlighted and, more widely, to the entire domain inside the external circumference (in red).

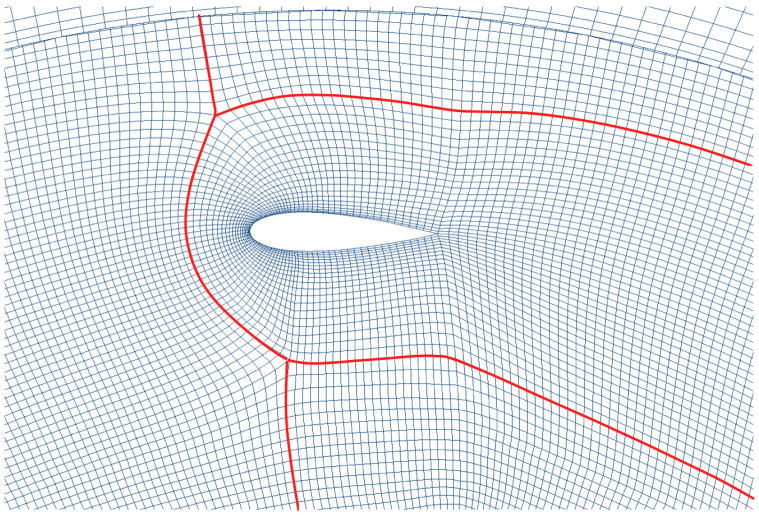

Figure 5.2: C-grid mesh structure for the blade

For the same reasons, a C-grid mesh arrangement has been chosen for the the blade region, as shown by Fig. (5.2). In fact, this mesh strategy –highlighted by the red connectors– differs from other techniques, such as the O-grid applied to airfoils, because it allows a high refinement level of the whole airfoil boundary and, at the same time, a good accordance with both the overall mesh domain and the physics of the problem. For instance, at the trailing edge, the cells align with the fluid flow, instead of arranging accordingly to circles all around the airfoil. This adaptation of the grid to the flow stream direction (and above all, to the flow physics, in terms of properties' variation) definitively helps the accuracy of the results.

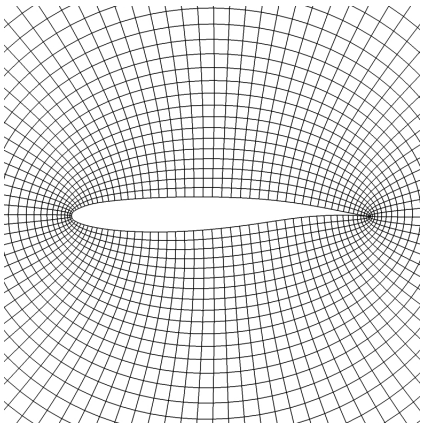

Figure 5.3: Example of O-grid arrangement

This requirement is often indicated as *body/flow conforming*, i.e. the mesh should properly follow the shape of the object and/or the flow. Among other things, for instance, it implies good cell orthogonality with respect to the wall boundaries and suitability with the circular overall mesh arrangement along the annulus highlighted in Fig. (5.1).

Other indicators for the mesh suitability are the *non-orthogonality*, the *skewness* and the *aspect ratio*. The first parameter straightforwardly measures the non-orthogonality between subsequent sides of adjacent cells. Indeed, orthogonal cells are preferred. The second parameter, instead, measures how much each cell deviates from a perfectly equiangular one (for instance, an optimum condition for a quadrilateral cell would be angles close to 90°). In general, cells should not be too stretched diagonally, with very acute angles. In the end , the third parameter is the ratio of the longest to shortest side of a cell, and should better approach value 1. An $AR \gg 1$ is only used for boundary layers, as wall functions do require a mesh refinement. Therefore, at the walls the cells are usually lengthened alongside the object profile and gradually increase their thickness towards an optimum AR. Actually, there is still a condition to be added for a good mesh. This requirement is *smoothness*: for instance, no sudden jumps should occur in the side length of adjacent cells.

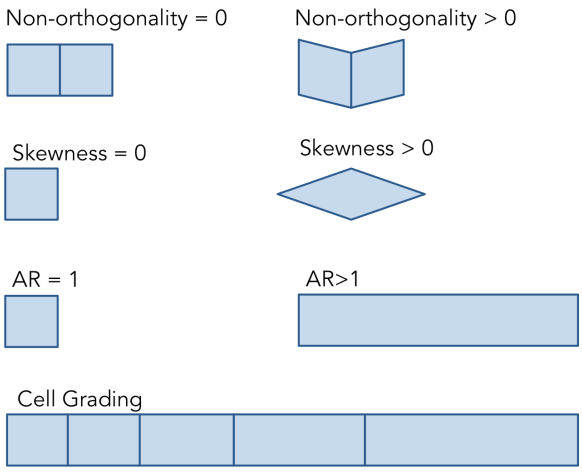

Figure 5.4: Skewness; Aspect Ratio; Smoothness

Fig. (5.4) provides a simple illustration of these three indicators, which are fundamental for a good mesh. Indeed, they widely conditioned the final mesh for the analyzed case, thus their definition is very important to understand some of the choices made, which will be discussed later on in this chapter.

5.2 Meshing Strategy

The mesh has been realized with the mesh generator Pointwise®, by starting from a geometry file supplied in the Stereolithography format (STL). The final grid includes $\approx$ 45 M volume cells. It is perfectly *mapped* and hexahedral. As already stated in Ch. (4), only half of the fluid domain has been simulated, since the geometry is perfectly symmetrical.

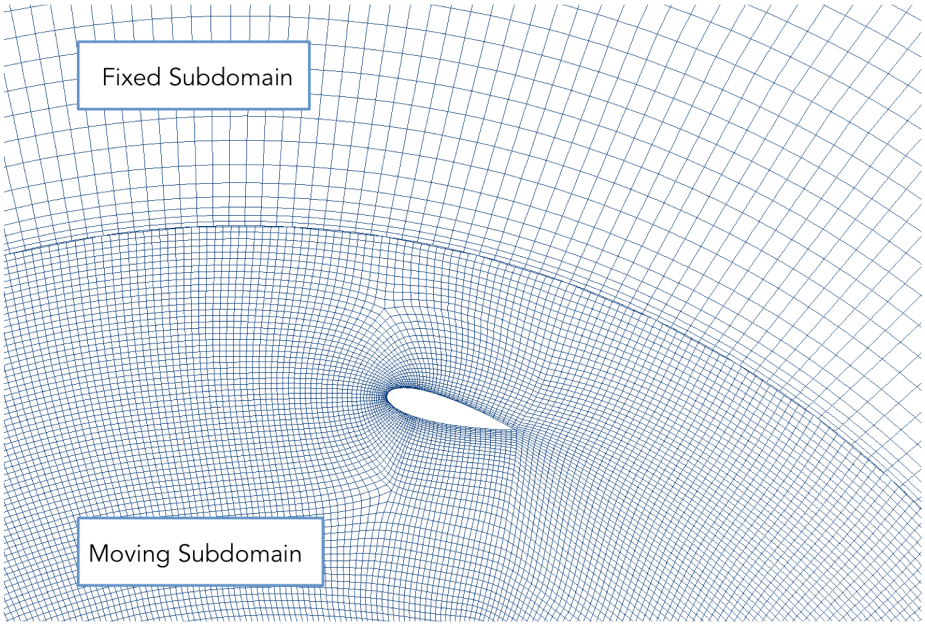

Figure 5.5: Change in resolution across the Arbitrary Mesh Interface

Moreover, the domain has been split into a cylinder, which includes the turbine and rotates with it, and and external outer domain, which is still. This has been possible thanks to an *Arbitrary Mesh Interface*, which allowed handling the interpolations of the results at the cylinder lateral surface. An insight into this tool will be provided in the next section. This also allowed discretely switching from a very refined mesh at the inside to a coarser mesh at the outside, as shown by Fig. (5.5). As will be proved by the results, this sudden change did not affect the simulation, since it has been observed that the aerodynamic quantities smoothly vary across this interface to the extent that it is impossible to notice it in the final solution by looking at the pressure and velocity fields. Thus, this strategy has definitively turned out to be a good option.

The outer domain is composed by cells that gradually increase their size as they get further from the turbine. In particular, at the left end of Fig.

(5.7), corresponding to the region closest to the outlet section, the cells exhibit a very high aspect ratio. Nevertheless, despite this low quality parameter, equations are not affected by it if the flow impacts the cells in a direction that is perfectly aligned with the cell orientation (in this case, it is aligned with the stretched sides of the cell). Therefore, since the outer domain does not move and these cells are far enough from the turbine, the flow crosses them perfectly along the longitudinal direction, thus the high aspect ratio does not represent an issue. After all, the huge extension of the domain has been set to isolate the boundary effects, but turbulence does not propagate at that distance.

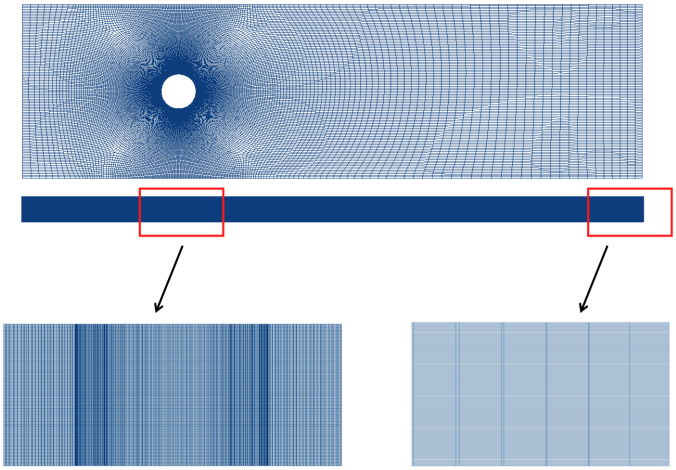

Figure 5.6: Outer Domain (fixed)

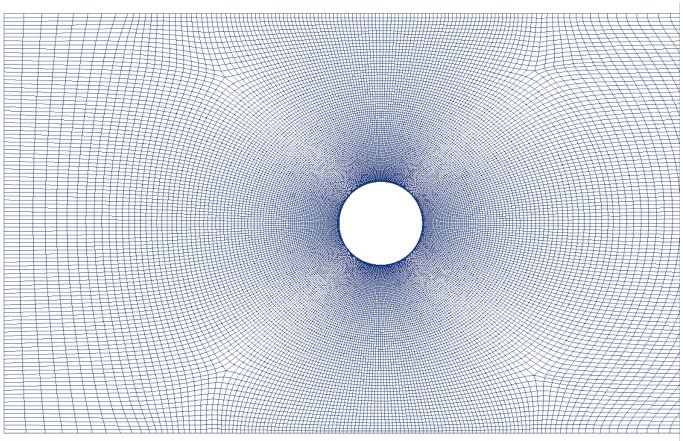

Figure 5.7: Detail of the outer domain.

Let us now focus on the inner domain. By looking at the geometry of the turbine, it can be noticed that one obstacle is represented by the presence of the horizontal support (only one in the symmetrical part analyzed). In fact, sudden changes in the geometry occur along the vertical direction, as shown by Fig. (5.8).

To deal with this issue, the overall domain has been split in four different sub-volumes along the vertical direction and a 3D-grid has been realized for each of them separately. Precisely, for each block, a 2D-mesh has been created first and it has eventually been extruded, by also taking into account a proper refinement in the vertical direction. For instance, along this direction, the grid is more refined close to the upper/lower faces of the horizontal support, in such a way that a boundary layer is realized for this latter.

In the end, non-conformal meshes at the interfaces have been stitched together. Each of these static couplings has been achieved with a *Sliding Interface* (actually an enhanced version with respect to the one available in the official OpenFOAM®distribution), which will be deepened in the next sections.

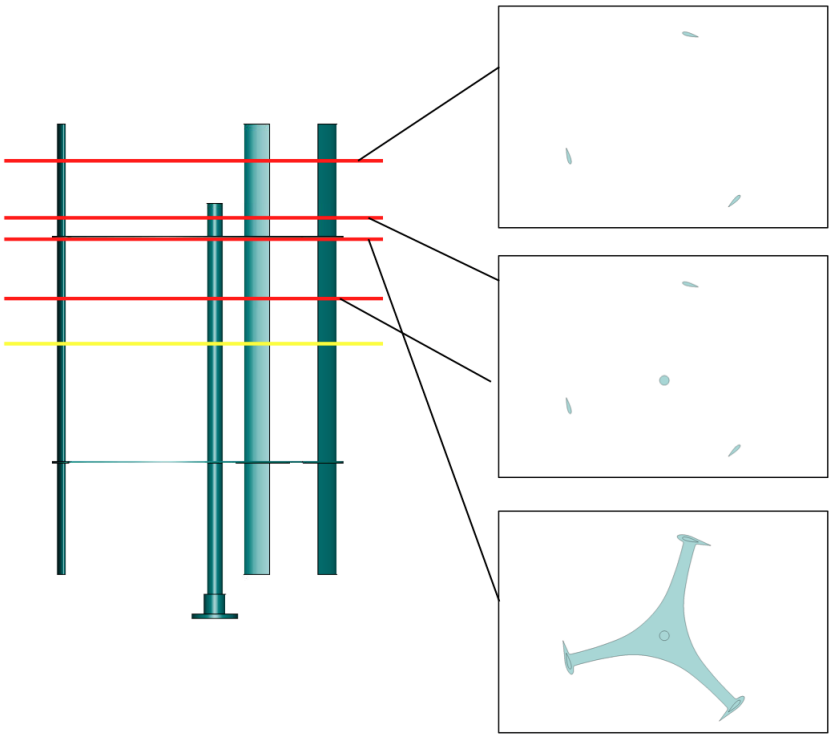

Figure 5.8: Geometry horizontal sections

Fig. (5.9) shows how the moving domain has been split into sub-volumes. A zoomed view of the non-conformal meshes is, instead, provided by Fig. (5.10), with details in Fig. (5.11) and (5.12) . Surface 3b is not taken into account since stitch 3 is identical to stitch 2. The issues related to the stitching operation will be discussed in the next sections. Some of the attempts made prior to the final computational grid will also be taken into account, since they help understand how the issues due to stitching affected the final grid.

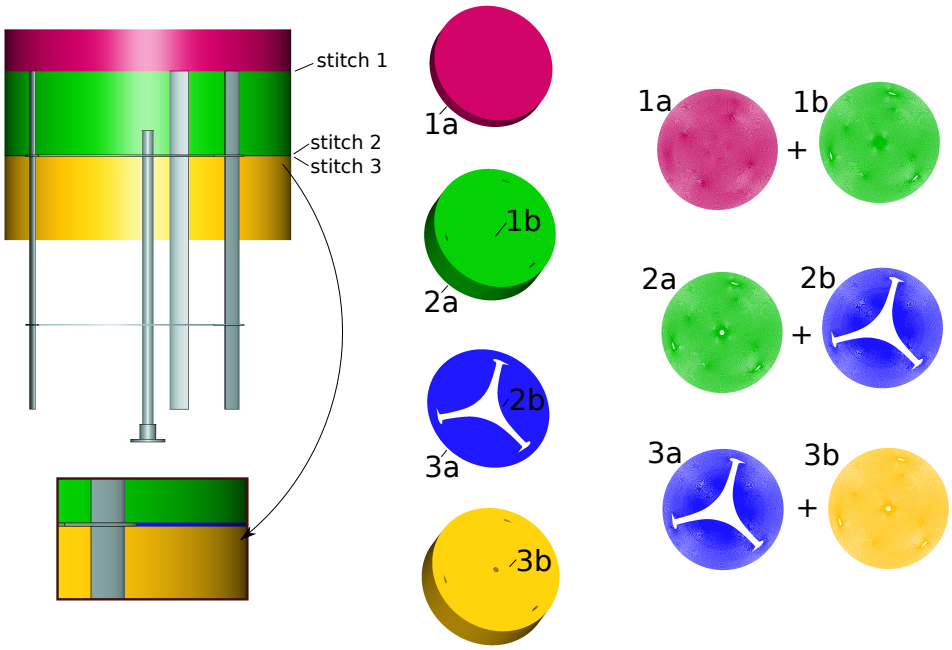

Figure 5.9: Sub-volumes for the inner domain

5.3 Arbitraty Mesh interface

Since a dynamic mesh is required to allow motion, the domain was split into a rotating cylinder and a fixed parallelepiped. There are different solutions to deal with the interface, i.e. to make the results uniform across the common edge surface.

For instance, these solutions include finite-element based multipoint constraint methods [10], interface capture and tracking methods [29] and cell centered finite volume methods (CCFVM), which are based on a flow matching protocol [18].

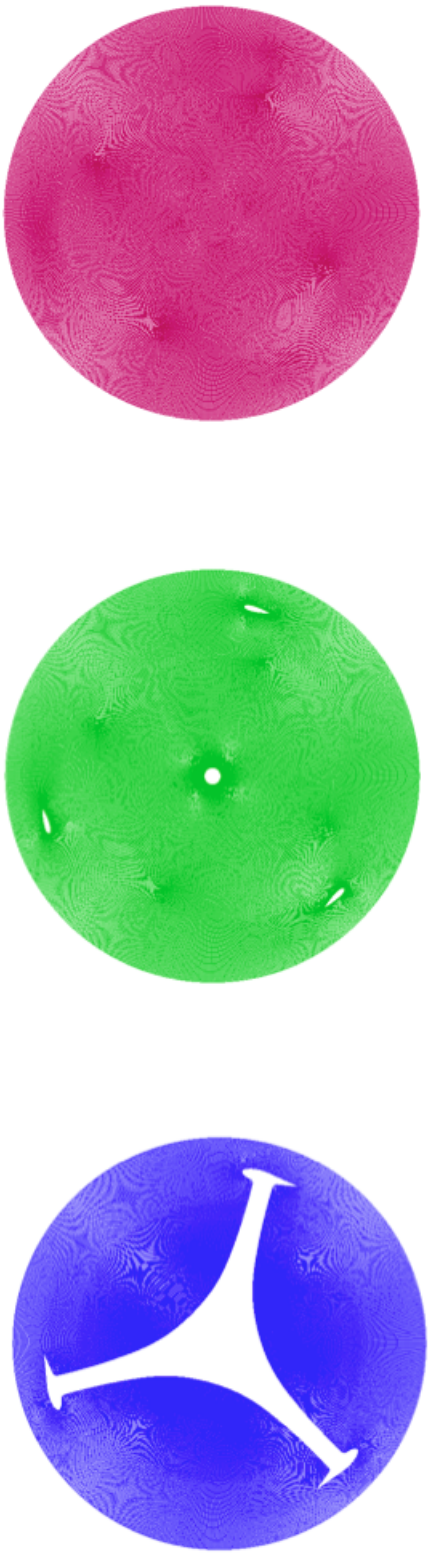

Figure 5.10: Meshes 1a, 2a, 3a

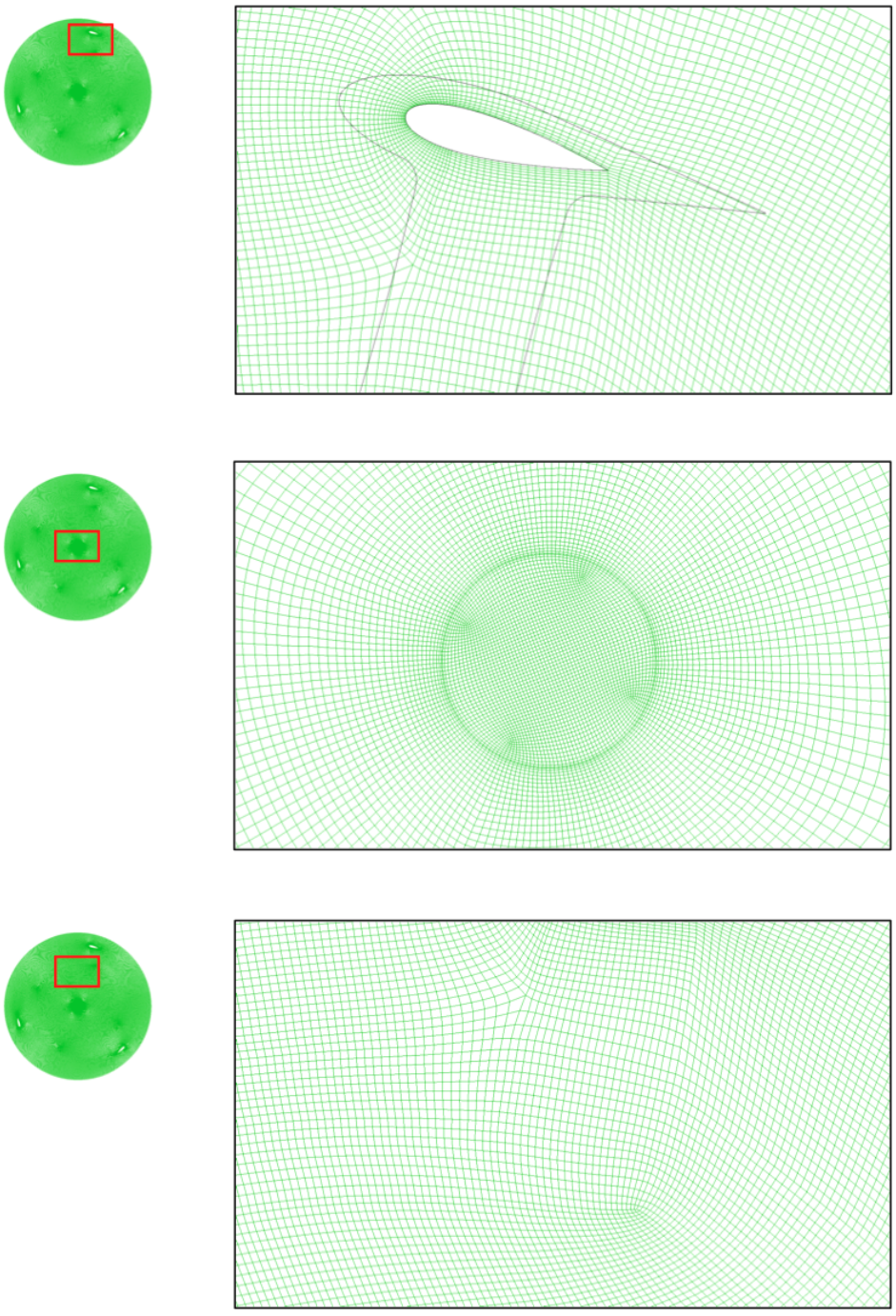

Figure 5.11: Mesh 2a: details

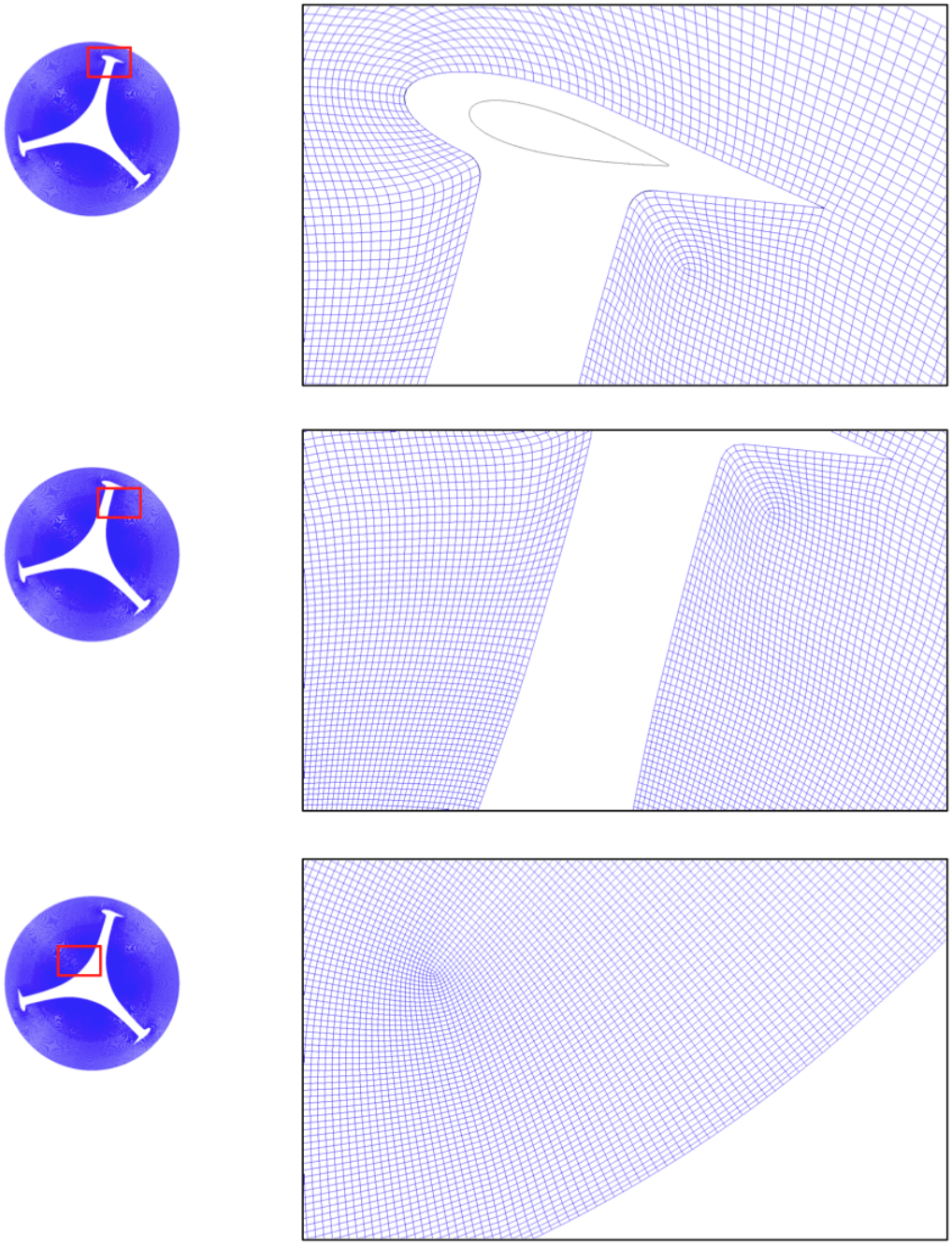

Figure 5.12: Mesh 3a: details

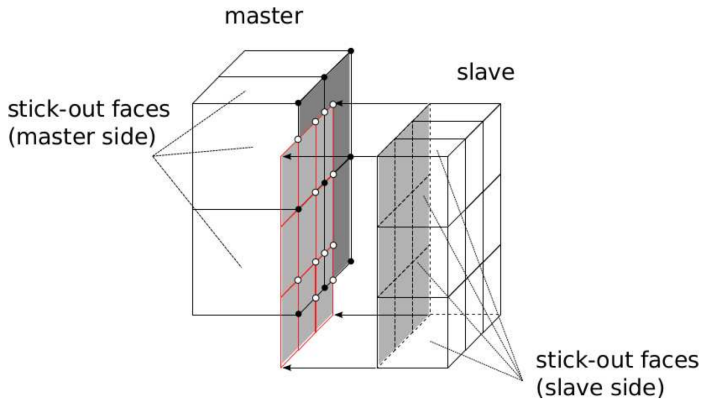

Figure 5.13: Sketch of the Sliding Interface operation

For the case on hand, the adopted strategy is an *Arbitrary Mesh Interface*. At the common cylindrical interface, the two domains do have distinct lateral edges, but their positions overlap (this cannot be noticed from the pictures, since the two surfaces seem to perfectly coincide). Therefore, this technique allows simulations across these disconnected (but adjacent) mesh domains, on condition that they are coupled to each other through the `cyclicAMI` boundary conditions. This tool does not involve any topological changes to the adjoining computational grids and, indeed, it operates by interpolating the computed fluxes at the interface.

For the analyzed case, the AMI tool has performed very successfully, since no sudden variations in the pressure and velocity field results are visible at the interface, but properties smoothly varies throughout the whole domain. This will be shown and discussed specifically in Ch. (8).

5.4 Sliding Interface

As already mentioned, the computational grid for the inner domain (the rotating cylinder) has been realized by stitching together 4 different sub-blocks. The tool that allows static coupling is called *Sliding Interface* and operates by causing topological changes to the adjacent non-conformal meshes to be stitched.

The way this tool operates is soon explained. Firstly, it distinguishes the nodes belonging to one surface from the ones belonging to the other one, since the basic requirement is that the two surfaces must not share com-

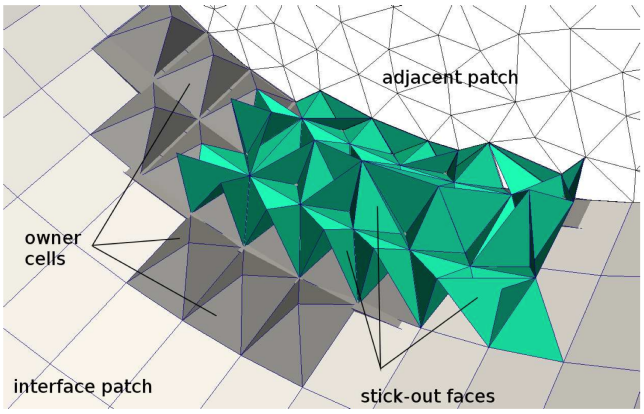

Figure 5.14: Sliding Interface 3D operation

mon points (even if they overlap). The nodes from the surface identified as *slave* are then projected onto the *master* surface, where the cell sides are rearranged by taking into account also the new added nodes. As the node clustering is spread over the interface, towards both the two sides, continuity is restored between the two adjoining sub-volumes automatically.

Fig. (5.15) and (5.16) show the overlapping stitched meshes. They help figure out the great flexibility allowed by non-conformal interfaces in building the mesh (increased D.O.F.). Realizing a single block manually for the inner domain would have been really hard and would have surely led to worse quality. Indeed, it has been possible to focus on each single 2D mesh and optimize it, without considering their connections, which have been realized automatically.

Actually, this is not completely true, as the method does involve some compromise to work properly. The coupling of non-conformal interfaces, indeed, can sometimes generate very distorted cells that connect the two domains or warp the adjacent ones that already exist. When exporting the mesh to OpenFOAM®, it then turns out that the mesh is not suitable for proper simulation, since it does not satisfy the requirements of low *skeness* and *aspect ratio* at some cells.

It must be clarified that, by opportunely setting the right tolerances, the stitch hardly fails. However, with too large tolerances, the result can sometimes not be the accurate one expected. This is the reason why the final mesh is the result of numerous attempts and some important decisions have been made prior to it. The most meaningful attempts will now be briefly illustrated, just to understand the reasons that have led to the final grid.

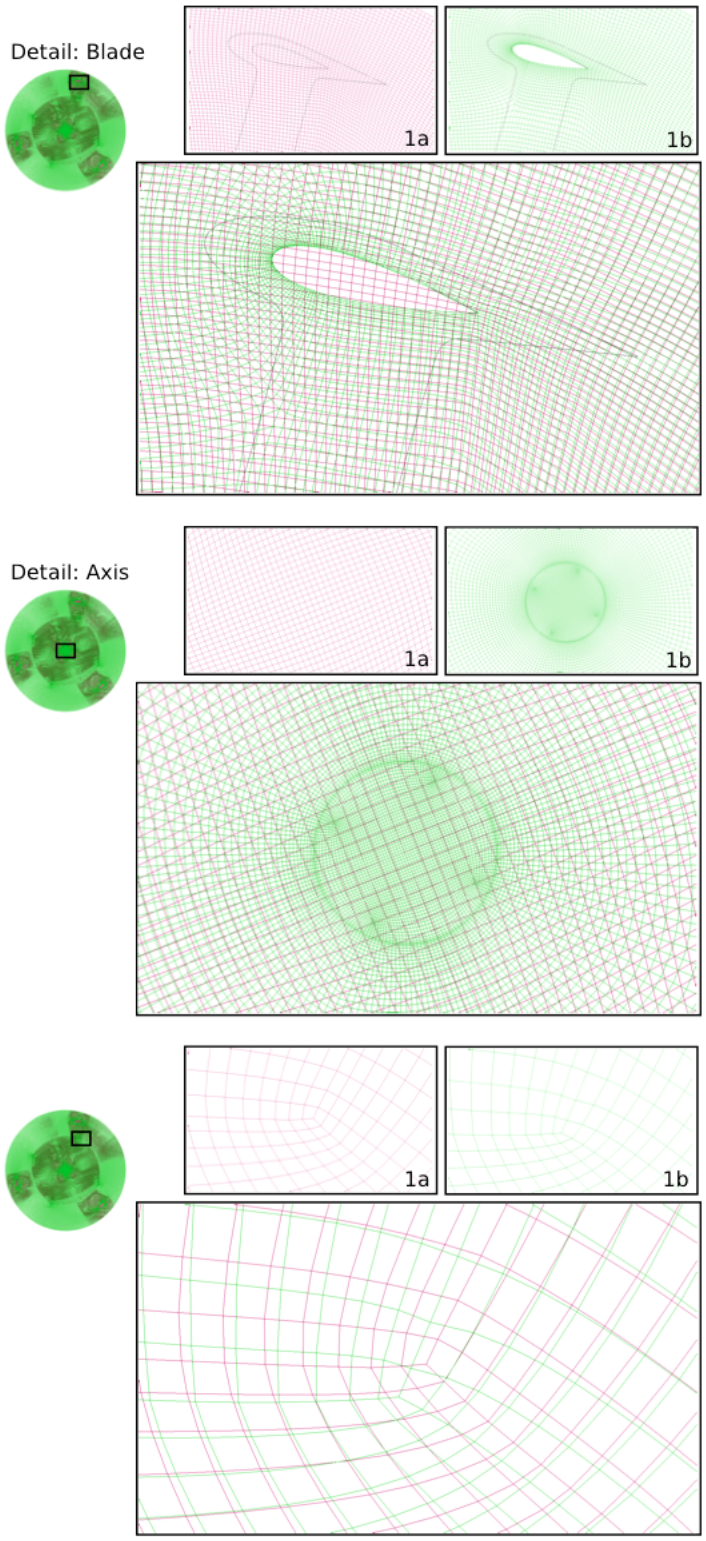

Figure 5.15: Details from stitch 1

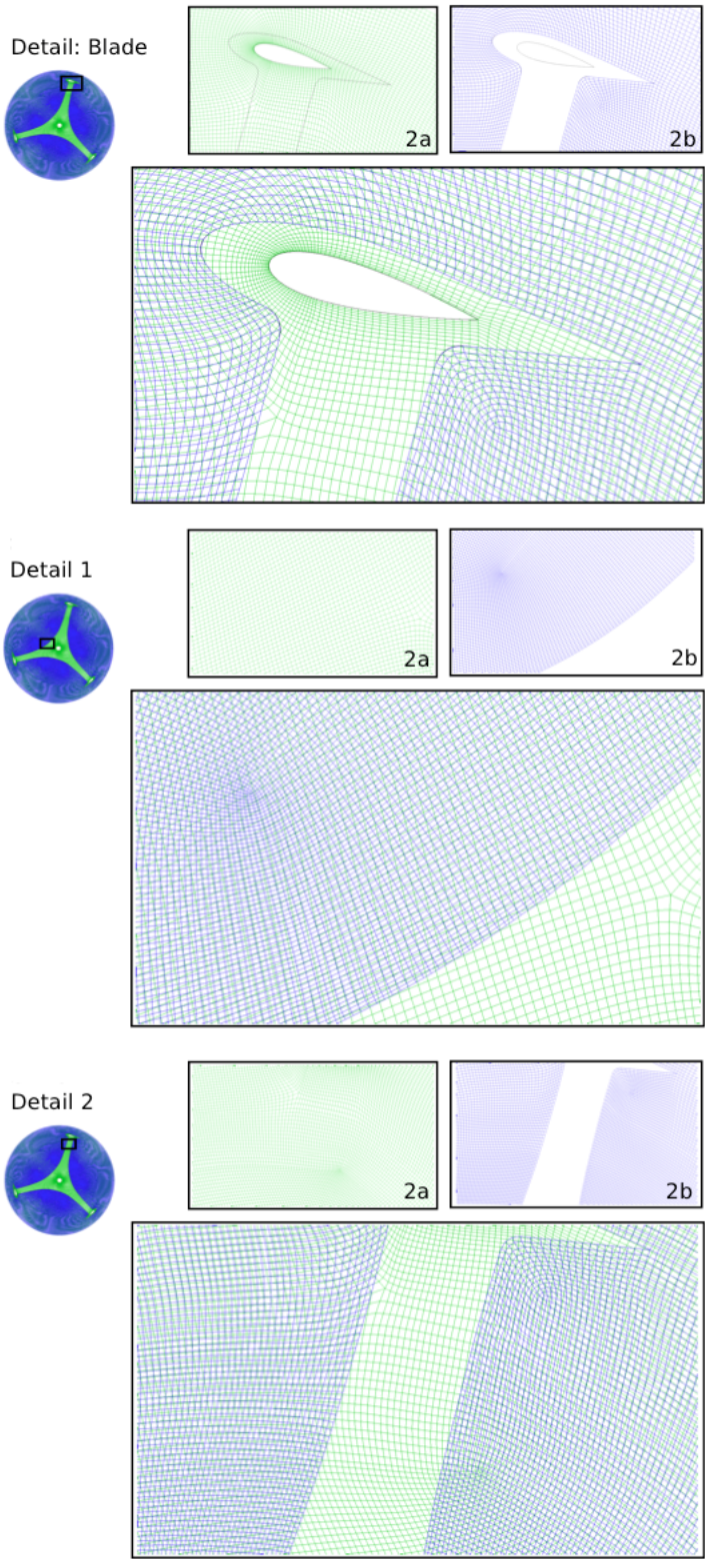

Figure 5.16: Details from stitch 2

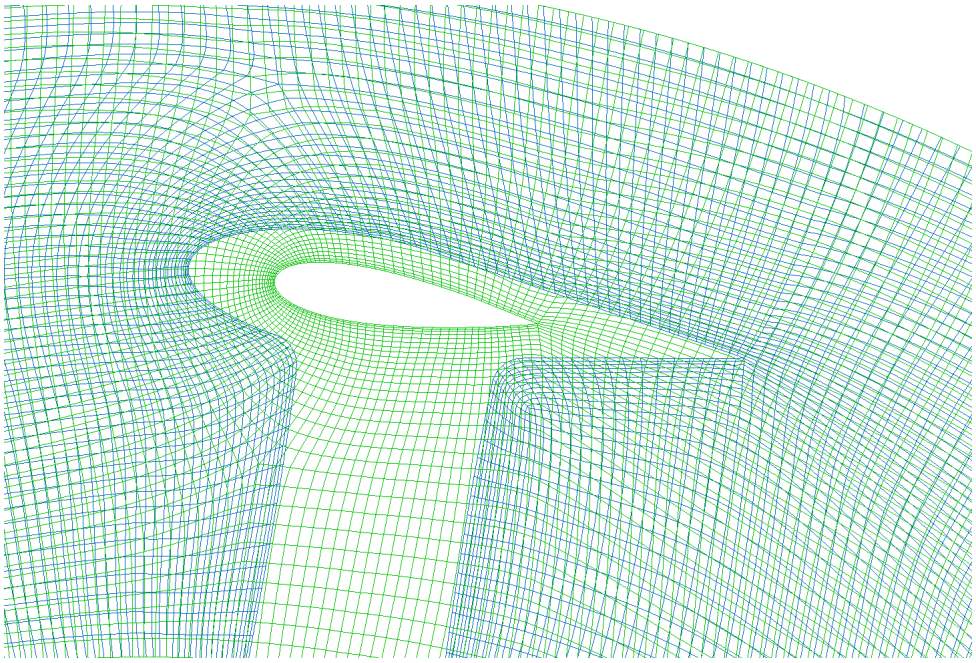

Figure 5.17: Blade/support boundary layers overlapping (past attempt)

Let us consider the 2D mesh corresponding to the horizontal support, whose details have been provided by Fig. (5.12). It can be noticed that there is no boundary layer at the sides of the support, i.e. the wall-adjoining cells exhibit an aspect ratio that approaches 1. This feature is intentional and stems from a precise choice. Indeed, let us consider Fig. (5.17), showing the overlapping grids realized in a past attempt, and Fig. (5.18), zooming on the boundary layer for the support grid.

A mesh refinement at any wall is always recommended. However, as it can be noticed, in this way cells with very different dimensions come in touch when stitching the two domains. The result will evidently be very distorted cells, which can cause errors in the numerical results. This is the reason why the domain corresponding to the horizontal support has been meshed as shown by Fig. (5.12).

A similar (but alternative) choice could have involved the blade domain, instead of the support. The reason for which the support boundary layer has been removed instead of the blades' one is quite straightforward. Basically, the boundary layer is important and its absence always leads to a lack in the result accuracy. By looking at the vertical extension of the cylinder sub-domains, it can be noticed that the support height is widely smaller than the blade span. Thus, the error committed by removing the boundary

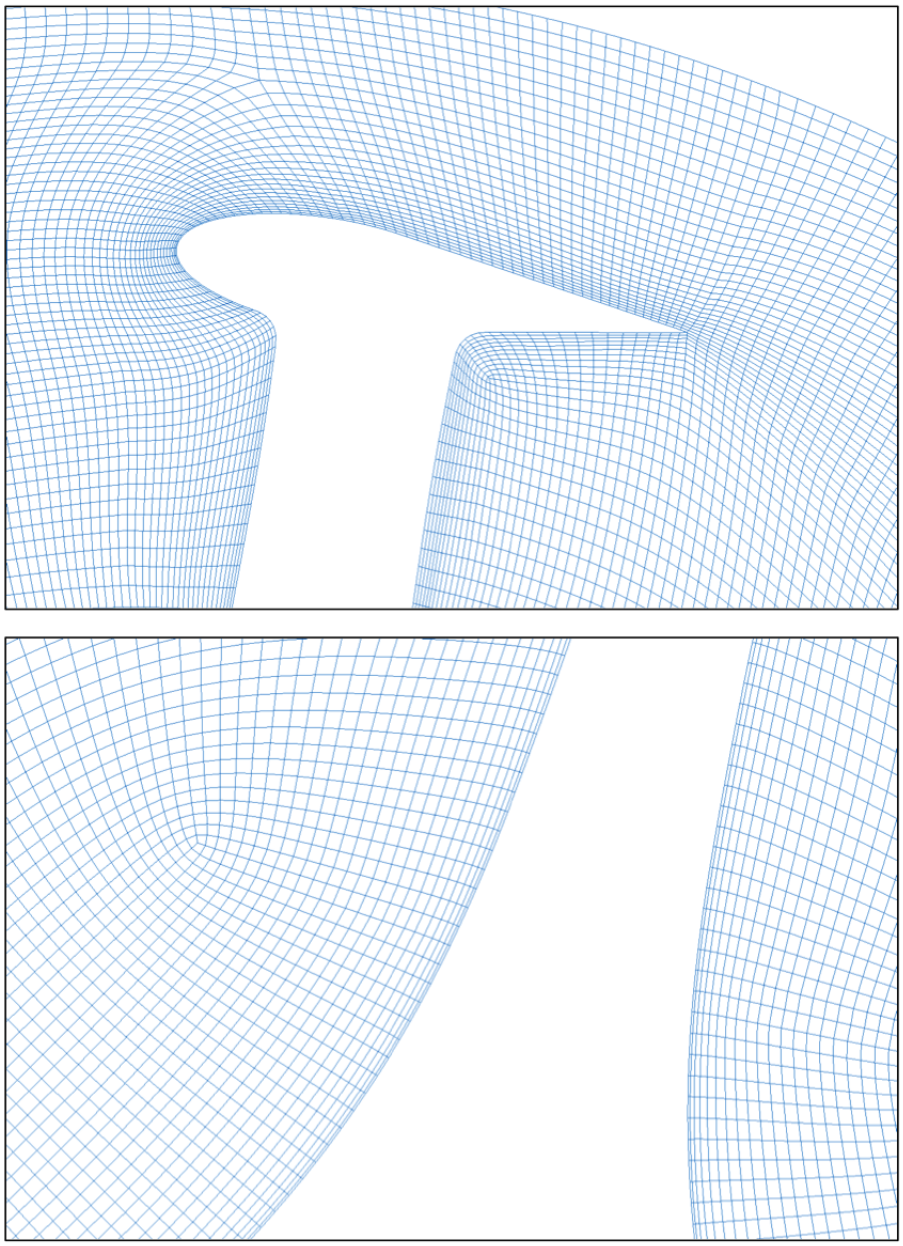

Figure 5.18: Boundary layer at the sides of the support (past attempt)

layer at the support sides is definitively negligible with respect to the error that would stem from the absence of a mesh refinement at the blade sides. Moreover, the physical problems is the aerodynamic interaction of the fluid with the blades, and the supports just represent necessary structural components for the turbine.

An alternative that was also taken into account has been to realize a proper boundary layer for the support and then project the geometry-adjoining nodes to the inside, up to the blade walls, in such a way that the boundary layer for this latter stems from the one created on the support. Even if this solution might seem convenient, actually the mesh quality at the blades' sides (at the best one can do) turns out to be still very poor, which is definitely not worthy. Moreover, by deriving the new boundary layer from the one at the support sides, the grid becomes extremely refined at the blades' wall and the implication is an extremely small δt for the simulation due to the Courant-number restriction.

Back to the case, after modifying the grid corresponding to the boundary layer at the support sides, in order to further ease the stitching procedure (or maybe, for an excess of zeal), other mesh variations have been done. For instance, Fig. (5.19) shows how the indicated node, connecting five cells (which could be troubling), has been moved to another location. Indeed, in the new position, it ends up at the fluid/wall interface, instead of the interface between two fluid regions to be stitched.

For the same reasons, the trends of the connectors from the two adjoining meshes have been somehow more evened out. It can be noticed from Fig. (5.20) that, especially at the blade suction side and downstream of the trailing edge, the computational grids seem to better agree (they turn out to be –let us say– *less* non-conformal) in the final solution adopted with respect to the previous attempts.

The last (past) attempt that is worth being considered is the one shown by Fig. (5.21) and Fig. (5.22). Indeed, at the beginning the idea has been to just refine the annulus that includes the blades. In fact, from experimental results and from the 2D preliminary simulation performed, a main trend of the blade wakes perfectly according to the blade trajectories could be inferred. Thus, this option would have allowed saving a number of cells and at the same time achieving the same high level of accuracy in the results.

Again, the reason why this option has been overtaken is represented by the difficulties encountered at the stitching step. In fact, splitting the inner domain into an inner cylinder and an outer hollow cylinder, would have required to stitch their lateral common sides as well, by further complicating

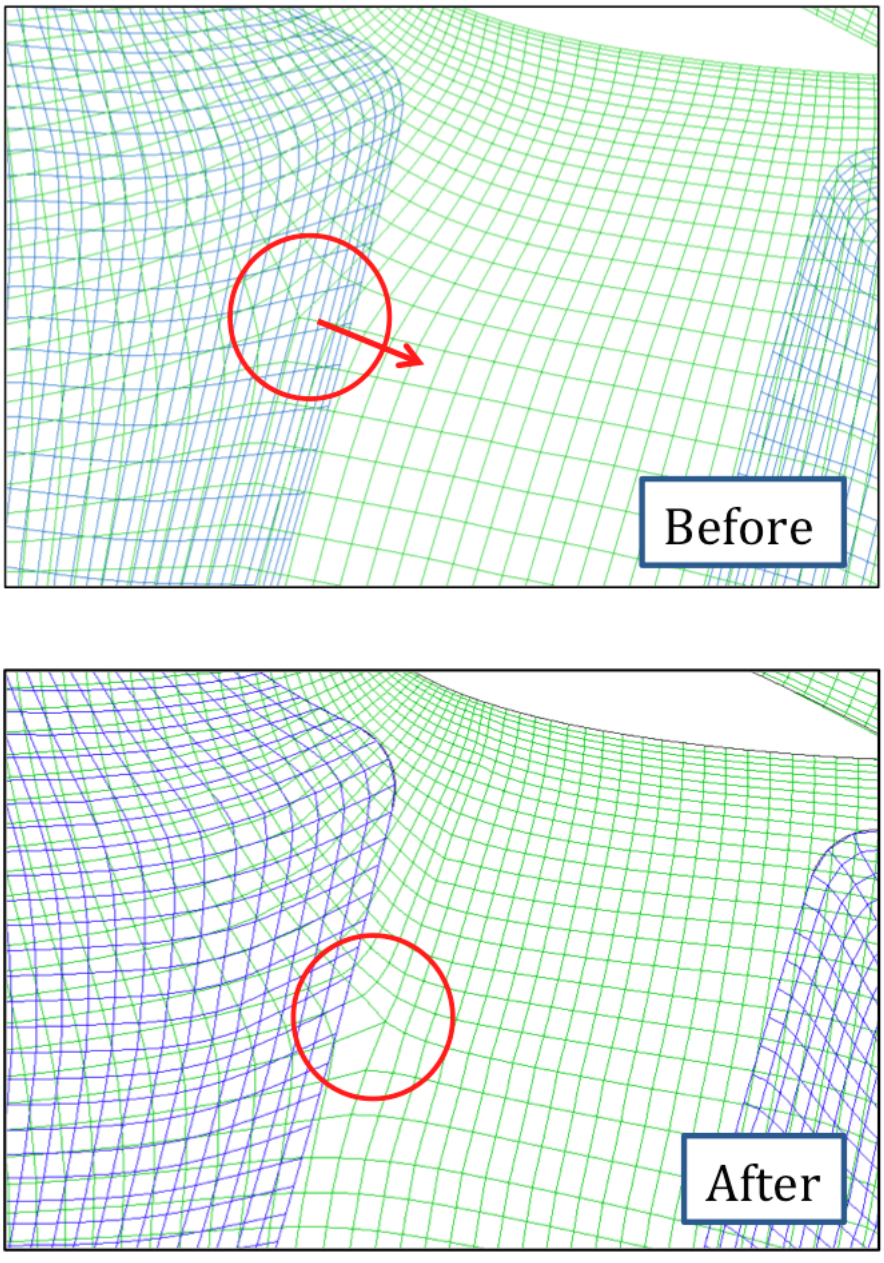

Figure 5.19: Example of re-meshing to facilitate the stitching procedure

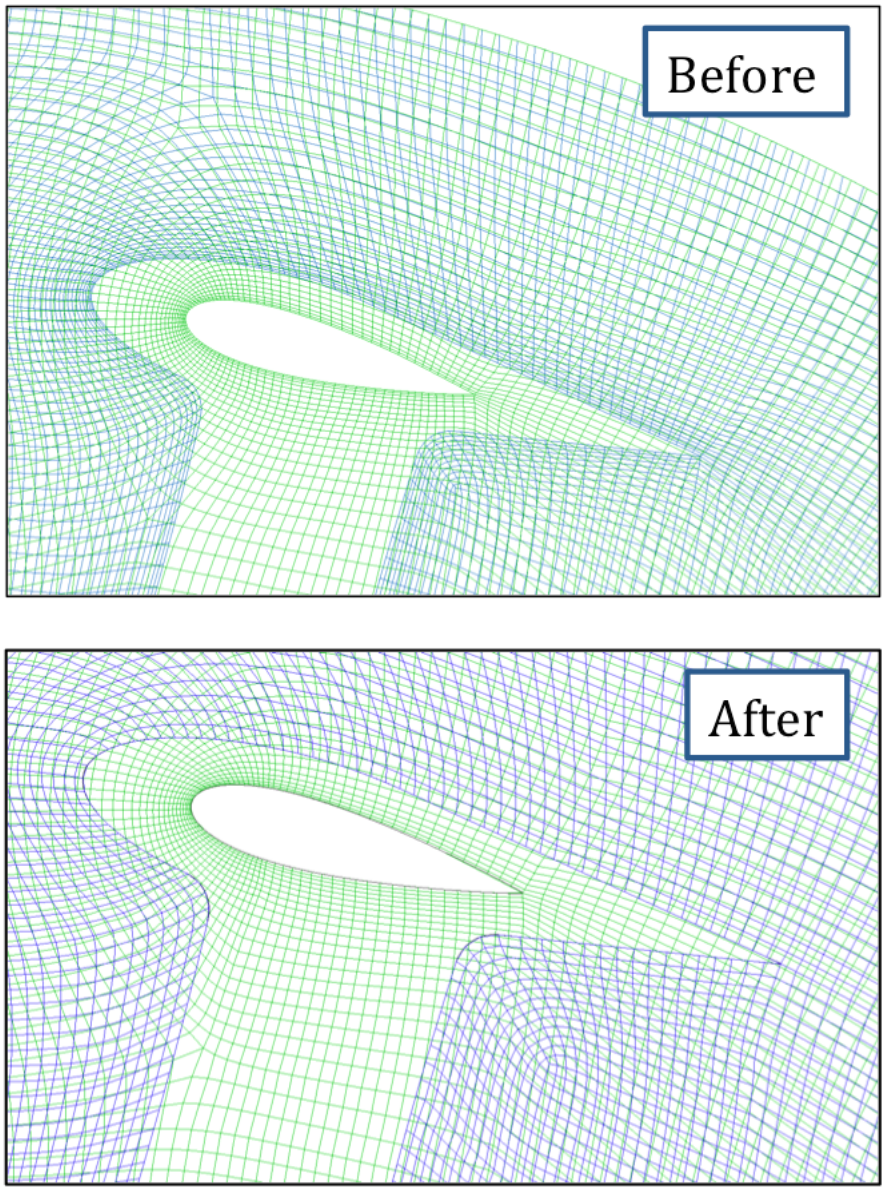

Figure 5.20: Re-meshing detail

the procedure. In the end, the option of a larger number of cells prevailed in the trade-off.

Alongside with all these considerations, it can be noticed that a very drastic option could have also been to completely remove the support from the simulation. The 3D simulation would have still differed from the 2D one (3D is necessary for turbulent flows) and the numerical approximations due to improperly-meshed boundary layers would have been avoided. However, this option has not been taken into account because it is definitively non realistic. Trivially, an approximated solution confined in some regions of the computational domain (the ones closest to the support) is better than a completely different case-study.

Moreover, the absence of a component would have made the simulation underestimate its interference with the fluid flow, while the risk of an approximate solution is –for this case– an overestimation of this interaction. Thus, from strictly the point of view of engineering, as the simulation is performed to help design and optimize the turbine, it is actually crucial to take the support into account as well.

In the end, it should be noticed how the choice of focusing on half domain (thanks to symmetry) has hugely facilitated and fastened both the case set-up and simulation. Indeed, on the one hand, it allowed for a drastic reduction of the total number of cells, but on the other hand it also allowed considering just one support. In other words, only three couples of adjacent non-conformal meshes have been stitched together, but the number could have been the double.

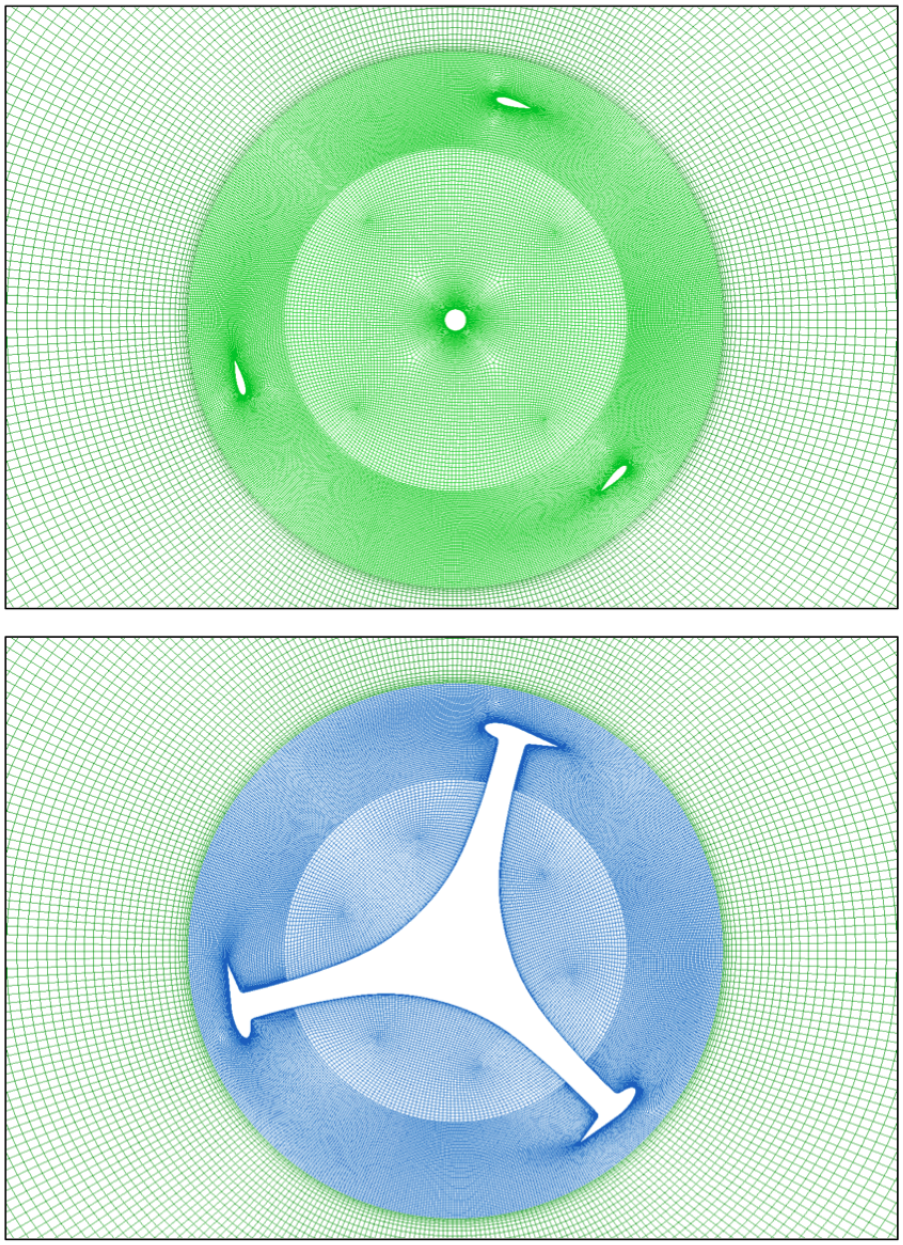

Figure 5.21: Annulus refinement (past attempt)

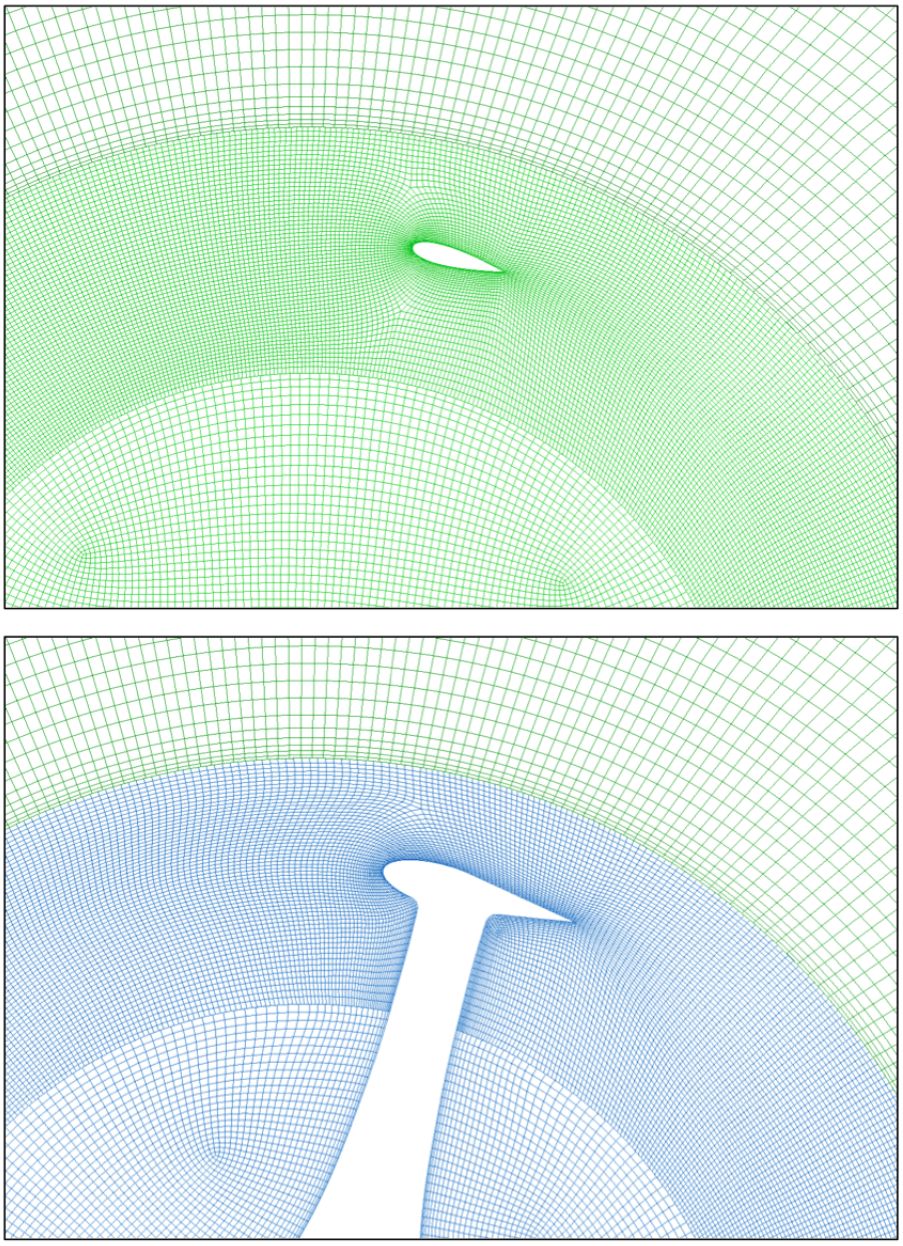

Figure 5.22: Annulus refinement detail (past attempt)

Chapter 6

Case Set-Up in OpenFOAM®

In this chapter, the OpenFOAM®set-up for the case under investigation will be discussed. It will be first shown how to configure the mesh movement and define the fluid and turbulence properties. Eventually, the settings for the turbulence model and solver will be presented, together with the numerics set-up. In the end, this chapter will deal with boundary and initial conditions.

6.1 Configuring Mesh Movement

The *Sliding Interface* method and the adoption of *Arbitrary Mesh Interfaces* have already been widely discussed in Ch. (5). The rotational velocity of the moving domain is set to 41.44 rad/s in subdirectory `constant/dynamicMeshDict`. The reference system for the mesh exported from Pointwise®is already aligned with the rotor axis, thus the rotational axis is simply set to (0 0 1).

```
solidBodyMotionFvMeshCoeffs
{
    cellZone        rotor;
    solidBodyMotionFunction  rotatingMotion;
    rotatingMotionCoeffs
    {
        origin        (0 0 0);
        axis          (0 0 1);
        omega         41.44; // rad/s
    }
}
```

6.2 Fluid Properties

Fluid properties are specified in `constant/transportProperties`.

Precisely, the value to be defined is that of the fluid kinematic viscosity ν, which is constant since no heat transfer occurs and the fluid is treated as incompressible. Indeed, this last assumption holds if the flow Mach number is lower than value 0.3, which is the case. Thus, even if the turbine is invested by air, which is evidently a compressible fluid, this can be treated as incompressible for the reason explained.

The value set for ν is $1.55 \cdot 10^{-5}$ m^2/s.

```
nu [0 2 -1 0 0 0 0] 1.55 E-5;
```

6.3 Control of Time and of Data-Reading/Writing

Input data relating to the control of time and reading/writing of the solution data are specified in the `system/controlDict` dictionary.

The first specification is the `application` entree. For the case on hand, the solver `pimpleDyMFoam` has been chosen. It consists in a transient solver for incompressible flows (which is consistent with the explanation provided in the previous section) of Newtonian fluids on a moving mesh and uses the PIMPLE algorithm.

The results have been saved at each degree of the rotor revolution. This means that, by considering the rotational speed of the turbine in [°/s]:

$$\omega = 41.44 \text{ rad/s} = 2374.337103 \text{ °/s} \tag{6.1}$$

the time step duration is:

$$dt = 4.211701863 \cdot 10^{-4} \text{ s} \tag{6.2}$$

Moreover, the end time for the simulation has been set in such a way that it allows for approximately 5 complete revolutions of the turbine. Therefore, if one single revolution takes:

$$t(1 \text{ rev}) = \frac{2\pi \text{ rad}}{41.44 \text{ rad/s}} = 0.1516212671 \text{ s} \tag{6.3}$$

the end time is then set to:

$$t(5 \text{ rev}) = 0.7581063353 \text{ s} \approx 0.76 \text{ s} \tag{6.4}$$

The maximum Courant number has been set to value 5.

Moreover, it should be noticed that for the specific case investigated, the `system/controlDict` dictionary also includes the libraries for the implementation of the functionObjects used to save data for post-processing.

Specifically, the main aerodynamic quantities have been computed, at every time-step, referring to each single blade, to the whole machine, and to the planes corresponding to the traverse measurement system used in experimental tests.

6.4 Numerics Set-Up

The adopted turbulence model is the *Dynamic Length-scale Resolution Model*, widely discussed in Ch. (3). This has been specified in the `constant/RASProperties` dictionary.

The `system/fvSchemes` dictionary, instead, sets the numerical schemes for terms, such as derivatives or gradients in equations, that appear in applications being run.

For time derivatives, a second-order backward scheme has been chosen. Indeed, with respect to an Euler scheme, which is very typical for simulations using RANS models (especially for stability), it gives more accuracy when using DLRM and prevents from numerical diffusion.

Secondly, a second-order LUST scheme (limited, low diffusivity) [30] has been chosen for divergence $\nabla\cdot$ terms ($\nabla \cdot \mathbf{UU}$).

In the end, a second-order scheme, corrected for non-orthogonality, has been selected for the laplacian (specifically, for $\nabla^2 p$ that appears in the Navier-Stokes equations).

In the `system/fvSolution` dictionary, instead, the parameters controlling the pressure-velocity coupling algorithm used for the simulation (PIMPLE) are specified as follows:

```
PIMPLE
{
    correctPhi          yes;
    nOuterCorrectors    50;
    nCorrectors         3;
    nNonOrthogonalCorrectors 0;
    pRefCell            0;
```

```
    pRefValue           0;

    turbOnFinalIterOnly on;

    residualControl
    {
        "(p|U)"
        {
            tolerance 1e-4;
            relTol 0;
        }

        "(k|omega)"
        {
            tolerance 1e-4;
            relTol 0;
        }
    }
}
```

6.5 Initial and Boundary Conditions

The initial and boundary conditions are specified in each variable file of the 0 directory. For each of them, three entrees need to be set: the `dimension`, the `internalField` and the `boundaryField`.

The `dimension` entree will be specified every time a quantity is considered. Let us focus, instead, on the `internalField`, which represents – for each variable – the value for the internal computational grid points to be set at the initial time of the simulation.

The `internalField` for pressure is then set to 0 and for velocity to `uniform` (14.2 0 0). The initial condition on the turbulent kinetic energy k is given by:

$$k = \frac{3}{2}(UI)^2 \tag{6.5}$$

where I is the *turbulence intensity* and U is the flow velocity, which corresponds to v_0 at the initial time. From [7], it can be read that experiments were performed in the wind tunnel at a level of turbulence that was lower than 1%. For external aerodynamics cases, this information is sufficient to suggest using value $I = 0.005$ in OpenFOAM®. Thus the initial `internalField` for k is set to:

$$k = \frac{3}{2}\left(14.2 \cdot 0.005\right)^2 = 0.0075615 \text{ m}^2/\text{s}^2 \tag{6.6}$$

The initial value for the specific dissipation rate ω is set to:

$$\omega = C_\mu^{-1/4}\frac{\sqrt{k}}{l} = 3.0240 \text{ s}^{-1} \tag{6.7}$$

In this formula, $C_\mu = 0.09$, k is the value computed in Eq. (6.6) and $l = 0.07L$ with L characteristic length (for this case, the mid-span length has been considered).

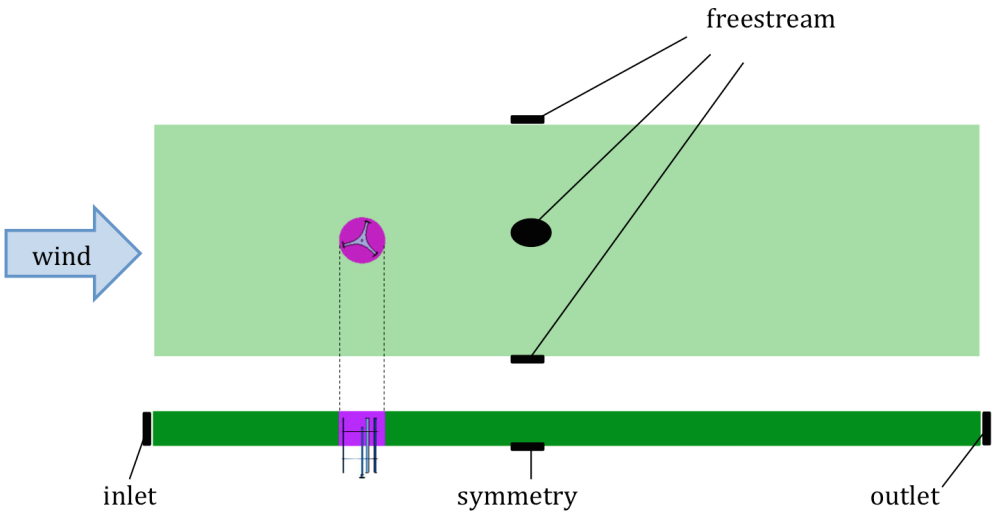

Figure 6.1: Boundary Conditions: Fixed Domain

Let us now focus on the boundary conditions with reference to Fig. (6.1). At the *inlet* section, the condition on pressure is `zeroGradient`:

$$\frac{\partial p}{\partial n} = 0 \tag{6.8}$$

while U condition is `fixedValue, uniform` (14.2 0 0), since the flow crosses the inlet section at velocity:

$$v_0 = 14.2 \text{ m/s} \tag{6.9}$$

in its normal direction.

The condition on k is `turbulentIntensityKineticEnergyInlet` with value $I = 0.5\%$, as explained above, while condition on ω has been set to

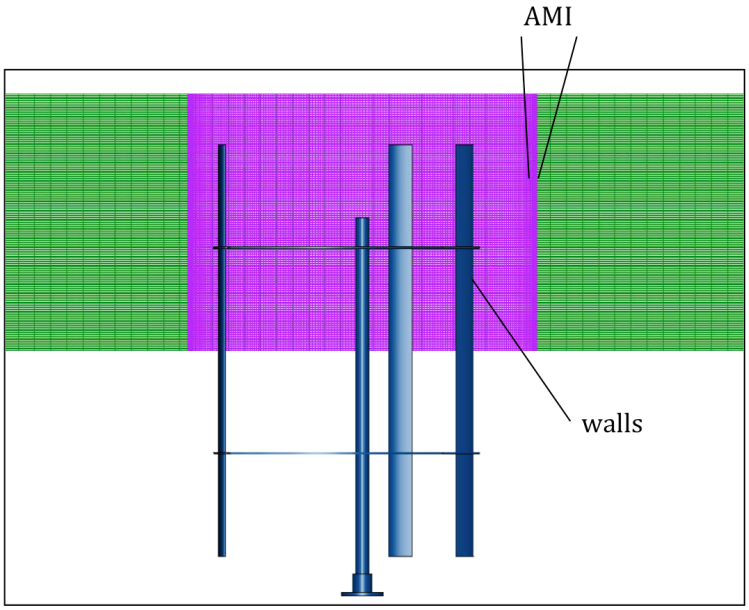

Figure 6.2: Boundary Conditions: Moving Domain

`turbulentMixingLengthFrequencyInlet` with $l = 0.1$.

By focusing on the outlet section, pressure condition is set to `fixedValue`, `uniform` 0, U and k to `zeroGradient` and ω to the `inletOutlet` boundary condition:

$$p = 0 \tag{6.10}$$

$$\frac{\partial U}{\partial n} \tag{6.11}$$

$$\frac{\partial k}{\partial n} \tag{6.12}$$

$$\frac{\partial \omega}{\partial n} \tag{6.13}$$

In the end, a `symmetryPlane` condition has been clearly used for the domain lower surface, while the conditions for the remaining external boundaries (i.e. the upper surfaces and the lateral sides) have been set to `freestream`, in order to reproduce the non-confined environment for the air stream.

With reference to Fig. (6.2), on the AMI patches the `cyclicAMI` boundary condition has been imposed to couple the static and the rotating meshes, as discussed in Ch. (5).

Walls, instead, are required to fulfill the no-slip condition, which means:

$$\frac{\partial k}{\partial n} = 0 \tag{6.14}$$

for the turbulent kinetic energy, and opportune laws of the walls for ω and ν_T.

Chapter 7

Results

The presented project is an ongoing work. Indeed, many factors contributed to make this case-study very complex: the external-aerodynamic problem-type, the complex flow aerodynamics, the decision to reproduce a non-confined environment, the huge number of grid cells involved as a consequence, the challenging operating point chosen to study the turbine behavior, the airfoil-based shape of the machine, the implementation of a new turbulence model.

The consequence has been a huge computational time required for the simulation, which – let us say – is the price paid for a higher accuracy in the results. Therefore, this chapter will show the preliminary results of the simulation only, which correspond to the transient state of the simulated time range.

It must be said, however, that despite the solution is still approaching full convergence, these results are definitely interesting as they clearly prove the correctness of the set-up (e.g. the validity of the AMI strategy for mesh-movement) and the suitability of the DLRM as turbulence model for this and similar cases. Moreover, they already allow inferring useful information on the fluid behavior, to the extent that a comparison with experimental results from Dossena *et al.* [7] can already be sketched out.

7.1 Pressure and Velocity Fields on Symmetry Plane

The case-study is about the behavior of a subsonic flow, which implies that the upstream velocity and pressure fields continuously rearrange as a function of the time-dependent downstream aerodynamics. If the downstream region strictly affects the upstream, then at least the steady-state solution should be awaited to infer general conclusions on the whole domain.

However, this consideration is not in disagreement with the possibility of capturing some time-specified states. In other words, even during the transient state, the simulation allows considering an instantaneous snapshot of the flow pressure and velocity fields as truthful, on condition that of course those results are just referred to the time step considered.

That having been said, for the case under investigation, even the instantaneous descriptions of the flow properties during the transient state seem to be on the right track for convergence, as at that time steps the flow behavior definitely approaches the one physically expected.

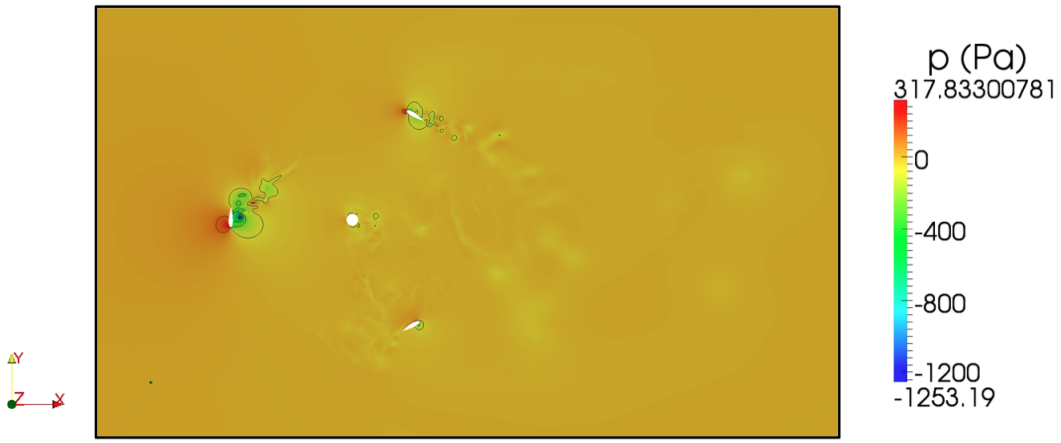

Figure 7.1: Pressure field on symmetry plane at t = 0.094342 s

Fig. (7.1) and (7.2) show the pressure field on the symmetry horizontal plane at time t = 0.094342 s. The values for p shown by the legend are scaled with respect to the cells with value 0, i.e. p is a relative pressure and this accounts for possible negative values. Indeed, when dealing with incompressible flows, no density appears in the momentum equation and, in simulations, the relevant information becomes the pressure gradients (and no more the absolute value of pressure).

These plots especially highlight how pressure distributes when the flow impacts each blade at different angles of attack. As it can be noticed, the second detail picture from the top in Fig. (7.2) provides the most critical situation, in which the flow impacts the blade at its suction side. On the one hand, this condition is crucial from the aerodynamics point of view, as the kinetic-to-mechanical energy conversion is not efficient and energy is mostly dissipated. On the other hand, this condition is also critical from the nu-

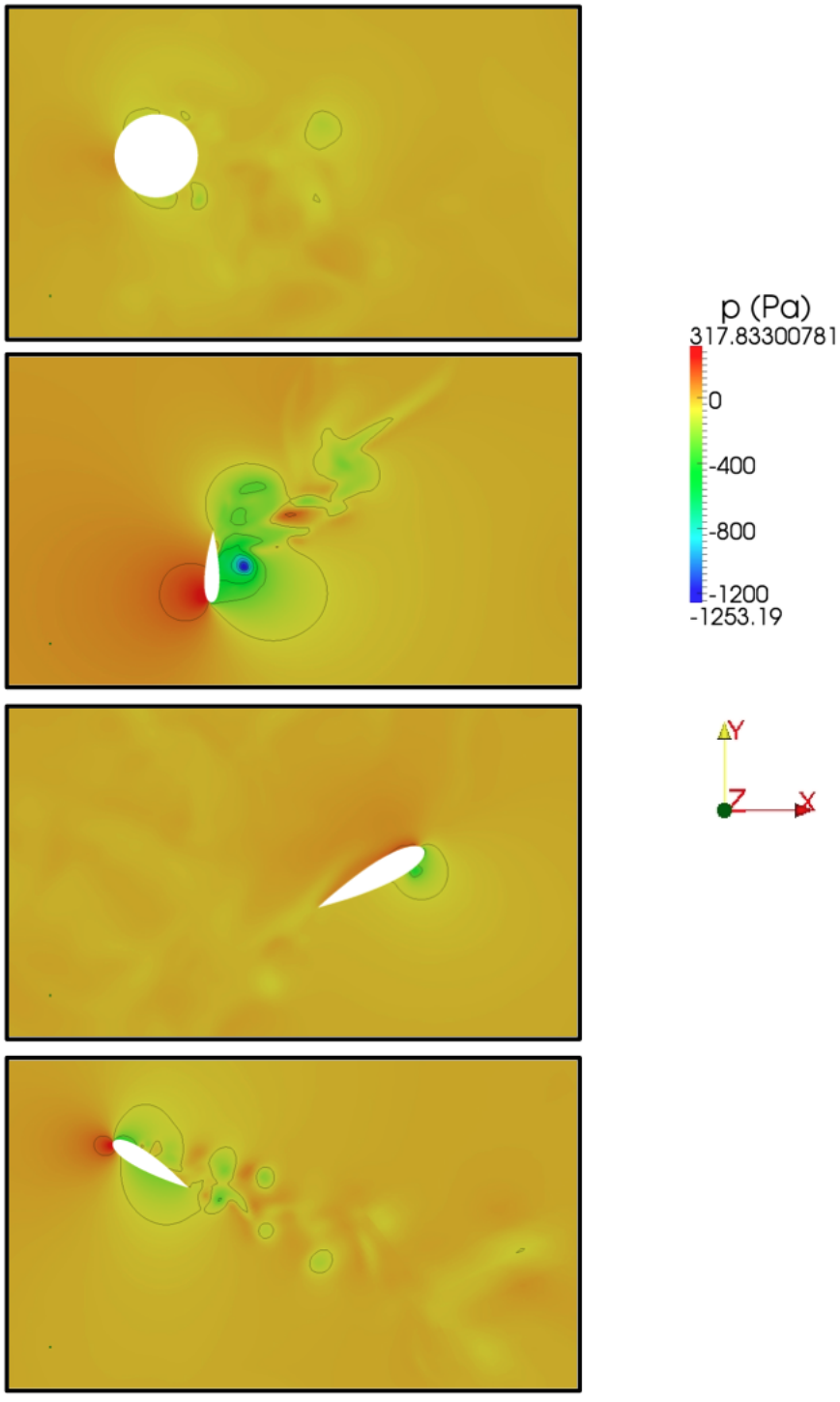

Figure 7.2: Details of pressure field on symmetry plane at t = 0.094342 s

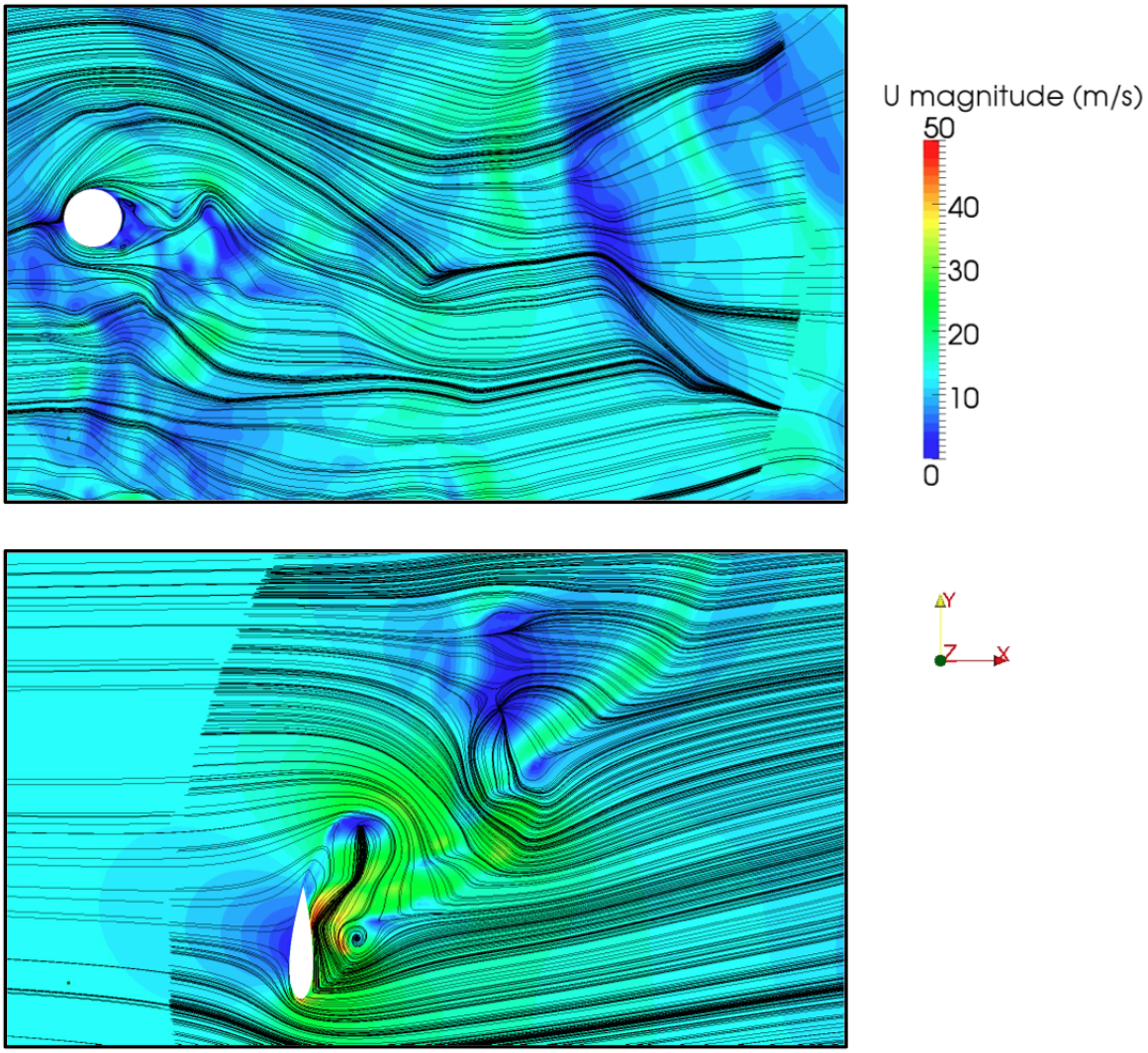

Figure 7.3: Details of velocity field on symmetry plane at t = 0.094342 s

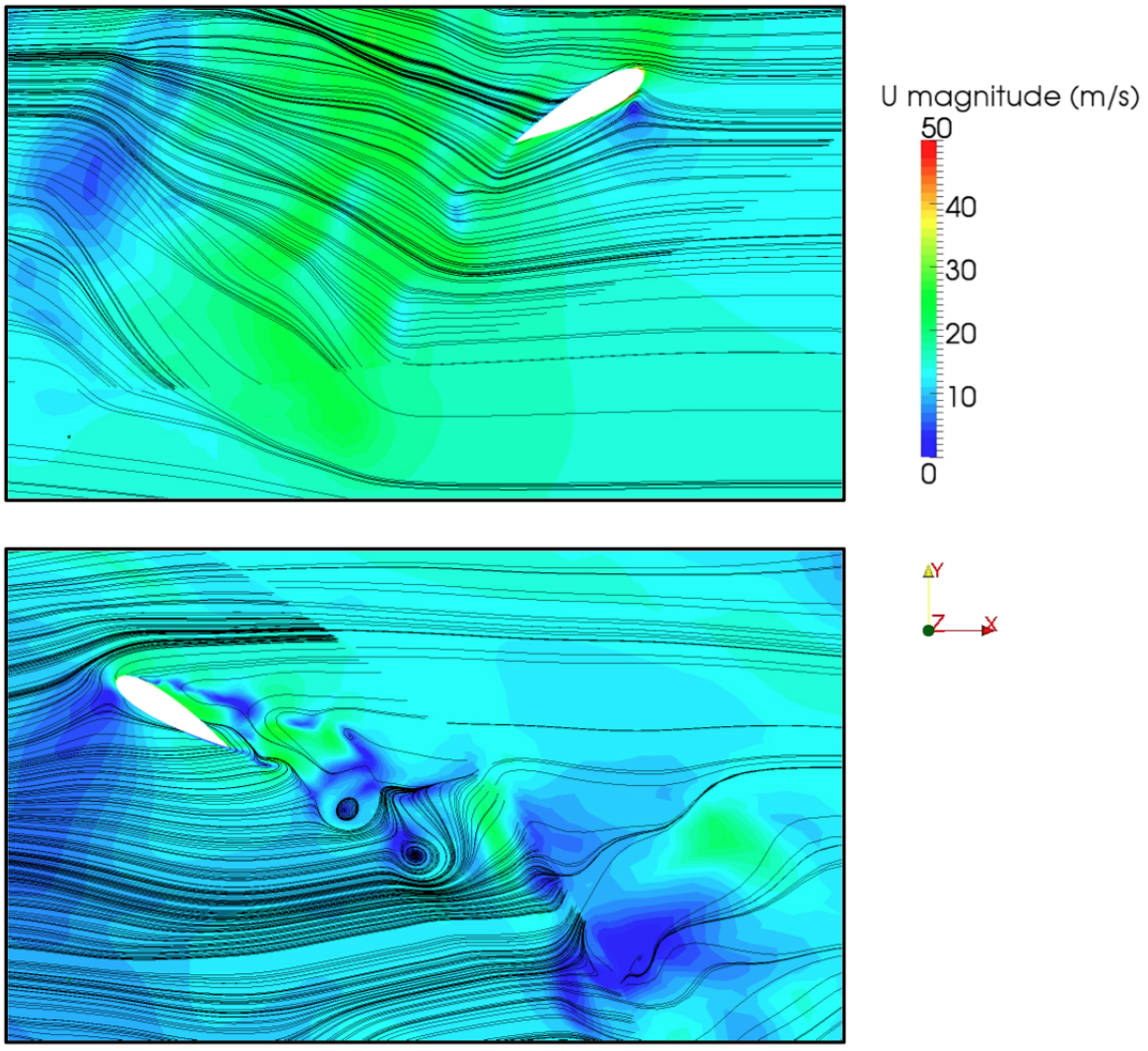

Figure 7.4: Details of velocity field on symmetry plane at t = 0.094342 s

merical point of view. In fact, the flow approaches the blade almost aligned with the axial direction and, in doing so, it impacts the longest sides of the boundary layer cells, which – as formerly discussed in Ch. (5) – are very stretched along the airfoil profile to give a good near-wall mesh refinement.

Despite this might cause numerical issues, no particular concern arises from the case under investigation. In fact, the results are close to the expected ones. This point (which is evident also in the other plots of both pressure and velocity) is a valid proof of the mesh high quality.

Fig. (7.3) and (7.4), instead, show some details from the velocity field results, on the same plane and at the same time step. The vortex production is evident at the blade walls and is further highlighted by the streamlines in the plots. Also, downstream of the axis, a first development for a *Kármán vortex street* can be noticed, which consists in a periodical pattern of swirling vortices, generated by alternating fluid separation from the two sides of the axis.

Similar results have been found for time t = 0.115077 s and are shown by Fig. (7.5) to (7.9). These plots show the further development of the flow, thus confirming the descriptions just provided.

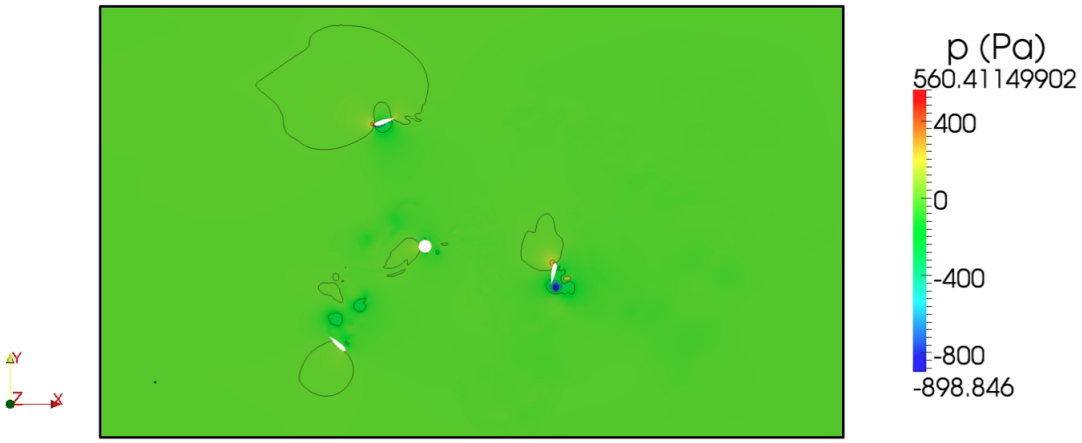

Figure 7.5: Pressure field on symmetry plane at t = 0.115077 s

7.2 Turbine Operation Overview

The case under investigation represents a low-load condition, since a tip-speed ratio $\lambda = 1.5$ has been chosen. At this point of the simulation, it is

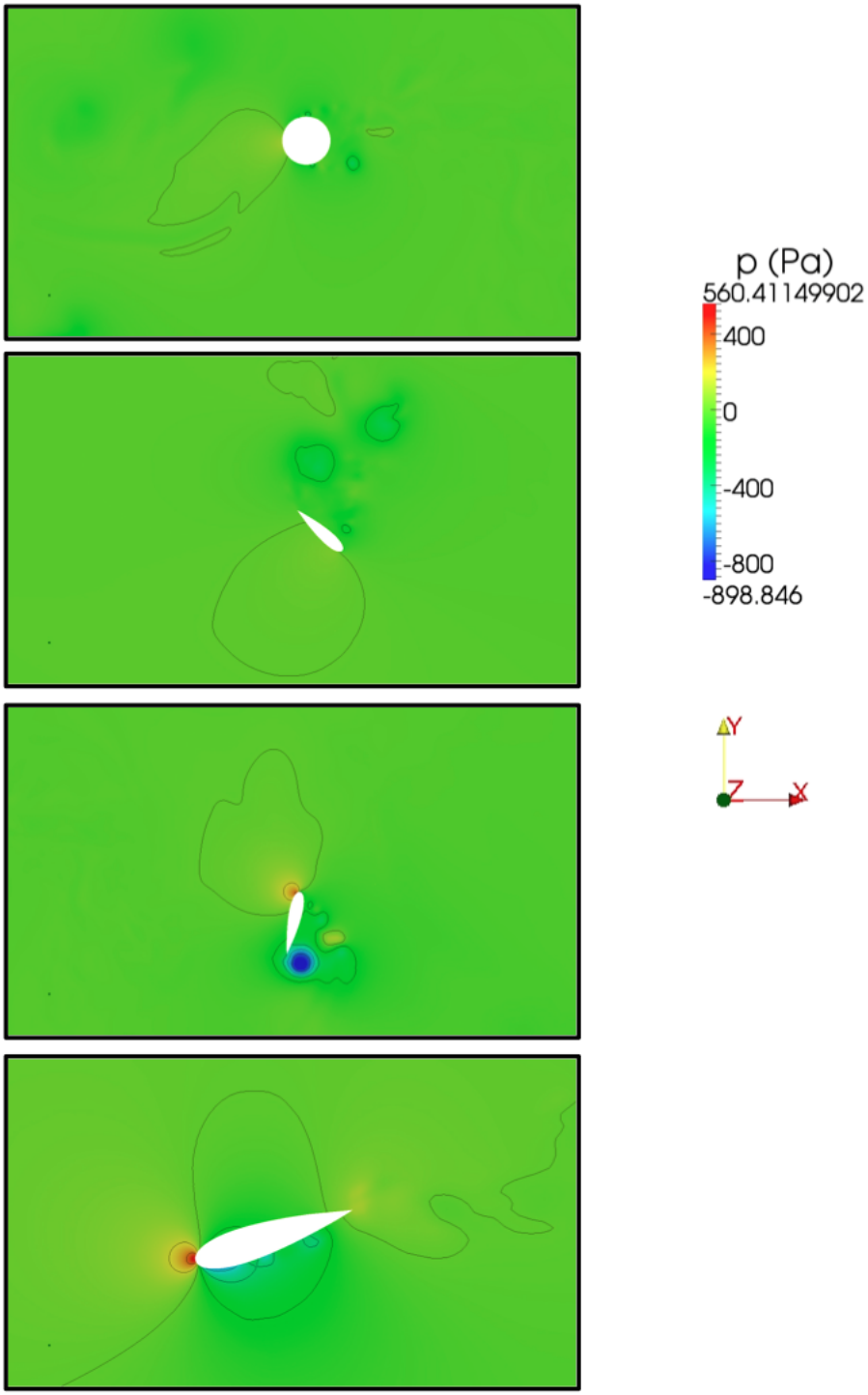

Figure 7.6: Details of pressure field on symmetry plane at t = 0.115077 s

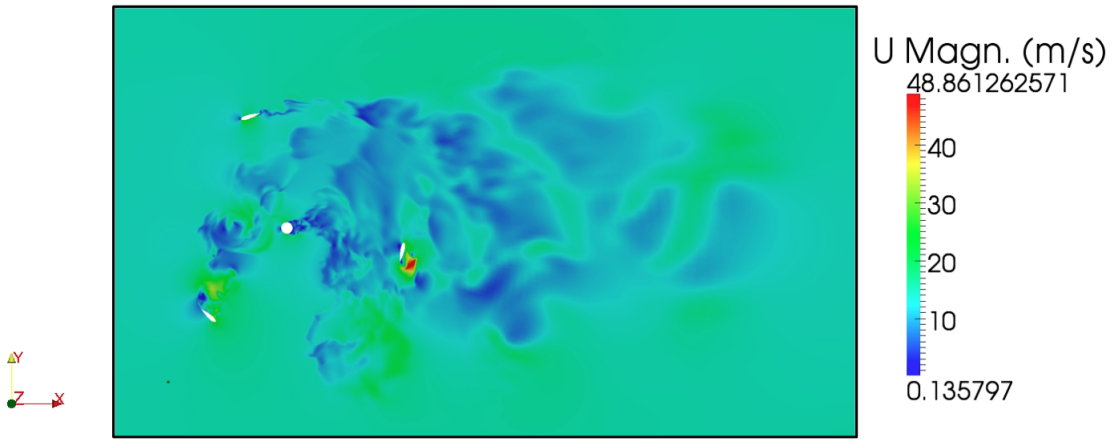

Figure 7.7: Velocity field on symmetry plane at t = 0.115077 s

untimely to infer reliable values for the coefficient of power, which should be computed by time-averaging the results only once the simulation has reached a steady state condition. Therefore, no conclusion is possible, even though, – already from the transient state – the value for C_p seems to position on the growing-trend portion of Fig. (4.9), as the experiments have evidenced.

However, the aspect that is worth being mentioned is the tendency of the flow to exhibit the same exact behavior (already in the non-steady condition) that has been highlighted by the experimental tests for a low value of C_p. Indeed, the flow shows a high tendency to stall as well as a marked non-symmetrical wake on the planes whose normal vector is aligned with the axial direction. This situation is crucial, since the variation of the flow angle of attack (evaluated at the blade leading edge) can increase to the extent that the fluid detaches during most of the turbine revolution.

These are the features on which this case distinguishes from higher-λ conditions, together with the accentuated periodical trend of the turbulent wake. The results for the vertical planes will be shown and discussed in the next section. Here, instead, it is important to give an overview of the turbine operation and, specifically, to distinguish two different regions as a consequence of its interaction with the wind.

A top view of the turbine is provided by Fig. (7.10). When the blades perform a complete revolution, the interaction with the wind can be roughly split in two phases: a *downwind* phase ($0 < Y/D < 0.5$) and an *upwind*

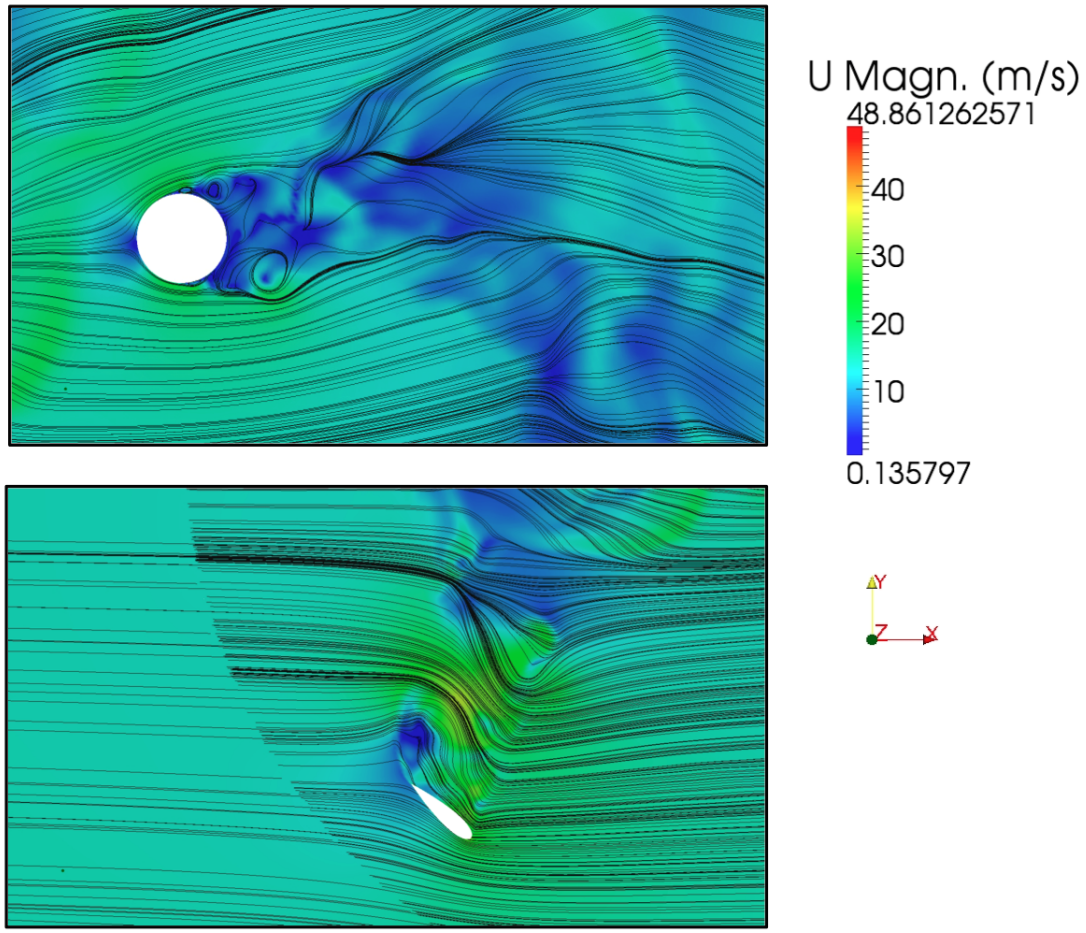

Figure 7.8: Details of velocity field on symmetry plane at t = 0.115077 s

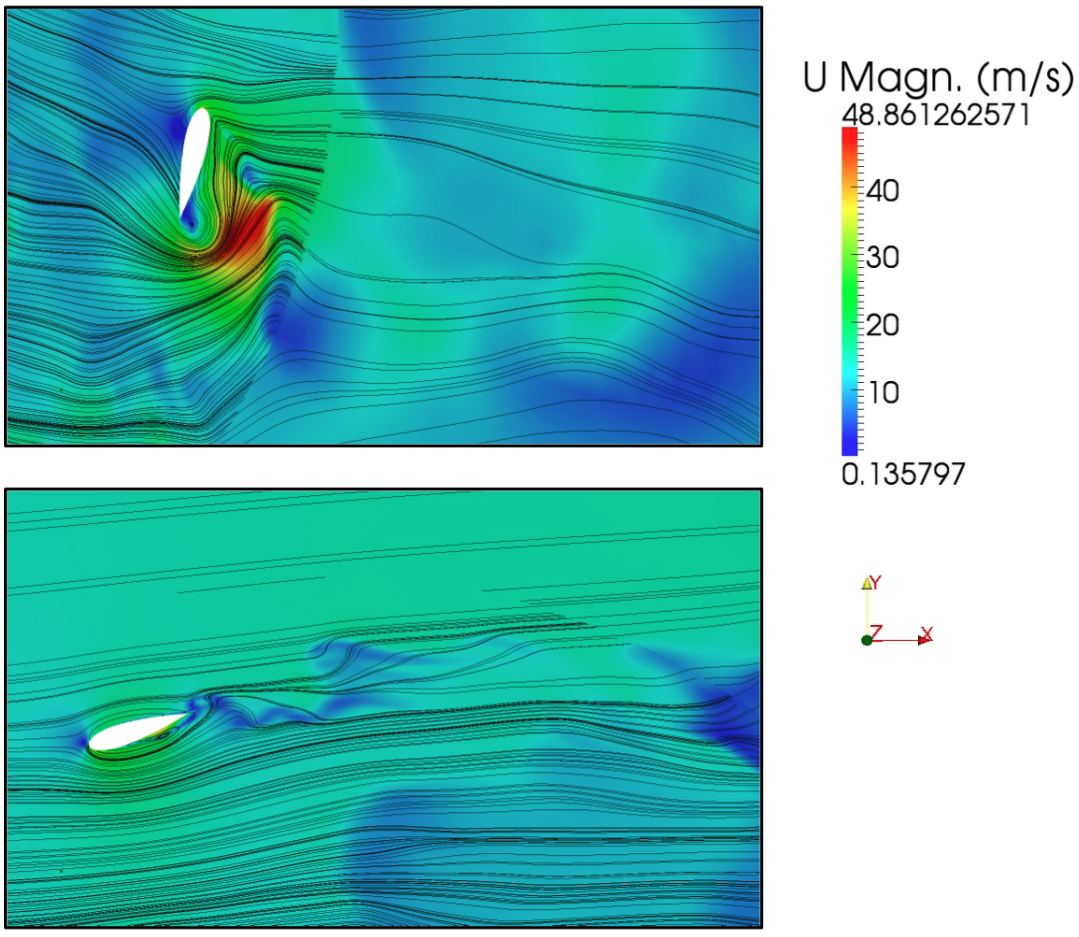

Figure 7.9: Details of velocity field on symmetry plane at t = 0.115077 s

phase ($-0.5 < Y/D < 0$). Of course, the discriminating factor is the relative position of the blades with respect to the direction of the far undisturbed air stream.

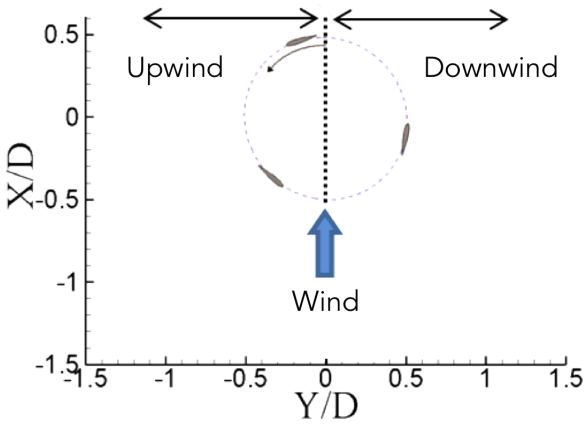

Figure 7.10: Schematics of turbine operation

As will be shown in the next section, the *downwind* phase is always the most critical one, especially for what concerns the issue of fluid stall. The difference in the angle of attack, whether the blades are crossing one region or the other, is also at the basis of the non-symmetric turbulence that generates at the blade tips, which has turned out to be evident from the very beginning of the simulation.

7.3 Pressure and Velocity Fields on Vertical Sections *Far* and *Near*

Fig. (7.12) and (7.13) show the velocity and pressure fields on both sections *near* and *far* referred to the simulation time-step t = 0.115077 s. Also for this case, a thorough analysis of these property fields should be carried out by running the simulations for a number of revolutions after the steady-state condition has been achieved.

Indeed, a good manner of handling the available information from the simulation would be to collect data on both velocity and pressure fields at corresponding positions of the turbine for each revolution. Actually, data can be sampled three times per revolution instead of one, due to the three-axial symmetry of the turbine and consequently of the physical problem. For instance, both the velocity- and pressure-field data can be sampled on

the measurement planes every time any of the three blades passes through a specified position. These data should eventually be averaged to obtain a mean field with respect to time.

This procedure would lead to plots that are expected to be similar to the ones derived by time-averaging experimental results, which are shown by Fig. (7.11).

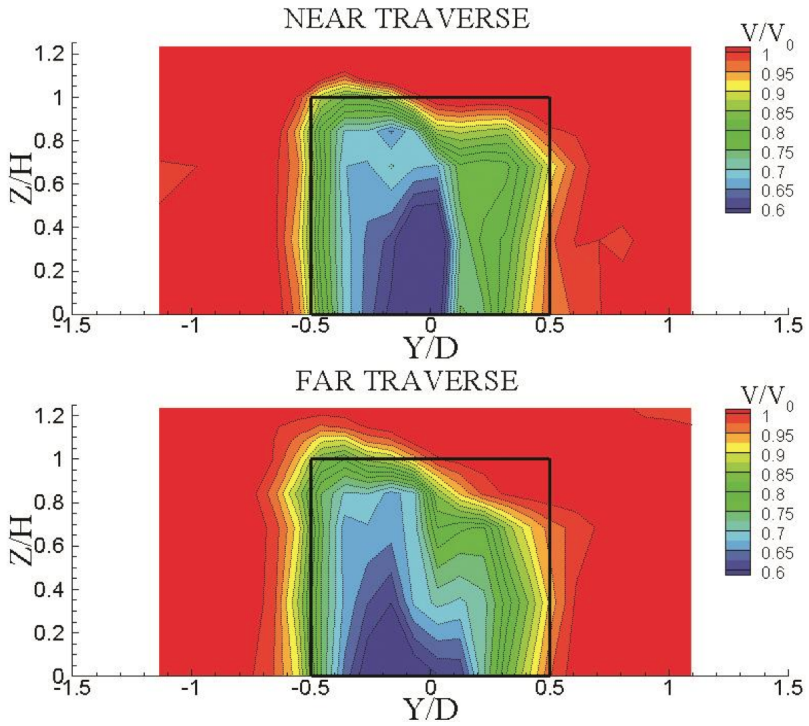

Figure 7.11: Time-averaged velocity field on sections *near* (top) and *far* (bottom) from experimental tests.

Back to the results for the case under investigation, it is important to specify that Fig. (7.11) and (7.12) cannot be directly compared, since – as mentioned – the plot from the simulation results is an instantaneous snapshot of the velocity field and the picture from experimental tests is the result of a time-averaging procedure of this property.

Nevertheless, once this point has been clarified, it can be actually noticed that the two representations share some clear common features. First of all, for the chosen tip-speed ratio, the wake is not symmetric and it mainly develops in the upwind-phase region.

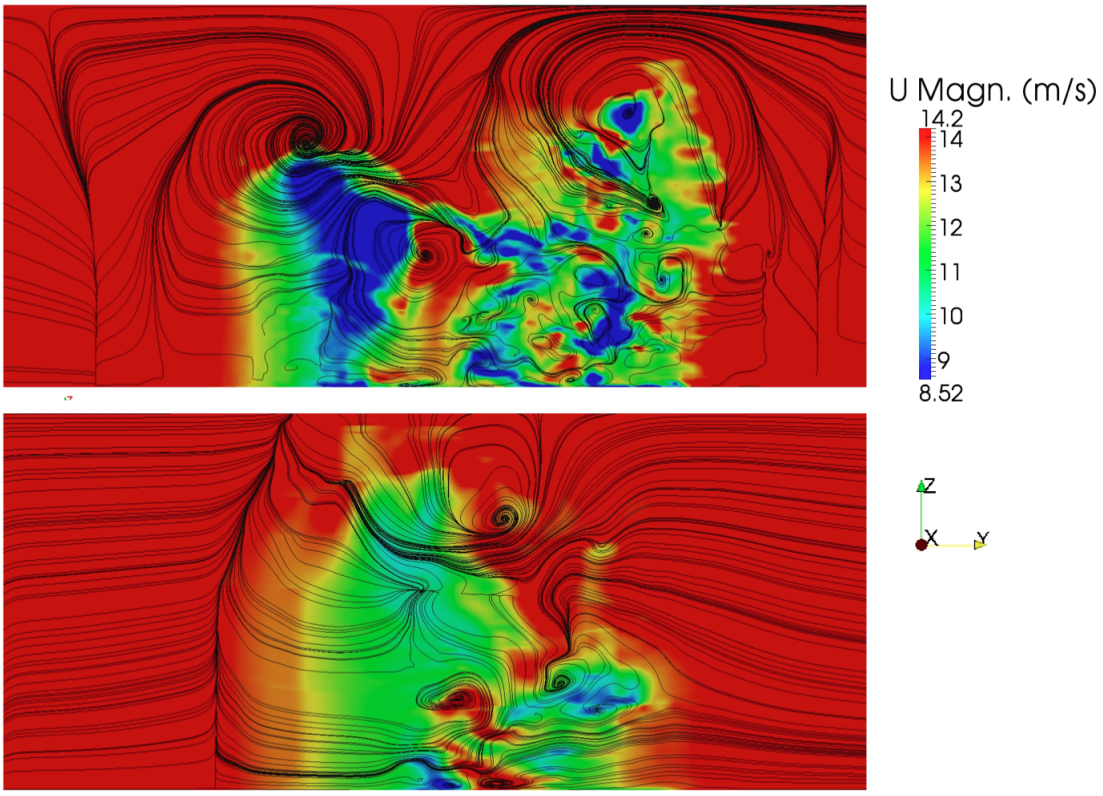

Figure 7.12: Velocity field on sections *near* (top) and *far* (bottom) at t=0.115077 s

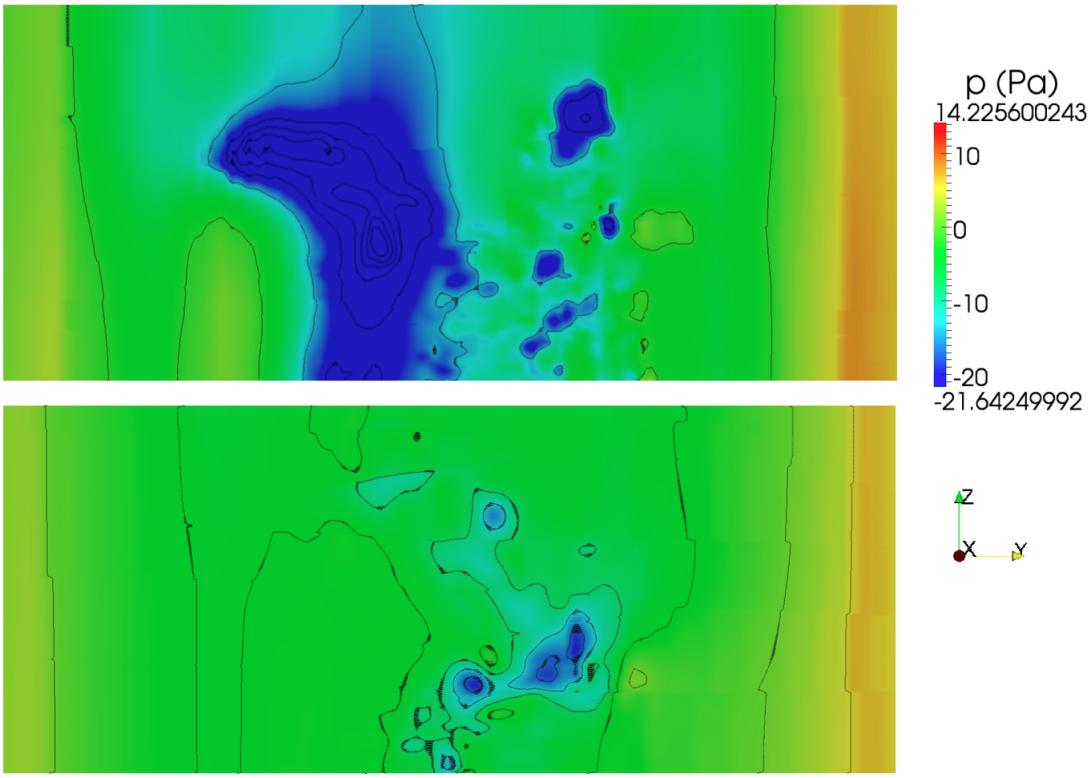

Figure 7.13: Pressure field on sections *near* (top) and *far* (bottom) at t=0.115077 s

It might be supposed that this is trivially due to the fact that for $-0.5 < Y/D < 0.0$ the blades rotate *against* the wind, while for $0.0 < Y/D < 0.5$ the wind blows in the same direction of the blades. Actually, this explanation is incomplete. Indeed, also for higher tip-speed ratios, the downwind-phase region is more critical and responsible for higher aerodynamic forces, but the wake definitely appears to approach a symmetric shape.

To be more precise, it is true that the wake is always non symmetric and the consideration above accounts for this fact. However, how much this non-symmetry is pronounced is what really makes the difference.

Therefore, the reason is to be found in the higher possibility – for small tip-speed ratios – of a dynamic stall. If the fluid is more likely to detach, there will be a high vortex generation at the blade tips during the downwind phase of the revolution, which in turn, will accentuate the non-symmetry in the shape of the wake firstly produced for the changes in the blade angle of attack. On contrary, during the upwind phase, as blades move against the wind, a higher lift establishes on the blades and stall is usually limited or inhibited.

To recap, since the impact between the blades and the wind occurs in both the upwind- and downwind-phase regions, for any λ condition, the wake exhibits a double peak. Moreover, in all the situations, the two peaks differ in their intensity as a consequence of the change in the blade-wind relative position, which in turn is responsible for different aerodynamic forces in the two regions. Precisely, the turbine rotation is responsible for a non-evenly distributed lift, which is stable in the central part of the turbine and unbalanced on the two sides. In fact, in the downwind-phase region, this force component is normally weaker.

Given that all conditions show a non-symmetric wake for this reason, the relevant feature is, however, that the two peaks of the wake especially differ for the case under investigation. Indeed, a significant detachment of the flow occurs at the downwind-phase region of the turbine and involves most of the machine revolution.

Specifically, in this case, stall is responsible for a non-symmetric shape that involves almost the whole vertical extension of the wake, while for higher tip-speed ratios only the tip region is involved. By being the distinctive factor with respect to other flow conditions, this characteristic then further proves the similarity between Fig. (7.11) and (7.12). Moreover, it can be noticed that, in both the two couples of figures provided, this non-symmetry becomes more evident as the wake extends downstream of the turbine. Thus, another common characteristic is given by a similar flow

behavior when switching from the *near* section to the *far* section.

Similar considerations on the non-symmetric shape of the wake can be inferred by plotting (on the same measurement planes) the *yaw angle*. This parameter measures the deflection of the fluid at each cell and is defined as:

$$\theta_{yaw} = \arctan \frac{U_y}{U_x} \tag{7.1}$$

The results for the case-study on hand are provided by Fig. (7.15). A comparison with the results from the experimental tests is also provided, but the same criteria for interpretation – as the ones specified above for the velocity field – hold, i.e. a time-averaged plot should not be confused with an instantaneous snapshot.

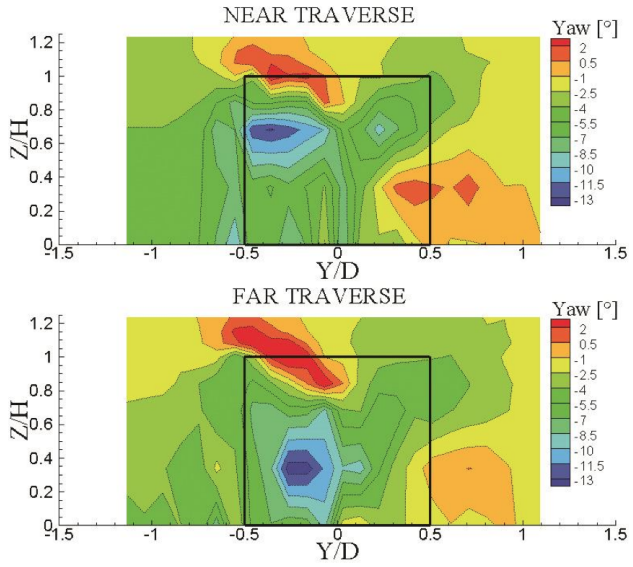

Figure 7.14: Time-averaged yaw angle on sections *near* (top) and *far* (bottom) from experimental tests.

The pictures show a very good agreement between the results on the *near* section and just a rough comparison can be made for the *far* plane. This is not a a contradictory result, and actually it is surprising that the *near*-section yaw angles are so similar to each other, as a time-averaged plot on a number of revolutions at a steady state condition is being compared to an instantaneous plot.

Indeed, it can be inferred that the flow almost starts deflecting to the final yaw angle at the very beginning of the motion in the regions that are

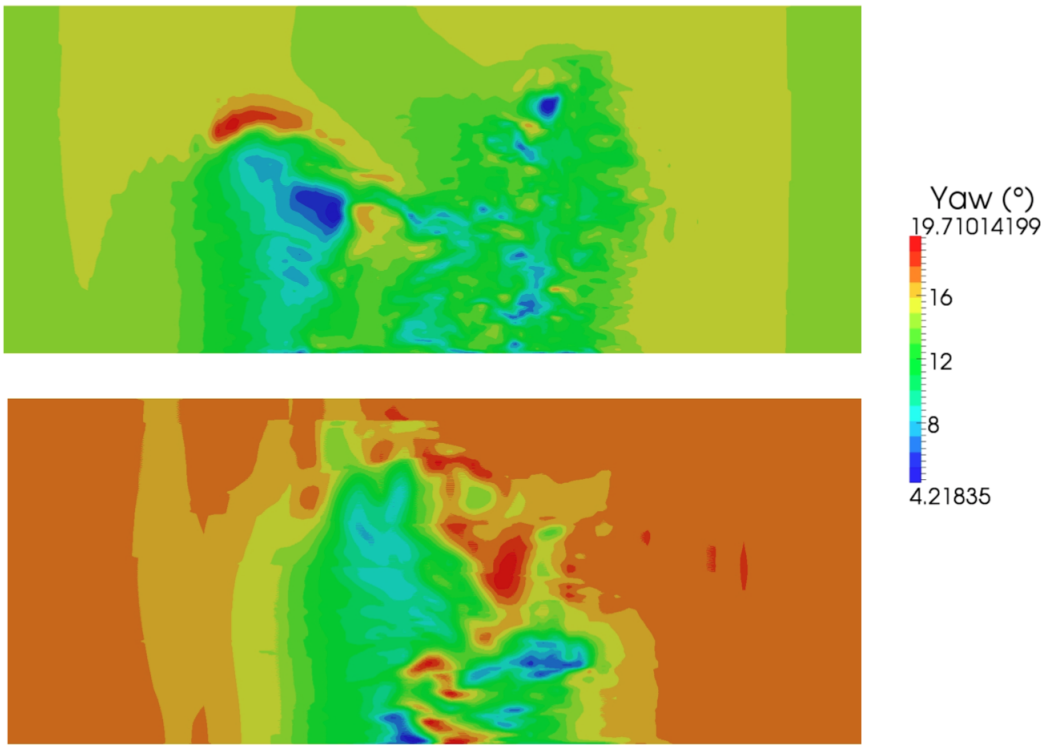

Figure 7.15: Yaw angle on sections *near* (top) and *far* (bottom) at t=0.115077 s

closer to the machine. This is also another validation of the simulation being run. On the other hand, the results on the *far* section can be justified by supposing that the wake still needs time to propagate and stabilize downstream.

7.4 Blade-Transit Frequency and Vortex-Detachment Frequency

The three-axial symmetry of the turbine involves a cyclic fluctuation of the main aerodynamic forces (if referred to the whole machine) with a period that equals 1/3 of the rotor period of revolution.

Fig. (7.16) and (7.17) show the coefficients of lift and drag, computed for the three blades separately and collected in a sigle graph for each parameter. It can be noticed that the coefficients for each blade do have the same frequency of the rotor revolution, if considered separately. Throughout each period they have a growing trend in their amplitudes for half of the revolution and a decreasing trend for the other half. This has been already discussed in the previous section, when explaining why, for instance, the lift force is not evenly balanced in the two regions highlighted.

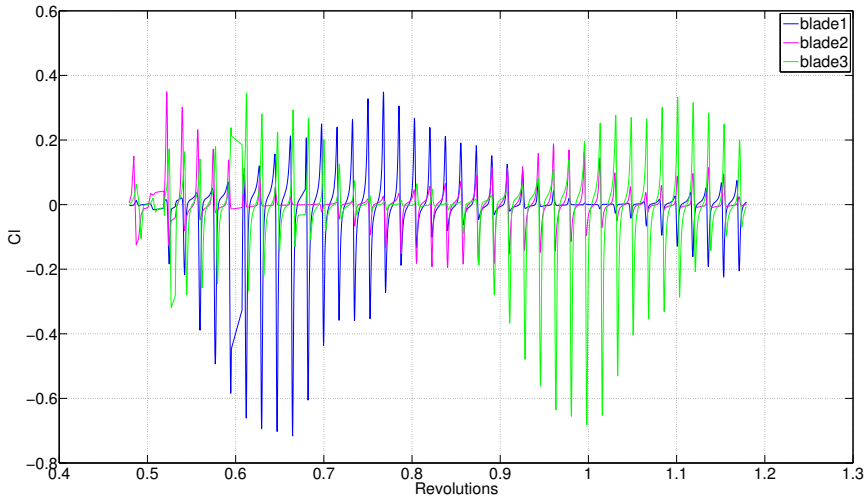

Figure 7.16: Trend of the coefficient of lift for the three blades.

A relevant aspect of these plots is actually that there is a higher-frequency fluctuation overlapping the lower-frequency one already discussed. Thus, starting from these figures, an explanation has been demanded. Indeed, a possible interpretation relates the overlapping fluctuations to the periodic

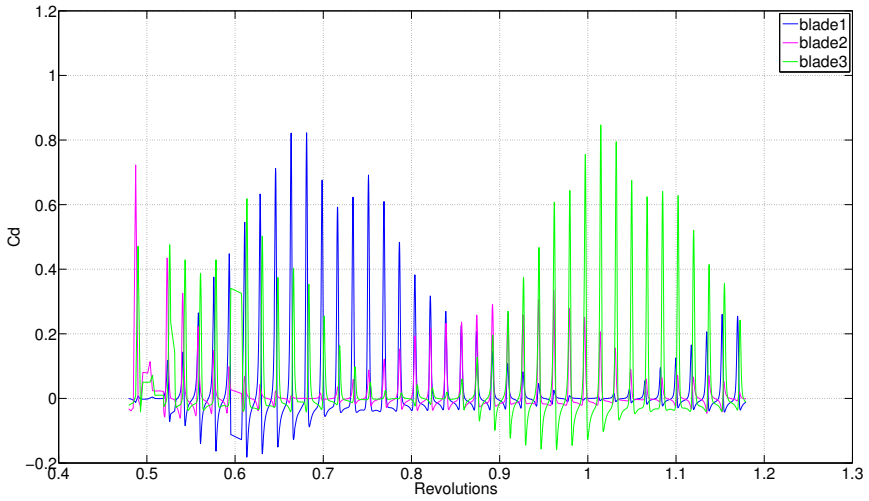

Figure 7.17: Trend of the coefficient of drag for the three blades.

unsteadiness of the flow in the regions closest to the blade wall. In other words, this is the frequency at which vortices detach from the blades.

Let us focus on the coefficient of drag of one single blade. Fig. (7.18) shows the trend for C_D referring to blade 1. Moreover, let us pinpoint two different values, which fulfill the requirement of being subsequent extremum values of the curve. To this purpose, t=0.03923 s and t=0.04135 s have been selected, which respectively correspond to $C_D = -0.04378$ and $C_D = 0.59324$.

Fig. (7.19) and (7.20) compare the flow condition at the two selected times, respectively in terms of pressure computed the walls of blade 1 and of velocity around this latter. Both the comparisons clearly highlight the significant differences among the two situations.

Specifically, pressure is definitely higher at t=0.03923 s in the proximity of the trailing edge (where vortices are generated) and undergoes a sudden reduction at t=0.04135 s. The pressure rise and sudden drop can be explained with vortex generation and eventual flow detachment. This is, indeed, confirmed by the velocity field computed on the symmetry plane portion about the blade. The arrows, whose length is scaled with respect to the velocity value, clearly allow identifying a vortex, which generates in the proximity of the blade and then propagates downstream.

To conclude, it seems reasonable to infer that the high-frequency fluctu-

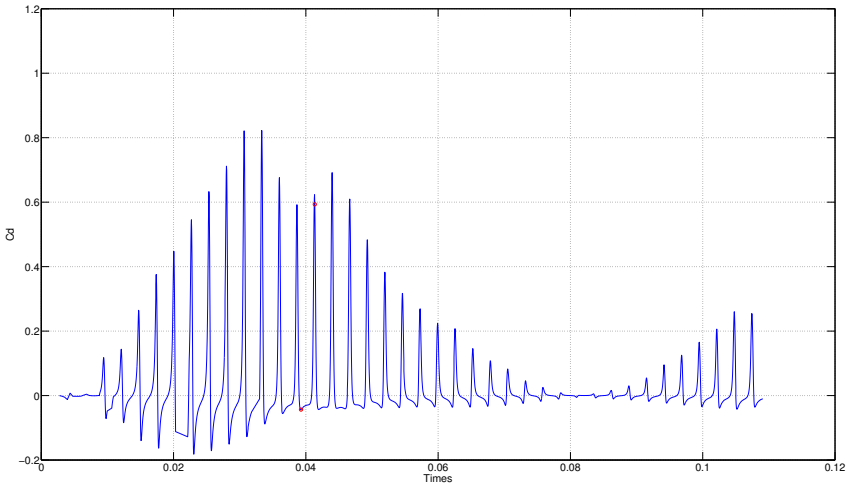

Figure 7.18: Trend of the coefficient of drag for blade 1. Times t=0.03923 s and t=0.04135 s are highlighted.

ations evidenced in Fig. (7.17) are related to the vortex unsteadiness in the proximity of the blade walls.

7.5 DLRM validation

As already mentioned, the case under investigation has also represented a test-case for validating the new turbulence model. Indeed, DLRM, whose description has been provided in Ch. (3), has been applied to an external aerodynamic case for the very first time.

DLRM has turned out to be very performing for the case on hand. The first aspect that deserves to be mentioned is that the pressure and velocity fields smoothly vary throughout the whole computational domain and no sudden variations occur when crossing the Arbitrary Mesh Interfaces used for matching the moving and still sub-domains.

Fig. (7.21) shows the velocity field on the symmetry plane at t=0.115077 s. The AMI patches are highlighted, but no sudden jump in the fluid properties is visible.

Secondly, it turns out that this model is able to capture the time-dependent unsteadiness of the flow very accurately. In particular, the vortex structures are especially captured in those regions of the computational domain where the mesh refinement is higher.

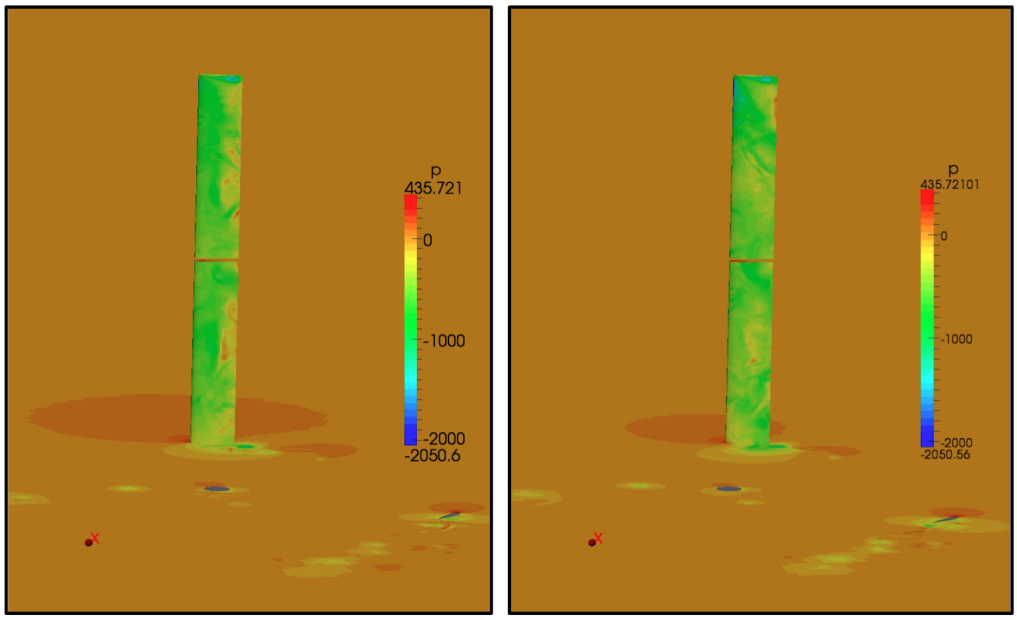

Figure 7.19: Pressure on blade 1 at t=0.03923 s (left) and t=0.04135s (right)

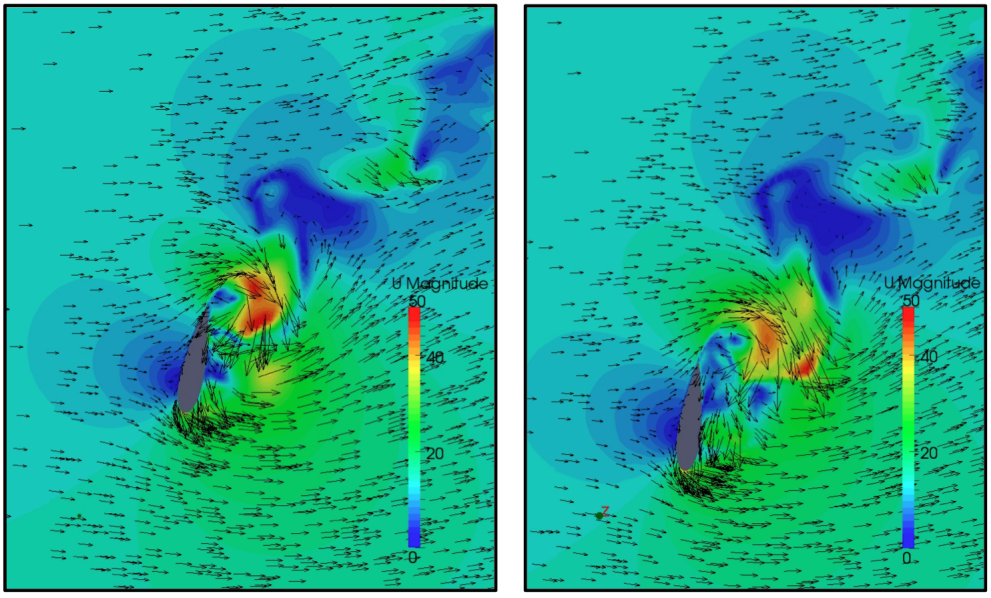

Figure 7.20: Velocity around blade 1 at t=0.03923 s (left) and t=0.04135s (right).

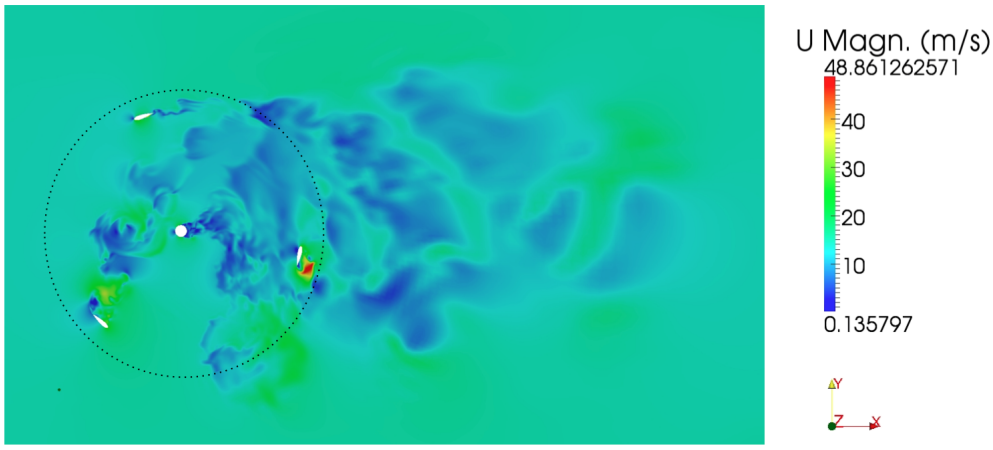

Figure 7.21: Velocity field on the symmetry plane at t=0.115077 s. The Arbitrary Mesh Interfaces (AMI) are highlighted

Indeed, this is clearly related to the higher possibility that the model switches to LES if the mesh size is smaller. Nevertheless, an overall general high accuracy can be evidenced throughout the whole domain.

By comparing the results for the case under investigation to the results of a similar simulation performed on the same case-study but based on a standard $k-\omega$ SST model, these conclusions become evident. Specifically, Fig. (7.22) and Fig. (7.23) show the comparison between the two models on the velocity field. Vortex structures are evidenced by means of streamlines.

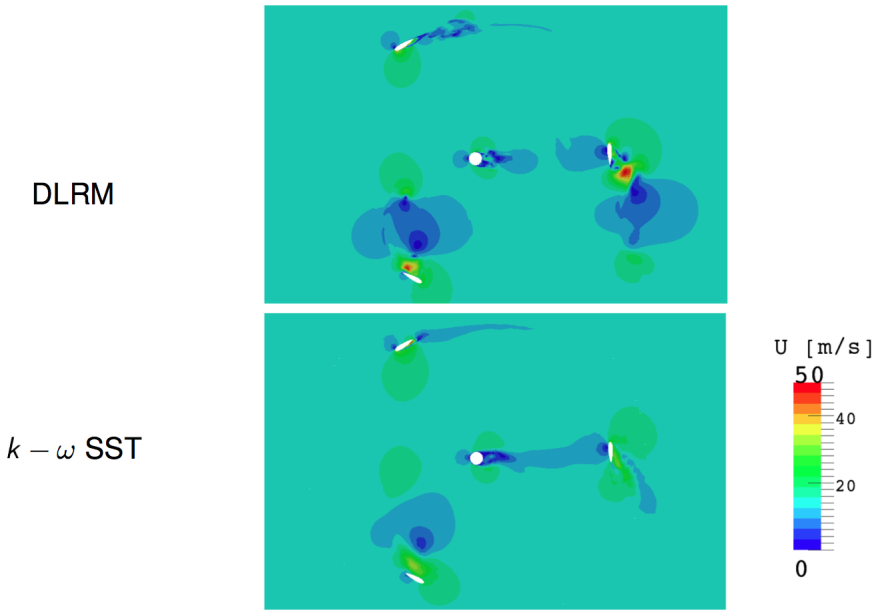

Figure 7.22: Comparison between DLRM and $k-\omega$ SST on the velocity field.

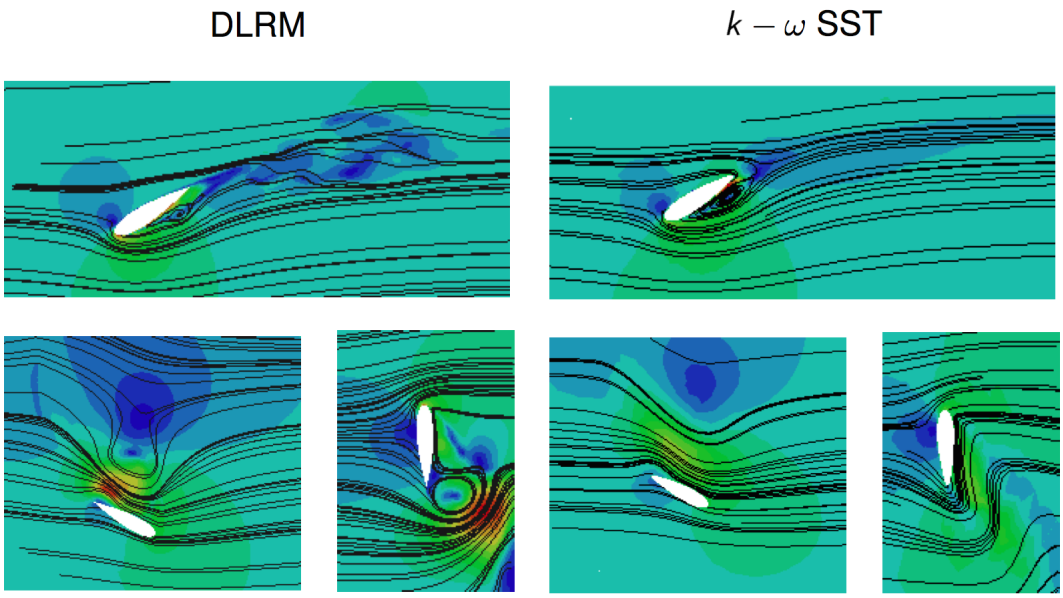

Figure 7.23: Comparison between DLRM and $k-\omega$ SST on the velocity field. Vortex structures are highlighted by streamlines.

Chapter 8

Conclusions and Further Work

The aim of this thesis was to investigate the flow field around a H-type Darrieus vertical-axis wind turbine. At the same time, this work presented an external-aerodynamics test-case for DLRM. This turbulence model operates in URANS or ILES mode, depending on the comparison of the modeled scales to what can potentially be resolved by the computational grid and time-step. The flow is fully turbulent and the machine operation is characterized by a tip-speed ratio $\lambda = 1.5$, which corresponds to a low-load condition.

The project represents an ongoing work. Indeed, the high quality of the computational grid and its spatial extension (≈ 45 M cells), which has been necessary in order to reproduce a non-confined environment for the airstream, involved a very high computational time required by the simulation and the solution still needs to fully converge.

Nevertheless, the analysis of the results on the transient regime was carried out and a good consistency with the expected outputs was observed. Instantaneous descriptions of the flow velocity and pressure fields, at different times of the simulation, revealed a good agreement with the available results from experimental tests. Specifically, a full comparison was not possible, since instantaneous plots of the fluid properties cannot be directly compared to time-averaged measurements. The results, indeed, should be averaged as well, which is possible only once the solution fully converges. However, many common features between the two sets of results could certainly be identified, and they revealed relevant aspects of the fluid behavior.

The pressure and velocity fields computed on the horizontal symmetry plane provided a very accurate description of the flow. Specifically, the anal-

ysis illustrated how these properties vary in the proximity of the blade walls as a function of the relative position between the wind and the blades. In fact, the angle of attack evolves periodically, as the turbine revolves, to the extent that the wind impacts the blade at any inclination.

The pressure and velocity fields were also analyzed on two vertical planes, with normal vector aligned with the axial direction, positioned downstream of the turbine. Namely, the *near* plane was located at 0.75 D far from the turbine axis and the *far* plane at 1.5 D (D denotes the rotor diameter).

Specifically, the wake extension was analyzed, in terms of both fluid deceleration and deflection. The velocity field and the yaw angle computation at each cell showed a highly non-symmetric shape for the wake, characterized by two peaks with different intensity. It would surely be an incomplete explanation to simply relate this non-symmetry to the different relative motions between the blades and the wind at different phases of the revolution (whether the blades move *against* or *in* the wind direction). In fact, this shape was found out to be especially related to the high possibility of fluid stall in low-load operating conditions.

The non-symmetry regards most of the vertical extension of the wake on the analyzed planes, as well as most of the turbine period of revolution. Moreover, it becomes more evident as the wake propagates downstream. All these features are in good agreement with the results of experimental tests.

From the analysis of the drag and lift coefficients referred to each single blade during the transient regime, another relevant aspect about the fluid aerodynamics has been inferred. Indeed, these curves clearly showed two different-frequency fluctuations overlapping. The lower-frequency fluctuation can be directly related to the rotor revolution, i.e. the properties at the blade walls undergo variations whose period equals the time for one full rotation of the machine. The higher-frequency fluctuation in the coefficient curves, instead, was found to be related to the vortex detachment frequency at the blade trailing edge. This was deduced by comparing the velocity and pressure fields at two different times, corresponding to subsequent extremum values of the higher-frequency fluctuation curve. The pressure sudden drop and the velocity vectors distribution at the blade pressure side confirmed this explanation.

In the end, the implemented turbulence model turned out to be very performing for the case under investigation. Therefore, it can be considered suitable for external-aerodynamics cases as well. On the one hand, this conclusion was inferred by observing that the properties smoothly vary throughout the whole domain, and no sudden changes are visible at the in-

terface between the still and the moving subdomains (AMI). On the other hand, the results were compared to a similar simulation on the same case-study that, instead, adopted a standard $k - \omega$ SST model. The validity of DLRM is evident in terms of both accuracy in the description of the flow and ability to capture the flow unsteadiness.

As already discussed, this thesis is an ongoing project. Thus, future work will aim to achieve a deeper knowledge of the fluid behavior, on a longer simulated time, in other to possibly confirm the results highlighted by the analysis of the transient regime. Indeed, a number of rotations for the turbine is required in order to opportunely average the steady-state results in time and make a full comparison with experimental measurements. Moreover, it would be definitively useful to investigate other load-conditions for the turbine operation, to achieve a comprehensive description of the flow behavior. Unfortunately, the high computational cost of these simulations is the largest restriction and the eventual work definitively will result in a long-term project.

Bibliography

[1] N. A. Adams and S. Hickel. *Advances in Turbulence XII*, volume 132. Springer Proceedings in Physics, 2009.

[2] L. Battisti, L. Zanne, S. Dell'Anna, V. Dossena, G. Persico, and B. Paradiso. Aerodynamic measurements on a vertical axis wind turbine in a large scale wind tunnel. *J. Energy Resour. Technol 133(3), 031201*, page 9, Jul 2011.

[3] M.H. Buschmann and M. Gad el Hak. Evidence of nonlogarithmic behavior of turbulent channel and pipe flow. *AIAA Journal*, 47(3), 2009.

[4] H. Chanson. *Applied Hydrodynamics: An Introduction to Ideal and Real Fluid Flows*. CRC Press, Taylor and Francis Group, Leiden, The Netherlands, 2009.

[5] L. Davidson. *Fluid Mechanics, Turbulent Flow and Turbulence Modeling*. Department of Applied Mechanics, Chalmers University of Technology, 2014.

[6] S.L. Dixon and C.A. Hall. *Fluid Mechanics and Thermodynamics of Turbomachinery*. Butterworth-Heinemann, Elsevier, 6th edition, 2010.

[7] V. Dossena, G. Persico, B. Paradiso, L. Battisti, S. Dell'Anna, A. Brighenti, and E. Benini. An experimental study of the aerodynamics and performance of a vertical axis wind turbine in confined and non-confined environment. *Proceedings of ASME Turbo Expo 2015: Turbine Technical Conference and Exposition GT2015*, page 12, June 2015.

[8] G. Falkovich and K.R. Sreenivasan. Lessons from hydrodynamic turbulence. *Physics Today*, 59:4, April 2006.

[9] J. H. Ferziger and M. Perić. *Computational Methods for Fluid Dynamics*. Springer, 3rd edition, 2002.

[10] D. K. Gartling. Multipoint constraint methods for moving body and non-contiguous mesh simulations. *International Journal for Numerical Methods in Fluids*, 47(6-7):471–489, 2005.

[11] GWEC. 2011 global wind report. `http://gwec.net/wp-content/uploads/2012/06/Annual_report_2011_lowres.pdf`.

[12] GWEC. Global wind energy council. http://www.gwec.net.

[13] W. Gyllenram and H. Nilsson. Very large eddy simulations of draft tube flow. *23rd IAHR Symposium, Yokohama, Japan,*, 1(2):1–10, October 2006.

[14] W. Gyllenram and H. Nilsson. Design and validation of a scale-adaptive filtering technique for lrn turbulence modeling of unsteady flow. *J. Fluids Eng*, 130(5):10, April 2008.

[15] M. Hansen. *Aerodynamics of Wind Turbines*. Earthscan, 2nd edition, 2008.

[16] A. Jameson, W. Schmidt, and E. Turkel. Numerical solution of the euler equations by finite volume methods using runge-kutta time stepping schemes. *AIAA Paper*, 1981.

[17] A.N. Kolmogorov. The local structure of turbulence in incompressible viscous fluid for very large reynolds numbers. *USSR Academy of Sciences, translated from Russian into English by V. Levin (1991)*, 30:299–303, 1941.

[18] Z. Lilek, S. Muzaferija, M. Peric, and V. Seidl. An implicit finite volume method using non-matching blocks on structured grid. *Numerical Heat Transfer, Part B: Fundamentals*, 32(4):385–401, 1997.

[19] J.M. McDonough. Introductory lectures on turbulence. Departments of Mechanical Engineering and Mathematics, University of Kentucky.

[20] F.R. Menter. Zonal two equation k-w turbulence models for aerodynamic flows. *AIAA Paper n. 93-2906, 24th Fluid Dynamics Conference*, July 1993.

[21] F.R. Menter. Two-equation eddy-viscosity turbulence models for engineering applications. *AIAA Journal*, 32(8), August 1994.

[22] R.H. Nichols. Turbulence models and their application to complex flows. `http://people.nas.nasa.gov/~pulliam/Turbulence/Turbulence_Guide_v4.01.pdf`.

[23] F. Piscaglia, A. Montorfano, and A. Onorati. A scale adaptive filtering technique for turbulence modeling of unsteady flows in ic engines. *SAE Int. J. Engines*, 2015.

[24] S. B. Pope. *Turbulent Flows*. Cambridge University Press, 2000.

[25] C. L. Rumsey and P. R. Spalart. Turbulence model behavior in low reynolds number regions of aerodynamic flowfields. *38th AIAA Fluid Dynamics Conference and Exhibit*, American Institute of Aeronautics and Astronautics, June 2008.

[26] P. Sagaut. *Large Eddy Simulation for Incompressible Flows*. Springer, 3rd edition, 2006.

[27] D.B. Spalding. A single formula for the law of the wall. *ASME Series E: Journal of Applied Mechanics*, (28):455–458, 1961.

[28] H. Tennekes and J.L. Lumley. *A First Couse in Turbulence*. The MIT Press, 1972.

[29] T. E. Tezduyar. Finite element method for flow problems with movign boundaries and interfaces. *Archives of Computational Methods in Engineering*, 8(2):83–130, 2001.

[30] H. Weller. Controlling the computational modes of the arbitrarily structured c grid. *Mon. Wea. Rev.*, 140:3220–3234, 2012.

[31] D.C. Wilcox. *Turbulence Modeling for CFD*. Griffin Printing, Glendale, CA, 1994.